

HYDROGEN STORAGE IN MAGNESIUM BASED THIN FILMS

A THESIS SUBMITTED TO
THE GRADUATE SCHOOL OF NATURAL AND APPLIED SCIENCES
OF
MIDDLE EAST TECHNICAL UNIVERSITY

BY

HASAN AKYILDIZ

IN PARTIAL FULFILLMENT OF THE REQUIREMENTS
FOR
THE DEGREE OF DOCTOR OF PHILOSOPHY
IN
METALLURGICAL AND MATERIALS ENGINEERING

OCTOBER 2010

Approval of the thesis:

HYDROGEN STORAGE IN MAGNESIUM BASED THIN FILMS

submitted by **HASAN AKYILDIZ** in partial fulfillment of the requirements for the degree of **Doctor of Philosophy in Metallurgical and Materials Engineering, Middle East Technical University** by,

Prof. Dr. Canan Özgen _____
Dean, **Graduate School of Natural and Applied Sciences**

Prof. Dr. Tayfur Öztürk _____
Head of Department, **Metallurgical and Materials Engineering**

Prof. Dr. Tayfur Öztürk _____
Supervisor, **Metallurgical and Materials Engineering Dept., METU**

Prof. Dr. Macit Özenbaş _____
Co-Supervisor, **Metallurgical and Materials Engineering Dept., METU**

Examining Committee Members:

Prof. Dr. Çiğdem Erçelebi _____
Physics Dept., METU

Prof. Dr. Tayfur Öztürk _____
Metallurgical and Materials Engineering Dept., METU

Prof. Dr. Vedat Akdeniz _____
Metallurgical and Materials Engineering Dept., METU

Prof. Dr. Remzi Çetin _____
Metallurgical and Materials Engineering Dept., SU

Assist. Prof. Dr. H. Emrah Ünalan _____
Metallurgical and Materials Engineering Dept., METU

Date : 15-October-2010

I hereby declare that all information in this document has been obtained and presented in accordance with academic rules and ethical conduct. I also declare that, as required by these rules and conduct, I have fully cited and referenced all material and results that are not original to this work.

Name, Last Name : Hasan AKYILDIZ

Signature :

ABSTRACT

HYDROGEN STORAGE IN MAGNESIUM BASED THIN FILMS

Akyıldız, Hasan

Ph.D., Department of Metallurgical and Materials Engineering

Supervisor : Prof. Dr. Tayfur Öztürk

Co-Supervisor: Prof. Dr. Macit Özenbaş

October 2010, 146 pages

A study was carried out for the production of Mg-based thin films which can absorb and desorb hydrogen near ambient conditions, with fast kinetics. For this purpose, two deposition units were constructed; one high vacuum (HV) and the other ultra high vacuum (UHV) deposition system. The HV system was based on a pyrex bell jar and had two independent evaporation sources. The unit was used to deposit films of Mg, Mg capped with Pd and Au-Pd as well as Mg-Cu both in co-deposited and multilayered form within a thickness range of 0.4 to 1.5 μm . The films were crystalline with columnar grains having some degree of preferred orientation. In terms of hydrogen storage properties, Mg/Pd system yielded the most favorable results. These films could desorb hydrogen at temperatures not greater than 473 K. The study on crystalline thin films has further shown that there is a narrow temperature window for useful hydrogenation of thin films, the upper limit of which is determined by the intermetallic formation. The UHV deposition system had four independent evaporation sources and incorporated substrate cooling by circulating cooled nitrogen gas through the substrate holder. Thin films of Mg-Cu were

produced in this unit via co-evaporation technique to provide concentrations of 5, 10 and 15 at. % Cu. The films were 250-300 nm thick, capped with a thin layer of Pd, *i.e.* 5-25 nm. The deposition was yielded nanocrystalline or amorphous Mg-Cu thin films depending on the substrate temperature. At 298 K, the films were crystalline, the structure being refined with the increase in Cu content. At 223 K, the films were amorphous, except for Mg:Cu=95:5. The hydrogen sorption of the films was followed by resistance measurements, with the samples heated isochronally, initially under hydrogen and then under vacuum. The resistance data have shown that hydrogen sorption behaviour of thin films was improved by size refinement, and further by amorphization. Among the films deposited, amorphous Mg:Cu=85:15 alloy could absorb hydrogen at room temperature and could desorb it at 223 K (50 °C), with fast kinetics.

Keywords: Hydrogen Storage; Thermal Vapor Deposition; Thin Film; Co-deposition; Resistance; Crystalline; Nano-size; Mg/Pd; Mg-Cu/Pd

ÖZ

MAGNEZYUM ESASLI İNCE FİMLERDE HİDROJEN DEPOLAMA

Akyıldız, Hasan

Doktora, Metalurji ve Malzeme Mühendisliği Bölümü

Tez Yöneticisi: Prof. Dr. Tayfur Öztürk

Ortak Tez Yöneticisi: Prof. Dr. Macit Özenbaş

Ekim 2010, 146 sayfa

Çalışma, düşük sıcaklık ve basınç aralıklarında, hızlı şekilde hidrojen depolama için uygun, Mg-esaslı ince film malzemelerin geliştirilmesini hedef almıştır. Bu amaca uygun olarak iki çöktürme birimi imal edilmiştir. Bunlar yüksek vakum ve çok yüksek vakum çöktürme birimleridir. Yüksek vakum birimi cam fanus esaslı olmakla birlikte iki çöktürme kaynağına sahiptir. Bu sistemde 0.4- 1.5 μm kalınlık aralığında saf Mg, yüzeyi Pd ve Au-Pd ile kaplanmış Mg, Cu ile eş-zamanlı çöktürülmüş ve tabakalandırılmış Mg filmler üretilmiştir. Çöktürülen filmlerin hepsi kristalin yapıda, kolonsal tanelerden oluşmaktadır ve film büyümeye sırasında belirli tercihli yönlenme göstermektedir. Hidrojen depolama özellikleri açısından, Mg/Pd sistemi en faydalı sonuçları vermiştir. Bu filmler 473 K'de depoladıkları hidrojeni geri verebilmektedir. Kristalin yapıdaki filmler üzerine yapılan çalışma, ayrıca filmlerin hidrürlenmesi için belirli dar bir sıcaklık aralığının varlığını da ortaya koymustur. Bu sıcaklık aralığı film içinde intermetalik fazların oluşumuna izin vermeyecek üst sıcaklık ile sınırlıdır. Çok yüksek vakum ünitesi dört ayrı çöktürme kaynağı içermektedir. Birim, soğutulmuş azot gazı çevrimi ile altlık soğutma

imkanına sahiptir. Bu sistemde eş zamanlı çöktürme yöntemi ile atomik olarak % 5, 10 ve 15 Cu içeren Mg-Cu ince filmleri üretilmiştir. Film kalınlıkları 250-300 nm arasındadır. Üretilen tüm filmler 5-25 nm kalınlığında Pd tabakası ile kaplanmıştır. Çöktürülen filmler altlık sıcaklığına bağlı olarak nanokristalin ya da amorf yapıda oluşmaktadır. Bahsi geçen tüm kompozisyonlar 298 K altlık sıcaklığında kristalin yapıda çökmekte ve kompozisyonda artan Cu miktarı ile film tane yapısında incelme meydana gelmektedir. 223 K de ise Mg:Cu=95:5 dışındaki kompozisyonlar amorf yapıda oluşmaktadır. Filmlerin hidrojen depolama davranışları rezistans ölçme yöntemi ile takip edilmiştir. Filmler eşsureli olarak önce sabit hidrojen basıncı altında ısıtılmış, daha sonra ısıtma işlemi vakum altında devam ettirilmiştir. Çalışma filmlerde tane yapısında incelmeye bağlı olarak hidrojen depolama özelliklerinin iyileştiğini göstermektedir. Bu iyileşme amorflaşma ile birlikte daha da artmaktadır. Üretilen filmlerden, Mg:Cu=85:15 alaşımı hidrojeni oda sıcaklığında depolamakta ve 223 K (50 °C)'de hızlı bir şekilde geri bırakmaktadır.

Anahtar Sözcükler: Hidrojen Depolama; Isıl Buhar Çöktürme; İnce Film; Eş-zamanlı Çöktürme, Kristalin, Nano-boyut, Mg/Pd, Mg-Cu/Pd

To Bekir and Hasan

ACKNOWLEDGEMENTS

I wish to express my deepest gratitude to my supervisor Prof. Dr. Tayfur Öztürk and co-supervisor Prof. Dr. Macit Özenbaş for their firm guidance, suggestions, prompt feedbacks, patience, advise, critisizm, encouragements, and close collaboration throughout the research.

I would also thank; Prof. Dr. Vedat Akdeniz, Prof Dr. Kadri Aydinol, and Prof. Dr. Şakir Bor, for their precious helps, advice, valuable support and encouragement during the development of the study.

I am indepted to my colleagues and friends; Assoc. Prof. Dr. Mehmet Şimşir, Assist. Prof. Dr. Ziya Esen, Dr. Tarık Aydoğmuş, Assist. Prof. Dr. M. Serdar Karakaş, Dr. Arda Çetin, Tufan Güngören, Fatih G. Şen, Nevzat Akgün, Assist. Prof. Dr. Y. Eren Kalay, Dr. Murat Güvendiren, Dr. Kaan Pehlivanoğlu, Şahin Coşkun, Irmak Sargin, Serdar Tan, Dr. Elif Tarhan B., Rabia Ölmez, Mustafa Yılmaz, Alper Kınacı, Dr. Öncü Akyıldız, Çağla Özgit, Onur R. Bingöl, Özlem A. Yıldırım, Mehmet Yıldırım, Evren Tan, Gülhan Çakmak and Savaş Özün for their help and patience. Additional thanks go to Dr. Seymen Aygün, Assoc. Prof. Dr. Jon-Paul Maria, Burcu Meriç, Ege Hürgel, Dr. Metin Balıkçıoğlu and Sinem Aladağ for their support and encouragement.

Special thanks to my family for their supports. Finally, thanks to all the technical and administrative staff of the Metallurgical and Materials Engineering Department, especially to Cemal Yanardağ, Ebru Özdemir Arslan, Gülden Şimşek, İsa Hasar, Atalay Özdemir and Cengiz Tan for their suggestions, help and comments during this study.

This thesis study has been financially supported by DPT-ÖYP research fund and by TÜBİTAK (Project 104M206).

TABLE OF CONTENTS

ABSTRACT	iv
ÖZ	vi
ACKNOWLEDGEMENTS	ix
TABLE OF CONTENTS.....	x
CHAPTERS	
1. HYDROGEN STORAGE-OVERVIEW	1
1.1 INTRODUCTION	1
2. LITERATURE REVIEW	5
2.1 INTRODUCTION	5
2.2 MECHANICAL ALLOYING	7
2.3 THIN FILMS AND NANO-SIZED MATERIALS.....	9
2.4 Mg-BASED THIN FILMS	10
2.5 HYDROGEN IN AMORPHOUS STRUCTURES	16
2.6 CAPACITY MEASUREMENTS	19
3. THIN FILM CONDENSATION PHENOMENA	21
3.1 INTRODUCTION	21
3.2 CONDENSATION	21
3.3 NUCLEATION AND GROWTH.....	23
3.3.1 Island Growth Mode, Three-Dimensional	26
3.3.2 Layer-by-Layer Growth Mode, Two-Dimensional.....	26
3.3.3 Mixed Growth Mode, 2D to 3D Transition	27
3.4 GROWTH MODES OF Mg THIN FILMS	27
3.5 STRUCTURE-ZONE MODELS.....	29
3.6 AMORPHOUS ALLOYS.....	34
3.6.1 Kinetic Criteria for Amorphous Phase Formation	35
3.6.2 Structural Criteria for Amorphous Phase Formation	38
3.7 AMORPHOUS THIN FILMS	40
4. HYDROGEN STORAGE IN Mg-BASED CRYSTALLINE THIN FILMS ...	48

4.1 INTRODUCTION	48
4.2 MATERIALS AND METHOD	49
4.2.1 High Vacuum Deposition System.....	49
4.2.1.1 Substrate Holder.....	51
4.2.1.2 Power Sources.....	52
4.2.2 Deposition Conditions.....	52
4.2.3 Hydrogen Storage	52
4.3 RESULTS AND DISCUSSION	53
4.4 CONCLUSIONS.....	66
5. HYDROGEN STORAGE IN Mg-BASED	
AMORPHOUS/NANOCRYSTALLINE THIN FILMS	68
5.1 INTRODUCTION	68
5.2 MATERIALS AND METHOD	70
5.2.1 Ultra High Vacuum Deposition System.....	70
5.2.1.1 Bell Jar	71
5.2.1.2 Vacuum Pumps	71
5.2.2 Substrate Cooling System and Operation	76
5.2.3 Ultra High Vacuum Levels	78
5.2.4 Quartz Crystal Thickness Monitor	80
5.2.5 Thin Film Production	82
5.2.5.1 Deposition Conditions.....	82
5.2.6 Hydrogenation and Characterization of Thin Films.....	83
5.2.6.1 Resistance Measurement Set-up	85
5.2.6.2 Hydrogen Loading and Dehydrogenation.....	86
5.2.6.3 XRD	87
5.3 RESULTS AND DISCUSSION	89
5.3.1 Structural and Morphological Characterization	89
5.4 CONCLUSIONS.....	115
6. MAXIMIZING HYDROGEN STORAGE CAPACITY OF Mg-BASED THIN	
FILMS	117
7. CONCLUSIONS.....	130
REFERENCES.....	132

CURRICULUM VITAE	145
------------------------	-----

CHAPTER 1

HYDROGEN STORAGE-OVERVIEW

1.1 INTRODUCTION

Replacing of the current fossil fuel based technology with the sustainable energy sources is an important consideration. Apprehensions about the energy security and monopolar distribution of the available fuels accelerated the research on the field. Environmental problems related to pollution are also alerting due to fossil fuel emissions. Among the alternatives, utilization of wind, solar or geothermal energy and distribution of the stored energy as in the form of hydrogen network is a widely envisioned approach. For this purpose, hydrogen has to be produced economically, and, more importantly, it is necessary to find an effective way for its storage. However, for practical applications, there is not yet an ideal solution exists for effective storage of hydrogen. Whatever that method, the material should reversibly store a significant amount of hydrogen under moderate pressure and temperature conditions.

Efforts to find a proper material for storage lead the research mainly in five different categories. These are namely, pressurized tank, liquefaction, physisorption in porous materials, complex hydrides and metal hydrides including the intermetallic compounds. Pressurized tank is the conventional technique. With the advance of technology today it is possible to manufacture storage tanks in a composite structure which can withstand a pressure up to 700 bar. However, the energy densities are still too low. The high cost of the tank and safety considerations remains to be solved, (Zhou 2005).

Liquefaction process requires relatively large amount of energy and insulation. This increases the cost, (Züttel 2004). Physisorption is based on the interaction of hydrogen molecules with the adsorbent surface. Carbon nanotubes in this field attracted much attention. Physisorption, in fact, has many advantages such as low cost, simple material design and low operating pressures. However, the amount of stored hydrogen is quite low, (Sakintuna *et al.* 2007). Complex hydrides include Group I and II salts of $[AlH_4]^-$, $[NH_2]^-$ and $[BH_4]^-$. These are alanates, amides and borohydrides. They received considerable attention in the last decade in the field of hydrogen storage. They have a very high hydrogen storage capacity e.g. 16.78 wt. % for $Al(BH_4)_3$, but in general, they have significant drawbacks. The problem with the alanates is the insufficient reversible capacity. And amides and borohydrides suffer from slow kinetics and undesirable by-products, such as ammonia and diborane, (Orimo *et al.* 2007). Finally, the complex hydride approach is still immature and needs further investigation.

Metal hydrides including elemental hydrides, alloys and intermetallics constitute an important group of storage. In the early 70s, discovery of $LaNi_5$ and $FeTi$ attracted much attention. A significant progress has been made on these and similar intermetallics over the last four decades in terms of reaction temperature and pressure, but their low storage capacity, below 2 wt. % makes them undesirable. On the other hand, light elements, which are located in the first two rows of the periodic table; have high storage capacity and have low weight. Elements cover Li, Be, B, C, N, O, Na, Mg, Al, Si and P. Among these, only Li, Na, C, Mg and Al have stable hydrides at room temperature and gravimetric density of above 7 wt. %. The equilibrium pressures for Li and Na are well below 1 bar at RT, and AlH_3 requires very high pressures for reversibility. Thus, Mg remains the only candidate for reversible hydrogen storage, (Aguey-Zinsou and Ares-Fernandez, 2010).

Currently target set in various programs, for hydrogen storage aim at capacities of 6 wt. % (gravimetric) and 0.045 kg/L (volumetric), (DOE). The program also aims to find a material which can operate within temperatures of -30 to 120 °C and pressures of 3 to 10 bar.

Mg has high gravimetric and volumetric storage capacities, which are 7.65 wt. % and 1.4 kg/L, respectively, (Selvam *et al.* 1986). It is relatively low-cost and light-weight metal found on a large scale in the earth's crust. As seen, it satisfies most of the requirements set for hydrogen storage. However, kinetics of hydrogen sorption is sluggish and very high temperatures are necessary for desorption of the hydrogen, i.e. 300-350 °C. For a stable hydride such as MgH₂ the heat necessary for desorption of hydrogen at 1 bar is 25 % of the heating content of the hydrogen. This makes the use of Mg uneconomical.

The high thermodynamic stability of MgH₂ results in a relatively high desorption enthalpy of approximately 75 kJ/mol-H₂ under standard conditions, which corresponds to an equilibrium temperature of roughly 288 °C (practically 300 °C) for H₂ desorption under 1 bar hydrogen atmosphere, (Grochala and Edwards, 2005). For a material which to desorp hydrogen below 80-85 °C at 1 bar pressure, the dehydrogenation enthalpy should be around $\Delta H_f = 47 \text{ kJ/mol H}_2$.

Sluggish kinetics is the second limitation for Mg-H system. The reason for such reaction kinetics is not clear yet, but it is attributed to a number of reasons; oxide layer around the particles, poor dissociation rate of hydrogen on magnesium surfaces and the slow diffusion of hydrogen both in Mg and MgH₂, (Augey-Zinsou and Ares-Fernandez, 2010).

Efforts spanning over four decades have focused on alloying of Mg with other elements to find a proper composition which will reduce the bond strength between Mg-H. Alloying approach has accepted in time as a rule of thumb rule for production and this made use of alloying with elements such as, Ni, Cu, Fe, Co, (Sandrock and Thomas 2001, Milanese *et al.* 2008).

Most of the study employed mechanical alloying as a processing method to obtain refined and/or alloyed Mg, (Güvendiren *et al.* 2004). Additives such as Ni, (Gutfleisch *et al.* 2003), Ce, Ti, Nb, (Ivanov *et al.* 1987), LaNi₅ and FeTi, (Gross *et al.* 1998), Fe, Co and Cr, (Liang *et al.* 1999) and various metal oxides (Oelerich *et*

al. 2001) have been added for the purpose of destabilization. However, additives just enhanced the kinetics. Improved kinetics was attributed to a number of reason; the formation of fresh, oxide free surfaces and grain boundaries, and defects introduced to the structure during milling under protective atmospheres. Due to additives, the milling process efficiency was increased and finer structures were obtained.

Thin film hydrides are an emerging field of research. Thin film method is a very versatile method, which provides an easy control of chemical make-up, structure, and geometric design of the material. It is expected to yield fast reaction rates because of large surface to volume ratio.

The current study, therefore, aims to produce thin films of Mg-based materials which can absorb and desorb hydrogen at ambient temperatures and pressures, with fast kinetics. For this purpose, Mg and Mg-based thin films were produced via physical vapour deposition (PVD) method. Films were deposited in both crystalline and amorphous states.

This thesis comprises seven chapters. A literature review of Mg-based hydrides is presented in Chapter 2. Chapter 3 focuses on the fundamentals of thin film production with an emphasis on crystallization and amorphization. Experimental set-up with glass bell-jar for the production of crystalline thin films is given in Chapter 4. Similarly, the set-up with stainless steel bell-jar for the production of refined and amorphized thin films is given in Chapter 5. These two chapters present all experimental results, a broad discussion on the production of these films and their hydrogen sorption behaviour. Chapter 6 focuses on maximizing the storage capacity of Mg-based thin films and examines the question by including the literature data. Finally, the conclusions derived from the current study are given in Chapter 7.

CHAPTER 2

LITERATURE REVIEW

2.1 INTRODUCTION

MgH_2 as an energy carrier has the highest energy density, 9 MJ/kg Mg, of all reversible hydrides applicable for hydrogen storage. It combines high capacity, low-cost and abundance. However, the large enthalpy value of the hydride phase makes hydrogen desorption impossible at low temperatures. Further, there is a large amount of heat released during absorption and absorbed during desorption. Thus, a heat management problem arises for practical storage designs.

The strategy for the production of materials with reduced stability follows two possibilities, based on alloying approach. The first one is to produce ternary hydrides of Mg at the expense of capacity. The second one is the preparation of a suitable composition of $\text{Mg}-X$ where X is the alloying element which provides only MgH_2 formation during hydrogenation, with free precipitation of the alloying element X . For the second possibility the formation of intermetallic phase/phases of the constituent elements, during sorption reactions, because of applied temperature may affect the properties inversely if the yielded intermetallic does not react with hydrogen and returns to elemental form when desorbed.

The statement is also valid for the case where the element X was used to obtain extended solid solution of $\text{Mg}-X$. In such cases solid solution, when exposed to elevated temperatures, may become unstable and element X may precipitate in

energetically favourable regions or it may form intermetallics with Mg, with the result that the original composition was altered, (Liang 2004).

The second problem with Mg is the sluggish reaction kinetics of the reaction with hydrogen. Several hours are required for full ab/desorption of hydrogen for bulk magnesium. This is basically due to slow dissociation rate of hydrogen molecule on Mg surfaces, and the high tendency of Mg to oxidation. Size refinement and proper additive incorporation are the only means to overcome these limitations.

According to Christmann 1988, hydrogen reacts with solid surfaces by either physisorption or chemisorption. In physisorption weak Van der Waals bonds are formed. Dissociation of hydrogen molecule to hydrogen atoms and then chemical bonding of hydrogen with surface atoms occurs during chemisorption. After chemisorption, host solid dissolves small amount of hydrogen to form a solid solution which is generally called α -phase. With the increase of hydrogen concentration in the host, hydrogenation continues with nucleation and growth of the hydride phase. This phase is referred to β -phase and it is reflected to the plateau region in pressure-composition-isotherms (PCI), (Züttel 2005). Reaction of hydrogen with the solid as explained above were affected by a number of features; crystal structure of the host metal, diffusion coefficient of hydrogen in the host, dislocation density, type and size of the interstitials and etc. The heat supplied to the material during processing is used for dissociation of hydrogen. But for hydrogenation to take place, diffusion into the lattice is required. Further, there will be no nucleation and growth, for the hydride phase formation, unless there is hydrogen diffusion in the host. Due to those relationships, thermodynamic and kinetic problems have to be considered together.

Alloying for destabilization and size refinement to fasten reaction rates can be accomplished by a variety of methods. The following sections will first discuss mechanical alloying for this purpose. Method uses the impact and grinding actions to create fresh surfaces and refined structures during milling. It can provide chemical modification to a certain extent when different elements are milled.

2.2 MECHANICAL ALLOYING

This process provides the opportunity for the synthesis of metal hydrides and size refinement at the same time. Atmosphere controlled and/or cryogenic milling is also possible. These opportunities make the method desirable for the preparation of hydrogen storage materials. The following sections review some of the studies which utilized ball-milling as the production method to achieve less stable Mg-based hydrides.

Efforts to produce metal hydrides with reduced stability yielded ternary hydrides such as Mg_2NiH_4 . This material has a lower enthalpy of dehydrogenation than that of MgH_2 , which is around; $\Delta H_f = -62$ kJ/mol H_2 . However, the storage capacity of this alloy was substantially reduced (3.8 wt. %) and temperature for desorption was still too high *i.e.* 573 K (Reilly and Wiswall 1968). The formation of ternary intermetallic phase by the addition of V, Cr, Fe, Co and Zn to Mg_2Ni to obtain a further reduction in stability suffered from the tendency of the alloy to decompose into more stable binary intermetallics upon cycling, (Darnaudery *et al.* 1983). Milling of MgH_2 -Ni with elemental powders like Cu, Si, Al, Ca and Co, yielded ternary intermetallics of Mg - Ni - Si and Mg - Ni - Cu only, (Klassen 2006). Ternary phase with Cu showed higher plateau pressure than pure Mg_2NiH_4 , but the capacity was further reduced *i.e.* 3.05 wt. %. The Mg - Ni - Si intermetallic did not react with hydrogen and decomposed into two intermetallics, only Mg_2Ni reacted with hydrogen to form Mg_2NiH_4 , and Mg_2Si phase did not react when exposed to hydrogen. Mg_2Ca with a dehydrogenation enthalpy of 42 kJ/mol H_2 found to be quite promising, but CaH_2 formation during hydrogenation lead to phase decomposition. This hydride, CaH_2 formed as a result was more stable than MgH_2 . (Mintz *et al.* 1980). Modification of Mg with other transition metals, such as Fe led to ternary hydride *i.e.* Mg_2FeH_6 , which has the same stability of pure MgH_2 , (Selvam *et al.* 1986).

To improve the capacity and to reduce of hydrogenation enthalpy, addition of light elements or complex hydrides to Mg, such as Si and $LiBH_4$ has recently been

proposed, (Vajo *et al.* 2004 and 2005). The approach really produced destabilized alloys with high capacity, but due to slow ionic mobility they suffer from poor kinetics, (Kelly *et al.* 2009).

Nanocrystallization by itself has been considered a way to reduce the stability of metal hydrides. It was predicted that, sufficient size refinement, below 5 nm first lowers the enthalpy by 30 %, (Berube *et al.* 2007). However, a reduction in enthalpy has not been observed due to the rapid recrystallization of nanocrystals at moderate temperatures, (Aguey-Zinsou *et al.* 2007).

On the other hand, nanocrystalline magnesium has been reported to absorb hydrogen without any need for activation, (Zaluski *et al.* 1999). Klassen *et al.* 2001 showed that nanocrystalline Mg can fully store hydrogen in minutes at 573 K and desorbs it in 1 h at the same temperature. During milling, the particle size decreases substantially, and new oxide free surfaces are created. In addition to these, surface defects are introduced. All promote hydrogen molecule dissociation. Reduced size decreases the need for long range diffusion, thus enhances the kinetics. All additives discussed above, especially the transition metal oxides, in fact, facilitate particle size reduction during the milling process, and allow fast reaction rates, (Oelerich *et al.* 2001, Güvendiren *et al.* 2004). The milling also helps to distribute and form decorated/doped particulate structure by catalyst elements such as Pd, Ni, Ti and etc, (Xu and Song 2006).

Among for all the systems examined up to now, no Mg-based alloy was found, which can satisfy targets set for practical applications, (Auges-Zinsou and Ares-Fernandez 2010). All these studies on mechanical alloying and catalyst incorporation, indicate clearly that size reduction associated with increase in surface area and catalytic effect of additives just enhances the kinetics of desorption but not the stability of the MgH₂, (Bouaricha *et al.* 2000).

2.3 THIN FILMS AND NANO-SIZED MATERIALS

As reviewed above, by milling improved reaction rates may be possible, but no significant improvement observed in thermodynamics. Thin film processing is an alternative method which has the same capabilities as mechanical milling.

Thin films have many advantages over bulk materials. In the case of thin films, a thin catalyst layer deposited generally on top, easily dissociates hydrogen molecule to atomic form or vice versa during desorption. This eliminates the requirement of high temperature activation of Mg surface, (Olsson 2004, Roger *et al.* 2007). In addition, this layer protects highly reactive Mg-surfaces against oxidation or poisoning, (Wenzel *et al.* 1983). On the other hand contamination of the unprotected particle surfaces by the impurity gases was reported to be the one of the most important disadvantage of mechanical alloying, (Suryanarayana 2001).

Further, deposition techniques are highly flexible for the formation of alloys. With the utilization of co-deposition or pre-alloyed targets, one can obtain thin film materials in all fractions of X in Mg- X .

Thin films provide a higher surface to volume ratio when compared to the powder or bulk counterparts, (Jain *et al.* 1988). Further, they all have a simple geometry. Thus, it is reasonable to examine the hydrogen sorption mechanism in such surfaces and interfaces, (Leon *et al.* 2002). In addition, extended solid solubilities or non-equilibrium phases can be obtained by deposition of multicomponent films, which could be difficult to produce through mechanical alloying, (Liang *et al.* 1999 and Berlouis 2003).

Thin film production is also a suitable method for an effective and controlled size reduction. Berube *et al.* 2007 have summarized the benefits and detriments of nano-engineering on the properties of metal hydrides, as shown in Table 1.1. Synthesizing nano-sized materials generally provides improvement on the

thermodynamic and kinetic properties of the materials in terms of formation enthalpy and thus decrease release temperature or fasten kinetics.

On the other hand, nature of nanostructures such as having higher ratio of grain boundaries, surfaces and defects may lead to reduced cyclic stability and temperature based degradations.

Nano-structuring by thin film method and precise geometric design of the deposited layers provide control on the net diffusion direction of hydrogen during sorption and eliminates the need for long-range transport. Thus, in a thin film sample within the limits of nano-sizes, hydrogen has to diffuse a shorter distance through the lattice for the formation of the hydride phase, (Fujii and Orimo 2003, Oujang *et al.* 2005).

2.4 Mg-BASED THIN FILMS

Mg-based thin films can be produced via condensation method in a variety of deposition systems. Thermal or electron beam evaporation and different versions of sputtering are the most common methods used for the production of thin film hydrogen storage materials. In recent years, pulsed laser deposition was also employed successfully for the same purpose. In thin film hydrogen storage studies, generally, Mg is the main constituent element in the film, but in some cases the intermetallic phases of Mg are produced aiming for the stoichiometric compositions. Thin films of Mg are generally produced in pure, multilayered, and alloyed forms in the presence of second or third elements/compounds. For alloying, co-deposition method is generally employed. An alternative method is to deposit Mg and other elements sequentially followed by a proper heat treatment to obtain the final stoichiometry. In most cases, a thin catalyst layer is applied on top or bottom or both sides of the film. This aims to prevent oxidation of the films and for easy dissociation of hydrogen molecule to its atomic form.

Table 1.1 Some benefits and detriments of nano-size production on hydrogen storage properties of metal hydrides.

(Table adapted from Berube et al., 2007)

		Storage Capacity	Kinetics	ΔH_f	Heat		
					Transfer	Cyclability	$T_{dec.}$
III	Increased Surface Area	Increased physisorption	Increased surface dissociation	Decreased (nano-grained materials)	Decreased	Potentially decreased	Potentially decreased
	Increased Grain Boundaries	Decreased	Increased Diffusion (α)	Potentially Decreased	Decreased	Potentially decreased	Potentially decreased
	Doping with Catalysts	Decreased for excessive doping	Increased	No observed effect	Decreased	May help reversibility	Decreased
	Increased Porosity	Potentially increased physisorption	Faster gas diffusion	No observed effect	Decreased	No observed effect	No observed effect
	Formation of Nano-composites	Mean of components	Increased	Potentially Decreased	Decreased	Potentially increased or decreased	Decreased
	Doping/Alloying	Potentially increased or decreased	Potentially increased	Decreased	Potentially increased or decreased	Potentially increased or decreased	Decreased

The following sections give a review of Mg-based thin films for hydrogen storage. These films were all produced either by sputtering or thermal/e-beam evaporation methods. Review covers different aspects of hydrogen storage in Mg-based thin films, such as effect of doping and alloying, kinetics and thermodynamics of hydrogenation.

Morris *et al.* 1999 have compared the same Mg compositions produced by deposition and mechanical alloying in terms of kinetics, storage capacity and degradation. Study showed that, thin film samples absorbed hydrogen faster than the powder samples. The capacity in thin films at 673 K was also higher. On the other hand, thin films were subject to early degradation by sorption cycles. There were no differences observed in terms of stability, between the powder and thin films and accordingly the dehydrogenation temperature of the films were reported as 723 K.

Leon *et al.* 2002 investigated the hydrogenation behaviour of Mg thin films exposed to air. 30 μ m thick films were deposited via thermal evaporation at 3×10^{-6} torr. In this work, hydrogenation was carried out at 623 K under 10 bar H₂ atmosphere. Hydrogen content in the films was 7.5 wt. %. Degradation of the film observed with repeated cycles. Dehydrogenation was performed under 0.21 bar residual H₂ pressure. The hydrogen release temperature of films were quite high, *i.e.* 623 K. Following a similar idea, Hjort *et al.* 1996 have investigated the effect of oxygen in Mg/MgO_x interfaces in a multilayer. The study revealed that it has a significant effect on the hydrogenation kinetics of the film. When oxygen in MgO_x is less than 160 ng/cm, hydrogen absorption occurs more rapidly. It was also stated that, using such a layered structure in the presence of MgO_x, lead to a decrease in the total capacity. In case of higher oxygen content, a reduction was observed both for the total capacity and hydrogenation kinetics. No data was provided for the temperature of hydrogen release.

Pd, V, Ti, Ni, Nb, Al₂O₃ and Nb₂O₅ are commonly used additives for Mg-based thin films as in the case of mechanical alloying. They can be applied either in the form of doping or top layer coating. Leon *et al.* 2003 studied the catalytic effect of Pd and V

doping to pure Mg thin films. The study showed that the films with lower V concentration absorb hydrogen more rapidly than pure or Pd doped Mg thin films. The films could absorb 6 wt. % hydrogen within 240 min. at 623 K under 10 bar hydrogen atmosphere in the first cycle. Enhanced rates were observed for both absorption and desorption for the second cycle. Dehydrogenation was performed at 623 K. Mosaner *et al.* 2004 reported a similar enhancement in kinetics with Nb doping, without mentioning any conditions for desorption.

Most studies about alloying of Mg, comprises deposition of non-stoichiometric alloys. For example, Kalisvaart *et al.* 2006 prepared Mg_xSc_{1-x} alloys by means of e-beam deposition and electrochemically characterized the sorption properties. Electrochemical storage was conducted at room temperature and it was found that thin film samples could absorb 6.5 wt. % hydrogen. The enthalpy of formation calculated from the mid-plateau pressure was about -78 kJ/mol H₂, a value quite close to that normally reported for MgH₂. In a similar study, Vermeulen *et al.* 2006 reported that Mg_xTi_{1-x} thin films deposited via e-beam deposition showed an excellent rate with a very high storage capacity at room temperature measured electrochemically. They concluded that 20 at. % Ti content is the lowest limit for the enhanced rate-capability. Further, higher Ti contents were reported to reduce the absorption capacity since Mg was the absorbing phase. Borsa *et al.* 2006 deposited similar films by co-sputtering and hydrogenated under 1 bar H₂ at room temperature. Mg-(20-30) at. % Ti were tested for sorption cycles and found to be stable up to 15 cycles under their experimental conditions. In a later study, they reported room temperature desorption for 50 nm thick Mg-30 at. %Ti film (Borsa *et al.* 2007)

Farangis *et al.* 2003, studied Mg/Ni, Fe, Co, Mn, Ti thin films. Richardson *et al.* 2003 were also examined similar systems; Mg-Ti, Mg-Ni, Mg-Co. The films were rather thin, < 100 nm. Farangis *et al.* found that absorption took place at room temperature and MgH₂ formed reversibly in all systems, but there were also the formation of ternary hydride in the case of Mg-Ni thin films. Authors did not provide any data with respect to desorption temperature. Pranevicius *et al.* 2004 used Al as an additive to Mg. After deposition, Mg₁₇Al₁₂ intermetallic formation was

observed. Ternary hydride, $Mg(AlH_4)_2$ was formed at 303 K in 30 min. Dehydrogenation was found to proceed in two steps. They reported that $Mg(AlH_4)_2$ was dissociated into two hydride phases; MgH_2 and AlH_3 . AlH_3 released hydrogen at 373-403 K. The second step comprised dehydrogenation of MgH_2 and formation of Mg_2Al_3 intermetallic phase at 503-523 K.

Stoltz and Popovic 2007 deposited ultra thin Mg-Ni films. They examined the desorption behaviour of the films under photoelectron spectroscopy and observed that hydrogen desorption starts at 400 K. Hydrogenation of vapor synthesized Mg_2Ni phase was studied by Guthrie and Thomas 1998, and the reaction enthalpy was found to be $\Delta H_f = - 64.4$ kJ/mol H_2 . Closer enthalpy values ($\Delta H_f = - 67$ kJ/mol H_2) were reported by Liang *et al.* 1999, with the synthesis of nanocrystalline Mg_2Ni . However, the absorption temperature was 573 K. In a recent study, Shao *et al.* 2009 showed that mechanically alloyed $Mg_{50}Ni_{50}$ with a “grain size” of 1-3 nm could only absorb 1.85 wt. % hydrogen at 373 K under 70 bar.

Palladium-covered Mg thin films was first reported by Krozer and Kasemo 1987, in which hydrogen sorption properties were investigated via quartz-crystal microbalance (QCM) method. The study revealed unusual kinetics where the hydrogen uptake was saturated far from stoichiometric MgH_2 at room temperature. The saturation uptake decreased with increasing hydrogen pressure. They explained their results in terms of hydride formation at the Pd/Mg interface, which is claimed to block further hydrogen uptake, resulting in partial hydrogenation.

Similar studies were also conducted by Krozer and Kasemo 1989, 1990 and Rydén *et al.* 1989. Focus of these studies was basicly the examination of the equilibrium pressure. Krozer and Kasemo 1990 defined two temperature limits; one is the lower temperature at which MgH_2 starts to form, the other is the temperature at which Mg-Pd intermetallics starts to form. The former temperature is pressure dependent. They concluded that the pressures exposed on the sample must be moderate since at too low pressures the uptake rate becomes so small, resulting in impractically long equilibration times and at too high pressures the uptake becomes so rapid that the

dissipated chemical energy of the exothermic hydrogenation reaction raises the temperature of the sample and thus preventing measurements under isothermal conditions. By studying thermodynamics of hydrogen uptake within the specified limits, Krozer and Kasemo (1989, 1990) also determined the enthalpies of hydriding and dehydriding as $\Delta H_f = -60.7 \pm 6.3$ kJ/mol H₂ and $\Delta H_d = 71.2 \pm 4.2$ kJ mol⁻¹ H₂, respectively.

A promising study, in terms of desorption temperature was performed by Higuchi *et al.* 2002. They investigated the effect of Pd layers on the dehydrogenation behaviour of Mg thin films. In this study, Mg film was sandwiched in between 50 nm thick Pd layers. Hydrogenation was applied under 1 bar H₂ pressure at 373 K for a dwell time of 24 h. They reported that Pd layers stored 0.15-0.3 wt. % hydrogen and Mg absorbed 5 wt. % hydrogen, independent of its thickness. More importantly, Higuchi *et al.* stated that all hydrogen in the film can be released at temperatures not more than 373 K. Fujii and Orimo 2003 also verified these results. They also claimed that the capacity and the reaction temperatures were not changed even after 10 sorption cycles.

Pd capped Mg based thin films were also studied by Yoshimura *et al.* 2004, Pasturel *et al.* 2006, and Slack *et al.* 2006. Higuchi *et al.* 1999 claimed that desorption temperature was inversely proportional to the crystallinity of Mg/Pd films. Yamamoto *et al.* 2002 found dehydriding temperature of 453 K by observing the formation of Mg precipitates on a macroscopic scale at the film. Mg/Pd thin films were crystalline in this study with 200 nm and 50 nm thick Mg and Pd layers, respectively. Pasturel *et al.* 2006 claimed that complete desorption of hydrogen is difficult at room temperature from X-ray amorphous Pd doped Mg thin films. On the other hand, Westerwaal *et al.* 2006 observed that in-situ grown amorphous like 200 nm thick Mg₂NiH₄ films can desorb hydrogen very quickly under high vacuum conditions as well as in air, provided that there is a Pd layer on the surface. In the absence of Pd, even under high vacuum conditions, dehydrogenation was limited by the kinetic reasons and occurred in negligible amounts. X-ray amorphous Pd coated Mg nanoblades were reported to desorb hydrogen starting from 380 K , (Tang *et al.*

2008). Similarly, Oguchi *et al.* 2008 showed that desorption of hydrogen from Mg-Ni X-ray amorphous thin films was completed at temperatures not greater than 473 K. ^{1,2}Qu and co-workers 2009, have recently shown that 100 nm thick as-deposited X-ray amorphous Mg/Pd films can desorb hydrogen effectively even at room temperature in air (¹Qu *et al.*, 2009).

Regarding the high cost of Pd, Wang *et al.* 2004 replaced Pd with mishmetal-Ni_{3.5}(CoAlMn)_{1.5} alloy. Alternate layers were deposited and hydrogenation was performed. These multilayers were reported to absorb hydrogen at 523 K under 2 bar hydrogen. Hydrogen release; however, was possible at 523 K, much higher than those reported above.

2.5 HYDROGEN IN AMORPHOUS STRUCTURES

Most of the studies given above consider the reaction of hydrogen with crystalline materials. In this context, it is useful to review the literature on the interaction of hydrogen with amorphous materials.

It is well known that α -MgH₂ is formed in tetragonal symmetry, H atoms occupy 4f (0.304, 0.304, 0) and Mg atoms occupy 2a (0, 0, 0) lattice sites. However, it is a challenge to clarify where and how the hydrogen atom localizes in an amorphous structure.

Considering this question, Rush *et al.* 1980 examined TiCuH both in crystalline and amorphous form using molecular vibration spectroscopy. They observed that in both situations hydrogen peak was obtained at the same frequency, but in broader fashion for the latter. This broadening was attributed to the deformation of the tetrahedral hydrogen positions as well as to the fluctuation in chemical composition for the amorphous structure.

Kircheim *et al.* 1982 proposed that since amorphous alloys lack long-range order (LRO), hydrogen atoms might occupy a wide variety of interstitial sites, resulting from a distribution of both chemical and geometrical configurations in the amorphous structure. According to Sakamoto *et al.* 1988 diffusivity of hydrogen is different in ordered and disordered states. They attributed this to the potential energies in the interstitial sites and also the jump rate of hydrogen between those sites during the migration process. Eliaz *et al.* 1999 proposed that hydrogen diffusion coefficient deviates from Arrhenius law in amorphous materials. They explained this deviation by the temperature dependence of short range order, in metallic glasses.

Kijek *et al.* 1980 and Ahmadzadeh and Cantor 1981 have studied the diffusion rate of hydrogen in amorphous and crystalline (FCC) structures. According to Kijek *et al.* 1980 due to the size distribution of the interstitial sites in amorphous materials, the diffusion of interstitials is not random. In this approach, the diffusivity of a given atom in an amorphous material is expected to be smaller than in case of crystalline structures, since the diffusing atoms may be trapped in bigger interstitial sites. On the other hand, Ahmadzadeh and Cantor 1981 suggested that if the diffusion of interstitials are controlled by the rate of escape from octahedral sites, the effective activation energy for diffusion should be similar in amorphous and in FCC structures. Studies of Stolz *et al.* 1986 and Bowman *et al.* 1983 showed that with smaller average values of activation energy, hydrogen diffusion is faster in glassy samples as long as hydrogen to metal ratio, $[H/M] > 0.01$. In a study on amorphous FeTi films, considering the kinetics of hydrogen absorption, Nakamura 1984 calculated that hydrogen diffusion coefficient and solubility as 10^3 and 10^2 times larger than the corresponding values in crystalline state, respectively.

In crystalline alloys, if a phase transformation occurs in the metal-hydrogen system, the chemical potential of hydrogen (or its pressure) remains constant within the two-phase region, although the total hydrogen concentration increases. This is reflected by the occurrence of plateau in PCT diagrams. However, one of the most characteristic changes in going from crystalline to amorphous alloys is the

disappearance of this plateau, (Eliaz and Eliezer 1999). This has been reported in amorphous Ni(Zr,Ti) alloys, (Spit *et al.* 1979 and 1980). The lack of plateau was attributed to the low temperature hydride formation and the lack of phase separation. Still it is important to mention that amorphous alloys upon hydrogenation are subject to similar volume change as their crystalline counterparts, (Maeland *et al.* 1980). For example, Samwer and Johnson, 1983 measure 13 % volume change in Zr-Pd glassy metals by hydrogen absorption.

According to Maeland *et al.* 1980 and Suzuki 1983 amorphous alloys can absorb more hydrogen compared to their crystalline counterparts. Eliaz and Eliezer 1999 attributed this to the limited occupancy sites for hydrogen in crystalline materials. On the contrary, Bowman 1988 claimed that, due to disordered structure of amorphous systems, there is limited number of sites for hydrogen occupancy, which would lead to less hydrogen storage in amorphous materials.

As can be seen from the discussions given above, how crystallinity and amorphous structures influences metal-hydrogen reaction is not clear at all. In general, amorphous structures were reported to have improved properties when compared to their crystalline counterparts. Some of these reports are given below;

Liu *et al.* 1997 reported that amorphous phase in mechanically alloyed Mg_xNi_{100-x} can absorb and desorb hydrogen electrochemically at room temperature. Iwakura *et al.* 1999 attributed the enhanced sorption characteristics of ball-milled Mg_2Ni -Ni composites, to the appearance of the homogeneous amorphous structure over the whole alloy particles. Ovshinsky and Fetchenko 1996 showed that thin film compositions based on Mg-Ni amorphous or amorphous-like films are preferable for Ni-MH rechargeable batteries, in terms of high storage capacity. In a similar study ¹Chen *et al.* 2002 calculated that the sputter deposited $Mg_{1.2}Ni_{1.0}$ thin films have a reaction enthalpy of $\Delta H_d = 42 \text{ kJ/mol H}_2$. This value is nearly half of the enthalpy value of polycrystalline Mg_2NiH_4 . The amorphous phase in the film is stable up to 523 K. Orimo *et al.* 1997 showed that amorphous Mg-Ni obtained by mechanical alloying can desorb hydrogen at 373 K with 50 at. % Ni. In addition to this, they

observed faster kinetics for nanostructured Mg₂Ni including amorphous Mg-Ni. Spassov and Köster 1999 stated that nano-crystalline Mg-based structures when embedded into amorphous matrix, showed better kinetics compared to fully amorphous ones, though the capacity was higher in the latter.

Another advantage of amorphous structures is their resistance to pulverization. This has been demonstrated by Spit *et al.* 1979 and Miyamura *et al.* 1993 on amorphous Ni(Zr,Ti) alloys and amorphous LaNi₅ thin films. A similar report has been made by Hu *et al.* 1996 on mischmetal-Ni amorphous films.

2.6 CAPACITY MEASUREMENTS

Conventional capacity measurement methods such as volumetric, (Güvendiren *et al.* 2004), or gravimetric, (Feenstra *et al.* 1986), are suitable for powder or bulk samples. Those are not applicable to thin film samples because of insufficient sample quantities. It is possible to use higher amount of thin film sample for measurements but obviously this approach has practical difficulties. On the other hand, a number of direct and indirect alternative methods have been developed to measure the hydrogen concentration in thin films. Direct methods are; nano-gravimetric measurement employing a quartz crystal microbalance (QCM) (Bucur and Flanagan 1974), hydrogen depth profiling by ¹⁵N nuclear resonance technique (Hjörvarsson *et al.* 1991), measurement of the neutron reflectometer spectrum, (Rehm *et al.* 1999), measurement of lattice expansion by X-ray diffraction (Zabel and Weidinger 1995), and electrochemical measurement (Pundt and Kirchheim 2006).

Electrochemical measurement is an easy method, but has limited scope due to the electrolyte wetting (Pundt and Kirchheim 2006). ¹⁵N nuclear resonance technique requires a vacuum chamber and out-gassing that occurs under vacuum can be a problem during measurements, (Rehm *et al.* 1997). The measurement of lattice expansion by X-ray diffraction is complicated due to non-linear effects (Zabel and

Weidinger 1995). Finally, quartz crystal microbalance technique is an *in situ* method and sometimes may not yield reproducible results because of frequency fluctuations due to environmental aspects such as temperature and pressure changes, (Lim *et al.* 2007). On the other hand, a novel Sievert's type apparatus was reported in a recent study, which allows volumetric measurement corresponds to an accuracy of better than 0.15 wt. % for a 2 mg sample, (Lee *et al.* 2008). However, produced thin films in this study were all in the range of 0.3 to 1 mg depending on the thickness under consideration.

Indirect methods are based on a correlation between the hydrogen concentration and optical or electrical property changes during measurements. Even the reaction enthalpies can be calculated by using the relationship between hydrogen content, hydrogen pressure, transmittance and temperature data for thin films using the optical measurements, (Gremaud *et al.* 2007).

The early resistivity measurements during hydrogen sorption of Pd coated Mg thin films, was published by Hjort *et al.* 1996. They investigated the effect of hydrogen concentration on the resistivity of the film. Gravimetric (*i.e.* QCM) or volumetric measurements were also performed simultaneously with resistivity measurements. Authors stated that there is a linear relationship between resistivity of the film and hydrogen concentration up to $[H/Mg] \approx 0.4$. In a similar study, Ingason and Olafsson 2005 have measured hydrogenation behaviour via resistance change by gradually increasing the pressure in steps. Based on this idea, the deviation in pressure resistance curve from linearity was considered as the beginning of the plateau pressure.

CHAPTER 3

THIN FILM CONDENSATION PHENOMENA

3.1 INTRODUCTION

The nucleation and the growth of thin films generally occur via condensation mechanism from the vapor phase. Individual atoms or polyatomic species arriving to the substrate surface incorporates to a series of reaction before the growth of the film takes place. There are many process parameters, depending on the equipment conditions, that may be effective on the early stages of the growth (Pauleau 2002). These parameters can be listed as; the purity of the source and substrate materials, the composition and crystallographic orientation of the substrate, deposition rate, impurity concentration and the pressure of the chamber and the substrate temperature.

3.2 CONDENSATION

Thin film deposition may be considered to occur in six sequential steps (Smith 1995). These are a) the adsorption of atoms or molecules to the substrate, b) diffusion of adsorbed molecules or atoms incorporating into the film, c) reactions between the atoms and the surface to form the initial structure of the film, d) initial clustering *i.e.* nucleation and, e) film growth resulting in final structure and morphology. In this step depending on the deposition conditions, amorphous, polycrystalline and single crystal structures may be formed. Finally, f) modifications

which may arise as a result of diffusion taking place in the bulk of the film. In general, the final resting sites of adatoms are defect sites such as vacancies, growth ledges, or pre-existing nucleus on the substrate/film.

According to Pauleau 2002, a very short time in the order of a lattice vibration time of picoseconds is required for equilibrating adatoms with the surface atoms. This corresponds to a quenching rate of about 10^{15} K s^{-1} . Fig. 3.1 given below summarises the basic atomistic nucleation and growth process on substrate surface during vapor deposition. The details of these reactions are discussed in the following section.

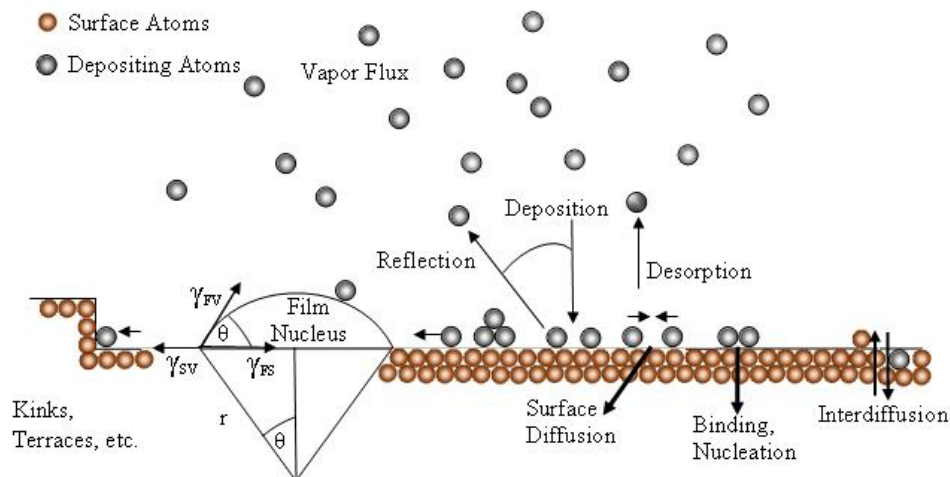


Figure 3.1 Schematic of basic atomistic nucleation and growth processes on substrate surface during vapor deposition. (Adapted from Ohring 2002, Smith 1995 and Venables *et al.* 1984)

It is commonly believed that, (Smith 1995, Berry *et al.* 1968, Ohring 2002), upon arrival of the atom within a few atomic distances to the surface, an attraction is exerted on the atom by interaction with the surface molecules or atoms, due to the Van der Waals forces. After this step, there are possible reactions that may occur depending on the energy considerations. Reflection of the atom is possible when the atom retains most of its kinetic energy and has only a short stay on the surface in the

order of picoseconds. Physisorption or weakly adsorbed state occurs when the greater portion of the perpendicular component of the momentum is dissipated to the surface. There is no potential energy barrier to overcome in physical adsorption, so the heat of desorption is the same of heat of adsorption which is usually less than 0.25 eV (Ohring 2002). In this state, atoms still have enough energy to migrate along the surface. The physisorbed molecule/atom is mobile on the surface except for very low substrate temperatures. This allows diffusion of the atom or molecule through the atomic sites of the surface, before chemisorption state develops, *i.e.* establishment of bonding with surface atoms. Heat of chemisorption, usually 1-10 eV, is greater than heat of physisorption. Activation energy is involved in chemisorption and a potential barrier must often be overcomed before chemisorption takes place. It is also possible for the diffusing species by gaining enough energy to re-evaporate again and get incorporated into the vapor phase. All these are continuous processes that take place simultaneously during the film formation.

3.3 NUCLEATION AND GROWTH

Vapor condensation to form a thin film is a classical case of heterogeneous nucleation (Kaiser 2002). The nucleation stage starts, after a sufficient number of atoms or molecules are condensed on the surface and may continue throughout the deposition process. Most studies agree that the demarcation line between the end of nucleation and the onset of nucleus growth is not well defined (Ohring 2002). According to Kaiser 2002 nucleation takes place at high supersaturation S , defined as;

$$S = \frac{p}{p_0} \quad (3.1)$$

where p is the vapor pressure of the depositing material at temperature T and p_0 is the equilibrium vapor pressure of the substrate material at its temperature T_s . Deposition rate R is related to p as;

$$R = p / (2\pi mkT)^{1/2} \quad (3.2)$$

where k is the Boltzmann's constant, m is the molecular weight, and T is the temperature of the evaporating source. The value of S in Eq. 3.1 is extremely high $\approx 10^5$ - 10^{50} for deposition to occur.

Nucleation is a non-equilibrium process. There are a number of proposed theories for nucleation process. One of which is the mean-field nucleation theory. This theory includes adparticle dynamics on strained surfaces (Grima *et al.* 2007). Capture zone fragmentation model was proposed by Mulheran 2004. This model is describing the dynamics and the scaling of the saturation island density with deposition rate as well as the island size distribution. Shi *et al.* 2006 have reported data comparing these theories with the kinetic Monte Carlo simulations.

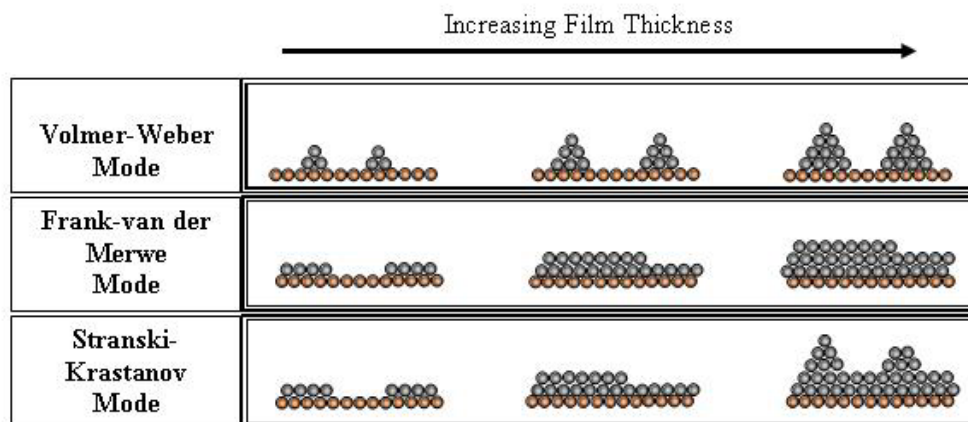


Figure 3.2 Three basic modes of thin film growth. (Adapted from Bauer 1958)

There are three basic modes of thin film growth as given in Fig. 3.2, (Bauer 1958). These are;

1- Island growth (Volmer-Weber) mode. This mode occurs when adatoms are strongly bound to each other rather than to the substrate atoms. This is often the case

for metallic films deposited on to insulating or contaminated substrates (Hirth and Moazed 1967).

2- Layer-by-layer growth (Frank-van der Merwe) mode. This growth is valid when the depositing atoms establish stronger bonds with the substrate atoms. It leads to the homoepitaxial growth on a clean substrate surface, as is the case for metal-metal and semiconductor-semiconductor systems (Neugebauer 1970).

3- Mixed growth (Stranski-Krastanov) mode. For this mode, the strain energy per unit area of the film overgrowth is large with respect to surface energy of the film permitting nuclei to form above the initial layers. This is observed in metal-metal and metal-semiconductor systems (Wagner and Voorhoeve 1971, Venables *et al.* 1984).

In fact, Fig. 3.1 clearly demonstrates the simple law governing the basic atomistic nucleation process on substrate surface during vapor deposition and the mode of the growth. By using the relationship between the surface tensions in equilibrium;

$$\gamma_{SV} = \gamma_{FS} + \gamma_{FV} \cos \theta \quad (3.3)$$

We can obtain an equation which is known as Young's equation. For island growth $\theta > 0$, and therefore,

$$\gamma_{SV} < \gamma_{FS} + \gamma_{FV} \quad (3.4)$$

In the case of layer growth, depositing atoms wets the surface and $\theta \approx 0$, and therefore,

$$\gamma_{SV} \geq \gamma_{FS} + \gamma_{FV} \quad (3.5)$$

Finally for the mixed growth initially;

$$\gamma_{SV} > \gamma_{FS} + \gamma_{FV} \quad (3.6)$$

should be satisfied.

3.3.1 Island Growth Mode, Three-Dimensional

Island growth mode is possible when the contact or wetting angle “ θ ” is greater than “0”. This condition yields *Eq. 3.4*. This mode includes the nucleation of the condensed phase into smaller distinct clusters on the surface. Separate three-dimensional island formation from small clusters by further deposition leads to the coalescence of those islands to form a continuous film structure. Bauer and van der Merwe 1986 include the strain energy to the discussion and stated that if the layer-by-layer growth is not fulfilled from the very beginning, then island growth occurs immediately on the substrate.

3.3.2 Layer-by-Layer Growth Mode, Two-Dimensional

This type of two-dimensional growth occurs corresponding to complete wetting of the surface, in other words when the depositing atoms exhibit a greater bonding strength with the substrate atoms. Wetting angle is then approximately “0”. Layers of material grow on top of another. This means that the free-energy barrier for nucleation is zero (Pauleau 2002). According to Bauer 1958 when the strain and surface energy considerations are satisfied the layer-by layer growth proceeds independent of the film thickness.

When the above conditions are not satisfied, the surface energy of the substrate may be modified by depositing a transition layer between the substrate and the film. For instance in case of Cr or Ti transition metal coating on a glass substrate eliminates the wetting problem between glass substrate and noble metal film, providing layer-

by-layer growth of noble metals on glass, instead of island growth (Xilian and Jianda 2006).

3.3.3 Mixed Growth Mode, 2D to 3D Transition

This mode is a combination of layer-by-layer growth and the island growth modes. The transition occurs after the formation of a few monolayers, and then layer-by-layer growth become unfavourable and the atoms began to form 3D islands on the previous layer. The reason why a transition occurs is not completely understood. Ohring 2002 and Pauleau 2002 attributed this transition to the strain energy release that accumulates in the growing film due to film-substrate mismatch. Further, Pauleau 2002 stated that release of stresses between the substrate and the deposited material leads to the formation of defects in the film that act as heterogeneous nucleation sites for the island growth mode.

The transition to island mode is well described by Bauer *et al.* 1977 who studied Ag deposition on W (110) substrate. He measured the binding energy of Ag atoms on W surface approximately as 3.15 eV. This value is slightly lower than that of the bulk sublimation energy, *i.e.* 2.90 eV. The difference though enough to favour the formation of monolayer coverage initially. Then the subsequent adsorption energy of depositing Ag atoms on that monolayer and on the second monolayer was measured as 2.91 and 2.80 eV. They concluded that this change in energy is the reason for the transition to island nucleation after the second monolayer.

3.4 GROWTH MODES OF Mg THIN FILMS

According to Kaiser 2002, growth of metallic films usually starts with islands. This has been demonstrated by Galkin *et al.* 2008 during deposition of 0-0.032 nm Mg films on Si (111) substrate at room temperature. They first observed 2D than 3D islands of Mg₂Si. The same phenomenon was also reported by the authors Quin and

Sona 1991, An *et al.* 1995 and An *et al.* 1996. In a study considering Mg deposition, Lee *et al.* 2007 claimed that the growth mode depends on whether the deposition of Mg occurs in multistep or in a single step. According to their observations, if multistep deposition is used, round Mg islands were formed on an amorphous Mg₂Si layer, while in single step, hexagonal islands were obtained.

Pezzagna *et al.* 2008 showed that it is possible to grow Mg in a layer-by-layer epitaxial growth mode, at room temperature on GaN (0001) surface. It was observed that, 2D islands largely coalesced at 0.90 monolayer (ML) coverage of the surface. Similar observation was made by Schiller *et al.* 2004. They deposited Mg on W (110) substrates. They explored the growth of Mg films by photoelectron spectroscopy. Study demonstrated the development of highly perfect, crystalline Mg in hexagonal closed packed (HCP) bulk structure, with (001) basal plane parallel to substrate surface. They stated that above 3 ML, Mg grows layer-by-layer and at room temperature this mode of growth can continue up to 80 ML in the least.

As discussed by Lee and Rigsbee 1986, the kinetics of thin film nucleation are almost always affected by the surface defect density. This was also stated for Mg films grown on different substrates (Pezzagna *et al.* 2008) and at different temperatures (Aballe *et al.* 2007). They observed that Mg nucleates preferentially on the steps or terraces and mimics the underlying surface at the very early stages of growth. At this stage adatoms are highly mobile and they have enough energy even for re-evaporation. Aballe and co-workers stated that starting from the second monolayer, the growth proceeds and with the increasing film thickness, memory of the substrate symmetry is gradually lost.

Tegenkamp *et al.* 1999 found a strong dependence of growth mode on substrate temperature. In depositing Mg on Ag (100) substrate, below 200 K growth of the film proceeds layer-by-layer, this is transformed into a Stranski–Krastanov growth mode at a surface temperature of 300 K. At this substrate temperature after completion of the first monolayer, three-dimensional islands formation was observed. In a similar method, Aballe *et al.* 2007 deposited Mg on W (110)

substrates and observed that Mg growth proceeds as layer-by-layer mode from RT up to 450 K. They further stated that, above 450 K multilayer re-evaporation of Mg takes place leaving behind the interface Mg monolayer, which does not desorb completely even at 700 K.

Reevaporation of Mg from the substrate is a well known phenomenon due to very high vapor pressure of Mg even at low temperatures, (thermal equilibrium vapor pressure of Mg at 473 K is about 10^{-7} torr), (Glang 2002). John *et al.* 1996 calculated the reevaporation rate of Mg at 473 K as 0.076 Å/s, and they further claimed that no net accumulation of Mg deposits could be obtained on Si (111) substrates at ≥ 473 K via reactive evaporation method. Re-evaporation is taking place before atoms are incorporated in the film *i.e.* while they are migrating in the surface as well as from the film itself (Serikawa *et al.* 2004 and Frederick *et al.* 2003).

3.5 STRUCTURE-ZONE MODELS

Microstructures of thin films are often been explained by the so-called structure zone models, Fig. 3.3. Structure zone model, (SZM), was first introduced by Movchan and Demchishin 1969. They considered normalized growth temperature T_S/T_M , as the main parameter for the final film morphology. In this model they defined 3 regions; zone 1, 2 and 3 and calculated transition temperatures between the regions. T_1 , the transition temperature from zone I to zone II have a value of $0.3T_M$ for metals and $0.22-0.26T_M$ for oxides. T_2 is between zone II to zone III and have a value of $0.45-0.5 T_M$ for both metals and oxides. Films belong to zone I typically contain tapered crystallites with domed tops, separated by open voided boundaries and consists of textured and fibrous grains. At zone II grains are columnar and separated by dense inter-crystalline boundaries. Grains are uniform and columnar with diameters exceeding the thickness of the films in zone III.

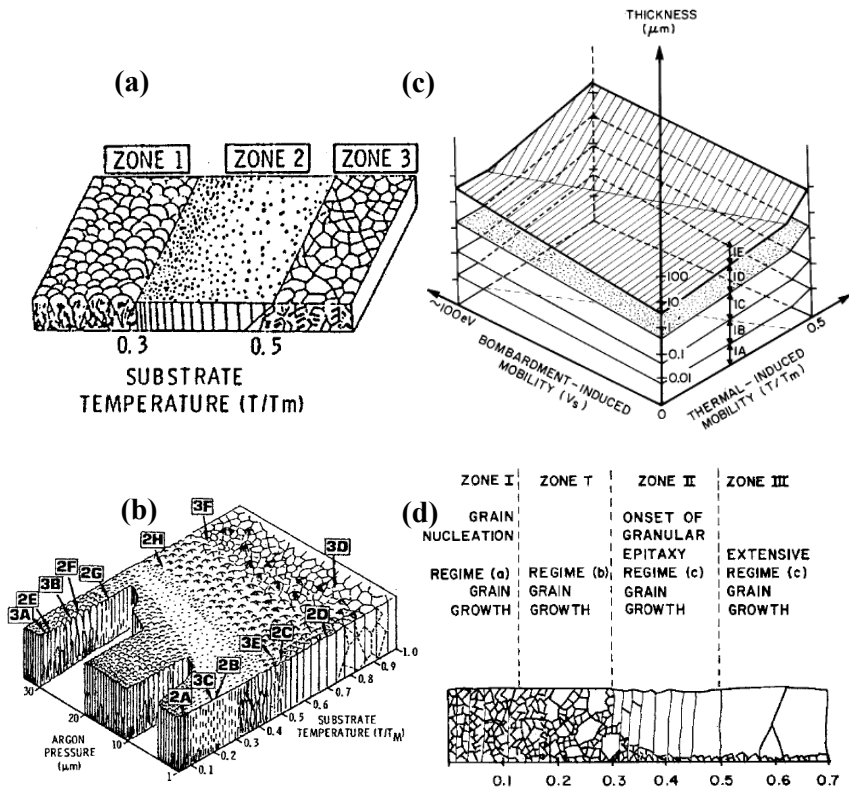


Figure 3.3 Structure zone models proposed for evaporated and sputtered thin films, (a) Movchan and Demchishin 1969, (b) Thornton 1974, (c), Messier *et al.* 1984, (d) Grovenor *et al.* 1984 and Hentzell *et al.* 1984.

The above model proposed by Movchan and Demchishin has been modified by Hashimoto *et al.* 1982 and Okamoto *et al.* 1989, by introducing other parameters such as surface diffusion, incidence angle of the vapor beam, adsorbed impurities, surface recrystallization and etc.

Fig. 3.2 (b) refers to a model proposed by Thornton 1974 and 1975 for sputter deposition, Fig. 3.3 (b). This model is the adaptation of the Movchan and Demchishin's model for sputter deposited films. He has introduced argon pressure as a variable. According to Thornton, at low Ar pressures, there is an additional zone between zone I and II. This zone consists of densely packed fibrous grains and defined as zone T, *i.e.* transition zone.

Messier *et al.* 1984 revised the previous zone-models to account for the evolutionary growth stages of structure development as well as the separate effects of thermal- and bombardment-induced mobility for sputtered thin films, Fig. 3.3 (c). This model assumes zone T as a lower subzone within zone I. It may be considered as a specific SZM for a particular film thickness when examined through a horizontal slice. For example, zone 1A on the figure refer to the smallest size level (1-3 nm) while zone 1E represents the bigger columns with size of 300 nm columns.

A more recent SZM has been published by Grovenor *et al.* 1984 and Hentzell *et al.* 1984. This model has classified the microstructure in four characteristic zones; zone I, T, II and III, Fig. 3.3 (d). They considered the substrate temperature as the main parameter for the final film morphology. The model discusses on the evolution of grain structure in metallic thin films based on the mobility of individual grain boundaries.

At $0.15 T_M$, where the mobility of deposited atoms is low, there is a homogeneous equiaxed grain structure with grain diameters in the range 5 to 20 nm. At these temperatures, according to the authors, due to very low mobility, arriving atoms sticks where they impinge to the substrate. Their calculations show that the critical nuclei radius for homogeneous nucleation of solid Ni at $0.15T_M$, corresponds to the size of a single atom.

They further explained that the difficulty is not in explaining the nucleation of a solid phase, but accounting for its crystallinity. The maximum diffusion length of a deposited atom before being covered with the depositing neighbouring atoms is about one atomic distance. They stated that even under these conditions crystalline grains are formed instead of amorphous structure. This was attributed to crystallization of a small group of atom athermally resulting in the release of the heat of crystallization. This energy was found to stimulate further crystallization until neighbouring nuclei impinges. Then the grain size is governed by the density of the nuclei.

According to this model the microstructure of the film changes from equiaxed shape to columnar at Zone T ($0.15 T_M < T_S < 0.3 T_M$). The transition is attributed to the onset of surface diffusion of adatoms, which can migrate to energetically favourable sites before being covered with additional arriving atoms. In addition, under these conditions, certain grain boundaries become mobile resulting in recrystallization or grain growth process. Secondary recrystallization yields a grain structure with bimodal size distribution. The secondary recrystallization process is driven by the energies of surface planes which also results in the formation of the fiber texture in the thin films such as {111} for FCC and {110} for BCC metals (Gravenor *et al.* 1984) and basal plane for HCP metals. Depending on deposition temperature, enough energy may be provided which leading to a change in preferred orientation. Such a texture formation has been reported by Bunshah 1974 for HCP film. In case of Be which had (002) orientation at low temperatures was changed to (1120) by deposition at elevated temperatures.

Returning to the model, the structure is columnar in zone II and these columns are produced by grain growth. Substrate temperature provides sufficient surface mobility to the atoms for diffusion resulting in an increase in grain size. Diameters of these columnar grains are smaller than the thickness of the film. With increasing substrate temperature and the film thickness bulk diffusion takes place. As a result, diameter and the size of the columns increase. Therefore, zone III consists of uniform grains with diameters larger than the film thickness.

It should be pointed out that there are other factors that are important in the development of film morphology that are not included in the above models. One of these is the impurity concentration which can greatly modify the structure that evolves in thin film deposition, independent of substrate temperature. Such an effect was reported by Barna and Adamik 1998. Fig. 3.4 schematically shows the influence of oxygen content in the environment during Al deposition. With increasing impurity level a significant refinement was observed in the structure.

The other is substrate topography. This topography is influential in the structure evolution. Rough surfaces with various defects (peaks, valleys) exhibit preferred adsorption, nucleation, and growth sites, lead to shadowing effect on the adatoms and more columnar open voided microstructures are formed (Pauleau 2002).

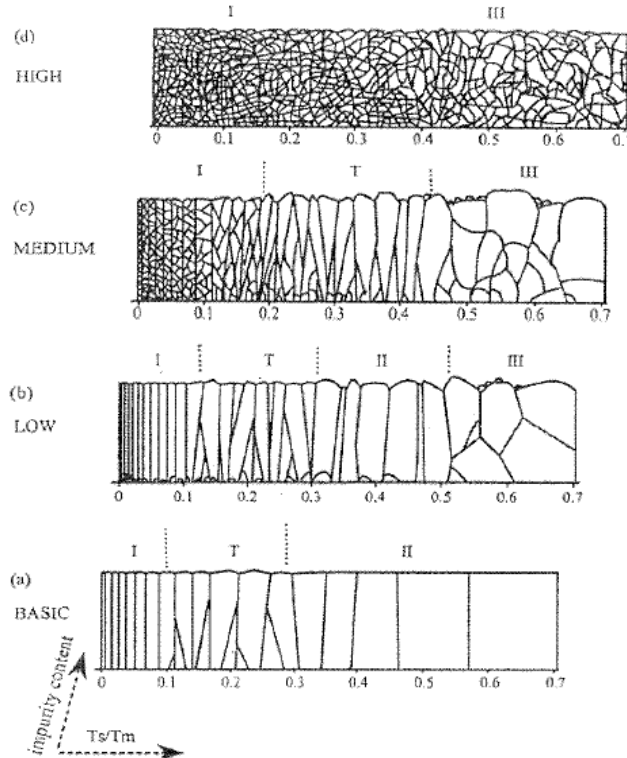


Figure 3.4 Basic and real-structure zone models for low, medium, and high impurity concentrations. (Adapted from Adamik *et al.* 1995)

Shadowing is a geometrical interaction between the depositing atoms and the roughness of the surface. While the beam is uni-directional, this effect is more important at low substrate temperatures where the adatom mobility is highly restricted (Kaiser 2002). On the other hand, relatively high substrate temperatures, provides sufficiently fast kinetics for surface diffusion processes to surmount topological effects and finally, thin films with relatively smooth surfaces can be deposited (Movchan and Demchishin 1969).

3.6 AMORPHOUS ALLOYS

Glass is basically a non-crystalline or amorphous solid formed by continuous cooling of a liquid. During the formation, temperature decreases across the glass transition temperature T_g , the viscosity increases rapidly but continuously, while at the same time the specific volume and configurational entropy decrease continuously. Amorphous or glassy state can only be achieved if the formation and growth of competing crystalline equilibrium phases can be avoided. Thus, the glassy state is not the equilibrium state of solids.

Inoue 1995 have proposed three major contributing factors for the transformation of metallic melts to glass; namely the atomic size mismatch, high negative heat of mixing, and multicomponent alloy. Choosing elements for an alloy system with appropriate atomic size ratio is a common practice for increasing the tendency for amorphization. In this way, the atomic packing density increases in the melt. Experiments show that for an easy glass formation, selected elements should have an atomic size mismatch of at least 12-15% (Liou and Chien 1987). Heat of mixing concept depends on Miedema's model and involves the calculations of the formation enthalpy of amorphous phase ΔH^{amor} , solid solutions ΔH^{ss} , and intermetallic compounds ΔH^{inter} . A higher absolute value of ΔH^{amor} and a smaller enthalpy difference between the intermetallic phase and the amorphous phase increases the glass forming ability of the alloys (¹Xia *et al.* 2006). Finally, proper alloying element addition is an accepted approach to achieve amorphous structures. This was reported by Süer *et al.* 2009 for Ti-Cu-X multicomponent alloys. The study showed that the alloying element X among the candidates, which reduced critical cooling rate, is more suitable for enhancing the glass forming ability of the alloy.

Two criteria for glass formation/amorphization have been proposed. First one is the kinetic criterion, which considers the cooling rate. This is simply the prevention of nucleation and therefore crystallization by the effect of quenching. The second is the structural criteria that take into account the bonding, atomic size effect, and

geometric considerations. It is important to note that, these two criteria are strongly related to each other.

3.6.1 Kinetic Criteria for Amorphous Phase Formation

Kinetic criteria consider parameters like nucleation, cooling rate and characteristic temperatures, such as reduced glass transition temperature and try to make correlations between these parameters and glass forming ability of a melt.

In such criteria, Turnbull 1969 have used the reduced glass transition temperature as the core parameter for amorphization. Reduced glass transition temperature, T_{rg} ;

$$T_{rg} = \frac{T_{ig}}{T_m} \quad (3.7)$$

where T_{ig} is ideal glass transition temperature and is slightly lower than the observed glass transition temperature T_g , and T_m is the melting temperature (equals to T_l , liquidus temperature for an alloy and melting temperature for pure substances) respectively.

Turnbull's proposal was based on the simple-nucleation theory and aims to estimate zero nucleation condition for a glass formation. The study defines dimensionless parameters α and β ;

$$\alpha = \frac{(N_o V)^{1/3} \gamma_m}{\Delta H_m^f} \quad (3.8)$$

and,

$$\beta = \frac{\Delta S_m^f}{R} \quad (3.9)$$

where, γ_m is the interfacial energy per molar surface area, ΔS_m^f is the molar entropy of fusion, N_o is the Avogadro's number, V is the molar volume in the crystal, ΔH_m^f is the molar heat of fusion and R is the gas constant.

For a typical metal, α takes a value of 0.4-0.5 and $1/3$ for non-metals. β is near 1 for metals (Chen *et al.* 1980). Turnbull claimed that liquids with $\alpha\beta^{1/3} = 0.9$ should readily form glasses, while for those with $\alpha\beta^{1/3} < 0.25$ it should be impossible to suppress crystallization. Thus, glass formation is promoted by values of larger interfacial tension and entropy of fusion (Chen *et al.* 1980).

Besides quantitative estimation, Uhlmann 1971 and Davies 1976, based their calculations on the possibility of formation of a small amount of crystalline phase in amorphous matrix and proposed a qualitative estimate of the critical cooling rate for glass formation. They used theory of nucleation and growth, suggesting a sufficient cooling rate such that the melt can be undercooled substantially to retard the formation and growth of crystal nuclei and this prevent crystallization.

For a small value of X , (volume fraction of crystallized material) the simplified equation can be written as;

$$X = \frac{\pi}{3} I u_c^3 t^4 \quad (3.10)$$

where, u_c is the crystal growth rate, I is the nucleation frequency and t is the time taken to transform X . Finally combining nucleation, crystal growth rate and Johnson-Mehl-Avrami isothermal transformation kinetics, Uhlmann and Davies obtained an equation giving the transformation time to achieve a small fraction of crystal X . This equation as given by Ge *et al.* 2007 in the form of:

$$t = \frac{9.3\eta}{kT} \left\{ \frac{a_0^9 X}{f^3 N_V} \times \frac{\exp(G^*/kT)}{1 - \exp(-G_m/RT)} \right\}^{1/4} \quad (3.11)$$

where k , N_V and T are Boltzmann's constant, number of atoms per unit volume and transformation temperature, respectively. G_m is the molar free energy driving force for liquid to crystal growth, G^* is the free energy barrier for nucleation of a spherical nucleus and expressed as;

$$G^* = \frac{16\pi}{3N_0} (\gamma_m^3 / G_m^2) \quad (3.12)$$

and,

$$G_m = H_m^f (T_m - T) / T_m \quad (3.13)$$

which is simply equal to $\Delta H_m^f \Delta T_r$.

By using those relationships given above one can construct a TTT curve. Once this curve is obtained, the critical cooling rate q_{rc} , can easily be estimated by using the equation;

$$q_{rc} = \frac{(T_m - T_n)}{t_n} \quad (3.14)$$

where T_n and t_n are the nose temperature and time, respectively. It is clear that amorphization tendency of any material is directly related to this critical cooling rate.

Any parameter or effect which reduces the necessary undercooling will increase the tendency for amorphization. For example, an increase in reduced glass transition temperature drastically lengthens the time at the nose of the TTT curves and then sharpens and shifts the nose to smaller undercooling values, as shown in Fig. 3.5 (Chen *et al.* 1980).

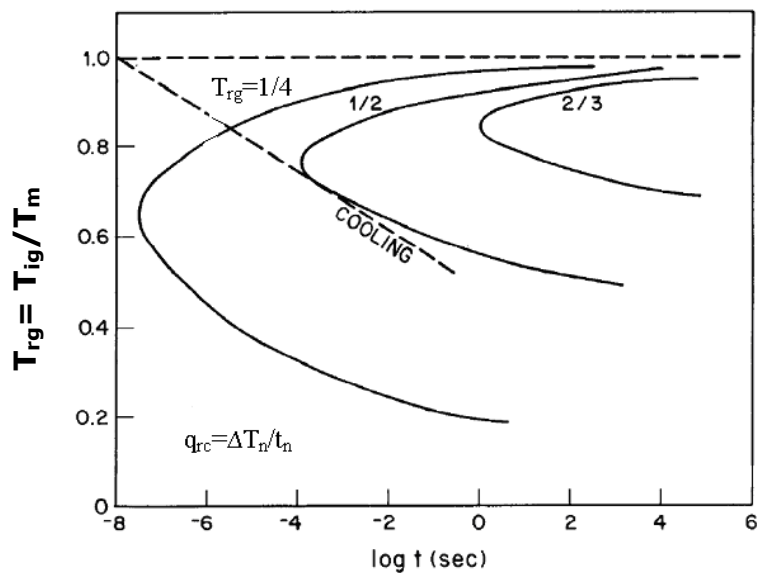


Figure 3.5 Time-temperature-transformation (TTT) curves of metals with various reduced glass temperature $T_{rg} = T_{lg} / T_m$ (Chen *et al.* 1980).

The curves are in good agreement with the experimental values observed for pure metals such as Ni and Pd and metal-metalloid binaries. The critical cooling rate values are 10^{10} K/s and 10^6 K/s in the respective order. Generally, any system with a value of $T_{rg} \sim 0.6$ or above have strong tendency for amorphization.

On the other hand, to represent actual cooling conditions, continuous cooling transformation (CCT) curves are required. This can be made analytically or numerically for actual cooling conditions (Pehlivanoglu 2003).

3.6.2 Structural Criteria for Amorphous Phase Formation

There are a number of studies considering the structural criteria (see Yang *et al.* 2009), in amorphous phase formation. Here, only selected studies will be considered. Elements with similar electronegativity values tend to form solid solutions, which decreases the tendency for amorphization. This is because large solubility of the elements in the competing crystalline phases requires only short

range atomic arrangements. With the increase of electronegativity difference among constituent elements, the formation of certain atomic pairs (*i.e.* clusters) is favoured and the solubility of these elements in the competing crystalline phases is restrained. However, too much difference in electronegativity would lead to compound formation which may prevent amorphization.

Viscosity of the melt is an important variable in terms of liquid stability especially in the glass transition region. During continuous cooling, viscosity of the melt exponentially increases with $\Delta\mu/S_c$ (Cohen and Turnbull 1964). Here, $\Delta\mu$ is the potential energy barrier against the co-operative rearrangement and S_c is the configurational entropy. S_c is approximately constant below T_g , thus $\Delta\mu$ is playing a major role in determining the viscosity of a glass phase at this region. $\Delta\mu$ is related to cohesive energy including repulsive-attractive interactions between the constituent atoms. In this respect, $\Delta\mu$ can be assumed as a measure of formation and stability of the amorphous state.

Hafner 1983 based on the free-volume approach (Cohen and Grest 1979), and entropy crisis model (Kauzman 1948), have estimated the glass transition and liquidus temperature of the glass forming binary alloys. Fig. 3.6 is taken from his study which refers to Ca-Mg binary system. Hafner assumed a lower and an upper limit for T_g , the upper limit based on the entropy-crisis, (T_S), and the lower limit based on a free-volume model, (T_η). In this approach $T_g > T_0$ is the basic criterion. The range of amorphous composition is calculated with two different cooling rates. The results were in good agreement with the experiments.

Experimentally, glass forming binary alloys can be classified in different categories (Cahn 1996). One category is that of the alkaline-earth elements alloyed with elements from groups IB, IIB, IIIB, IVA, VA, VIA. Amorphous alloys in this category cover a wide range of composition.

The other categories include glass forming alloys based on the metalloids. Other than this group, there are glass forming alloys based on the metalloids. These

elements form amorphous alloys with late and early transition metals and noble metals. Early and late transition metals can also form glass when alloyed with each other. Finally, there are alloy systems based on aluminium, lanthanides and actinides.

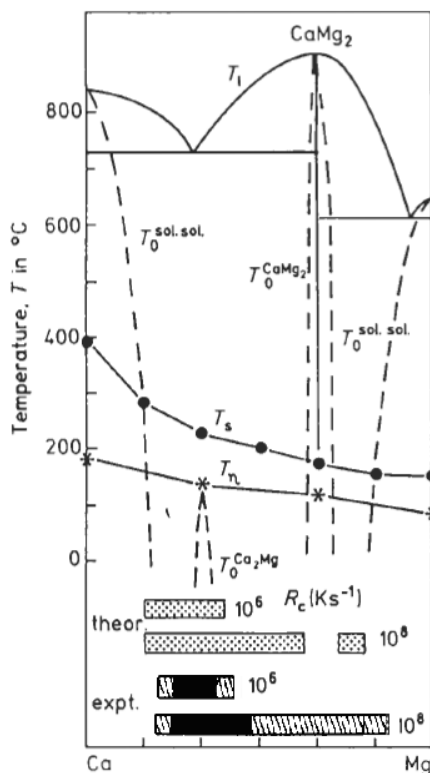


Figure 3.6 Comparison of calculated and experimental glass forming composition range in Ca-Mg system according to Hafner 1983. The shaded region with black colour refers to composition range for complete amorphization.

3.7 AMORPHOUS THIN FILMS

The formation of amorphous phase in metals and alloys is normally achieved by; liquid quenching (splat quenching and melt spinning), co-evaporation of two or more elements by deposition techniques and deposition on substrates which are sufficiently cold to inhibit atomic mobility. Pure amorphous metals may only be prepared by the latter (Reda *et al.* 1982). This is simply because of the rate

differences, achieved by different quenching techniques. In liquid quenching methods, the cooling rate is commonly 10^5 - 10^6 K/s, whereas, a solid grown from atoms in the vapor phase (generated by evaporation or sputtering), the effective quenching rate is as high as 10^{12} K/s (Cahn 1996). Thus, vapor quenching onto cryogenically cooled substrate severely restrict the mobility of adatoms and a disordered atomic configuration has a greater probability of being frozen (Ohring 2002).

Vapor deposition is a non-equilibrium process where condensation from the vapor phase takes place at high supersaturations, directly translating the mono- or polyatomic species to solid state on a substrate surface. The resulting structure may be crystalline, amorphous, or single-crystal depending on the deposition parameters. In case of amorphous structures, atoms will form a random array without arrangement in the long-range order. In such evaporation process the substrate provides good thermal conductivity to absorb the heat of condensation to prevent thermal diffusion, and allows the formation of a random and homogenous solid solution for systems, which have essentially no solubility in the solid or liquid state, since the vapor phase has no miscibility restriction (Takayama 1976).

Ievlev 2004 has proposed that amorphous alloy films consist of nano-composite substructure. In other words, there is no perfect amorphous system with a complete random arrangement. Due to this fact, amorphous structures are identified as systems having short range order over a region of less than $15 \pm 1 \text{ \AA}$.

The temperature of the substrate during condensation is a crucial parameter for the amorphization of the alloy thin films. Surface mobility of the atoms is related to the substrate temperature. This mobility determines the degree of the order in the growing film. In most cases, crystallization requires diffusion of the adsorbed atoms. A sufficiently hot substrate can provide enough energy to overcome the activation energy barrier for diffusion. In such a condition, crystallization process occurs easily and growth starts via surface and bulk diffusion, due to similar activation energies required for both processes (Kaiser 2002). On the other hand, a sufficiently cold

substrate provides a significant amount of quenching. This results in limited diffusion and may freeze the structure in disordered state. However, even in the presence of this restricted diffusion condition, crystallization may still take place via a non-diffusional process (Buckel 1954, Bülow and Buckel 1956, Hentzell *et al.* 1983). Hentzell *et al.* 1983 has measured the activation energy for ordered grain growth under such conditions. The value was far below than any value required for diffusion in metals either on surface, interface or bulk. According to Movchan and Demchishin 1969, this process involves very short migration paths, as a collective motion of atoms producing the required energy for crystallization.

According to Mader *et al.* 1967 pure elements which are condensing under limited diffusion conditions may crystallize by sitting on the potential grooves of the substrate. By this way, they can mimic any periodic array that was already present on a crystalline substrate. These periodic potentials selectively trap atoms and whereby eliminates the possibility for the formation of a disordered structure (Takayama 1976). In case of amorphous substrate, the opposite may be true (Barna and Adamik 1998). The formation of nuclei is randomly distributed due to lack of any periodic array on these substrate surfaces.

Although the degree of quenching is very high with vapor condensation, pure metals with metallic bonding character are difficult to deposit in amorphous state. Most metals have close-packed structures and need only small atomic displacements for crystallization. This was reported by ^{1,2}Vook and Witt 1965 for Cu and Au metals deposited on glass substrates held at 80 K. On the other hand, some of the metalloids and non-metals were reported to be amorphous in pure state when condensed from the vapor phase. These are Ga (Buckel 1954), Ge (Mader 1971), and Sb (Richter *et al.* 1954). Bi is also amorphous but the required temperature is extremely low ≤ 20 K. According to Buckel 1973 amorphization tendency of pure elements is increased with increasing covalent character of the bonds. However, too much increase in covalent character would lead to crystallization.

Introduction of impurity elements play an important role in amorphization (Novick and Mader 1965, Buckel 1969, Nilsson *et al.* 1979). These solutes have a pinning effect during growth, as has been illustrated by Hentzell *et al.* 1983 for Ni-Al co-evaporated thin films. They found that when Ni alloyed with Al, the activation energy required for grain boundary migration was increased to \sim 1.3 eV/atom, whereas the half was sufficient in case of pure Ni. This was attributed to the segregation of Al at the grain boundary regions.

The effect of alloying element on stabilizing the amorphous state depends on the composition. Mader and Nowick 1967 have deposited dilute Cu-Ag and Co-Au alloys in crystalline state on substrates held at liquid helium temperature. The same alloys were amorphous when the composition shifted to higher alloy concentrations. The concentrations were \geq 10 at. % Cu for Sn-Cu (Buckel 1954) and \geq 12 at. % Bi for Pb-Bi (Baier 1968).

In Mg-Cu the composition range for amorphization was extremely wide, *i.e.* 10-80 at. % Cu (Mader 1965). The substrate temperature in this study was 80 K. But according to Mader, depending on the composition, the alloy may also be obtained in amorphous state at room temperature. Another study by Wagner 1969 considered deposition of a specific composition of this binary system, *i.e.* Mg₆₅Cu₃₅ on Be substrates held at 90 K. They found that the alloy forms an amorphous structure with a short-range order size of about 15 Å.

As experimentally measured, during solidification of Mg-Cu system, partial-glass formation composition range varies between 9 at. % Cu and 42 at. % Cu. According to Sommer *et al.* 1980 complete glass formation range covers 12 at. % Cu to 22 at. % Cu. This region was given as 8 at. % Cu to 28 at. % Cu by Detendler *et al.* 1992. This indicates that amorphous Mg-Cu can only be formed for Mg-rich compositions in melts.

On the phase diagram, where Cu₂Mg phase appears, glass formation typically recessive in the competition experimentally, presumably because the nucleation of

this Laves phase is rather easy. This equilibrium compound has a simple structure, of the FCC type of pure Cu, and the similarity between makes the crystallization easy. On the other hand, at Mg-rich side of the diagram, the competing crystalline phase is Mg₂Cu, which is quite complex with 48 atoms in the unit cell, and it has an orthorhombic structure. Thus, a composition around the eutectic always increases the probability of glass formation in this system. Detendler *et al.* 1992 reported that the free energy of the amorphous state near the eutectic composition was lower than the mixture. And also the negative heat of mixing of the elements in Mg-Cu system (*i.e.* -3 kJ/mol) is sufficient to keep Mg–Cu pair together and prevents separation into two phases (Yuan *et al.* 2005).

In compounds and solid solutions, as the order goes from elemental to binary, ternary and higher order, the number of new structure types diminishes. In such a condition, long-range diffusion is necessary for a crystal to nucleate. The introduction of a new element into an alloy also introduces local atomic level strain along with chemical disorder, frustrating crystallisation. Egami 2002 proposed that multicomponent alloys may experience a wide compositional distribution in local glass transition temperatures due to rearrangement of interaction between the constituents. In a theoretical study, Mekhrabov and Akdeniz 1999 examined the effect of ternary element addition on atomic ordering characteristics of Fe-Al binary. They found that the measure of increase in order-disorder transition temperature of Fe-Al alloys is defined by Fe-sublattice substitution of alloying element atoms, as well as the magnitude of the partial ordering energies of Al-X pairs. Ramachandra 1980 has postulated that an alloy with the smallest possible molar volume is most prone to glass formation. Polk 1972 stated that more close packed structures may be obtained by filling of the spaces between randomly packed atoms by smaller radii atoms in multicomponent alloys. Following a similar idea, Inoue *et al.* 1990 examined the effect of Al addition to Fe-B-Si alloy. The study showed that Al addition increased the stability of the supercooled liquid against the precipitation of the crystalline phases. It changed Fe-Fe interatomic distances in the solution. According to Inoue *et al.* this increase lead to more homogenously mixed disordered structure suppressing the nucleation. In the similar context, Behrndt 1970 and Sadoc

et al. 1972 have proposed that small metalloid atoms promote special local arrangement of atoms in alloys, leading to a short-range order. Sadoc stated that activation energy for diffusion in such multicomponent systems requires at least 0.3 T_M independent of film thickness.

As discussed so far the conditions, promoting the tendency for amorphization during condensation, are similar to those given for solidification. Similarly atomic size mismatch is another important parameter for vapor deposited thin films in terms of amorphization. According to Takayama 1976 and Novick and Mader 1965 atoms with different sizes kinetically retard the crystal growth and stabilize the amorphous phase.

When the size ratio approaches to unity amorphization range decreases. This was illustrated by Mader 1965 by comparing amorphization range of vapor quenched Mg-Cu and Co-Cu. The ratio is 1.25 for Mg-Cu and 1.02 for Co-Cu. The former could be obtained in amorphous state depending on the composition, whereas the latter forms an FCC structure for almost all compositions.

Nowick and Mader 1965 developed a hard-sphere model considering the composition, deposition rate and size difference of the depositing species. In a later study Mader and Nowick 1967 deposited Cu-Ag and Co-Au on cryogenically cooled substrates. Based on their model and experimental observations the following conclusions were drawn. i) amorphous structures can be produced in the composition range of 30-70 %, ii) the size difference between the atoms has to be greater than 15 %, iii) binary systems with limited terminal solubility are more prone to amorphization, iv) the deposition temperature has to be lower than 0.3-0.35 T_M , where T_M is the average melting temperature of the two components. These were also confirmed in other binary systems such as: Cu-Mg, Co-Ag, Co-Au, Ag-Cu and Co-Cu.

Systems with lower size differences (*i.e.* size difference lower than 15 %), also reported to be amorphous with co-evaporation method such as, Mg-Bi where the

size ratio is about 6 % (Slowik 1974). This indicates that large atomic size differences significantly increase the ease of formation and stability of amorphous alloys but not sufficient on its own.

Strong atomic interaction between vapor atoms of different sizes may cause a reduction in the undercooling due to depression of T_M (Takayama 1976). This may lead to the formation of amorphous state during condensation. On the other hand, very strong interaction between the atoms was also reported as tendency for the formation of intermetallic phase (Yasuda *et al.* 1994). Glass forming ability of vapor condensates can be given by the following equation,

$$\tau_m = kT_c / h_v \quad (3.15)$$

where τ_m is a degree of atomic mobility at crystallization temperature T_c , and h_v is the heat of vaporization. Thus a depression of T_c results in a reduction in the undercooling and increase the tendency for amorphization (Takayama 1976).

Reduced glass transition temperature T_{rg} , is an important criterion for the prediction of glass forming ability of an alloy system. Originally derived by Turnbull (1969) based on the consideration of bypassing crystal nucleation, this criterion has led to the realization that deep eutectics are preferable for glass formation upon cooling of the liquid. The competition between glass formation and crystalline phase growth controls the glass forming ability of an alloy. And amorphous phase will form when T_{ig} , the ideal glass transition, isotherm is higher than the growth temperature of any of the possible crystalline phases. On the other hand, a number of experimental studies show that the glass-forming region generally deviates from eutectic points (Dubey and Ramachandrarao 1990, Tan *et al.* 2003, ²Xia *et al.* 2006, Xiu *et al.*, 2006, Wang *et al.* 2010). According to Tan *et al.* 2003 if the alloy system has a symmetric coupled zone, the optimum glass forming alloys should be around the eutectic composition, and if the alloy system has a skewed coupled zone, the optimum glass forming alloys should be at an off-eutectic composition. This

requires consideration of the type of the eutectic couple zone in a specific binary, before predicting the best composition for amorphization (Li 2005).

On the other hand, Schwarz and Johnson 1983 have observed that sequentially deposited pure crystalline metal layers may become amorphous when reacted under isothermal conditions. They attributed this glass formation to the large negative heat of mixing of the two metals which led to a low reaction temperature. This low reaction temperature was believed to suppress the formation of possible thermodynamically stable intermetallic phases. This has led to the glass formation over a substantial range of compositions centered in the binary phase diagram *i.e.*, over the intermetallics, rather than near the deep-eutectics for liquid quenched glass (Wu and Li 2009).

CHAPTER 4

HYDROGEN STORAGE IN Mg-BASED CRYSTALLINE THIN FILMS

4.1 INTRODUCTION

Mg can satisfy most of the requirements for stationary and mobile applications with its low density and high gravimetric/volumetric capacity (Hoffman *et al.* 1976, Selvam *et al.* 1986). However, the high stability of the hydride phase and sluggish reaction kinetics hinders those advantages for practical applications. Extensive research for the last four decades on the catalyst materials and mechanical alloying substantially solved the kinetic problem providing faster reaction rates (Bobet *et al.* 2002, Güvendiren *et al.* 2004). On the other hand, higher reaction temperatures because of higher stability of the hydride phase is the main problem still remains to be solved.

Mechanical alloying has been used as the main technique for obtaining a reduction in the stability of MgH₂ (Bouaricha *et al.* 2002, Wang *et al.* 2006, Jurczyk *et al.* 2008). Thin film approach can be used for the same objective as well. Indeed, there are so many studies published in literature based on hydrogen storage in thin films covering the last three decades (Jain *et al.* 1988, Andersson *et al.* 2002, Richardson *et al.* 2003, Pranevicious *et al.* 2004). In pure, 30 µm thick, air exposed Mg thin films, Leon *et al.* (2002), successively stored 7.5 wt. % hydrogen. Absorption was performed at 623 K under 10 bar hydrogen pressure. This study revealed that hydrogen absorption–desorption of Mg follows a nucleation and growth process. Higuchi *et al.* 2002 reported that, nano-structural Pd/Mg/Pd multi-layer films

prepared by magnetron sputtering could absorb at least 5 wt. % hydrogen and desorbed it at 373 K. The improvement on the hydrogen storage properties of Mg film was attributed to the so-called cooperative phenomenon occurring in the Mg/Pd interfacial regions. It indicates that the composite microstructure of multilayer film is also effective for improving the hydrogen storage properties of Mg. Hjort *et al.* 1996 observed a similar reduction in stability at Pd-covered Mg-MgO multilayered thin films. Studies discussed above, imply that the stability of MgH₂ can significantly be reduced via thin film processing if the film chemistry and structure can be suitably tailored.

Regarding the above discussions, in this part of the study hydrogen storage properties of Mg and Mg-based thin films were examined. Effect of the catalyst layer and different film structures and geometries, such as co-deposition and multilayering were also considered as effective parameters on the results. Produced thin films were namely, pure Mg, Mg coated with Pd or Au-Pd, and Mg-Cu. For Mg-Cu, thin films were deposited in two different ways *i.e.* Mg-Cu co-deposited and Mg-Cu multilayered.

4.2 MATERIALS AND METHOD

4.2.1 High Vacuum Deposition System

Thin films were condensed from the vapor phase on microscope slide glass substrates. For this purpose, a resistive evaporation unit was designed and constructed, as shown in Fig. 4.1 (a) and (b). This unit consists of four main parts.

The chamber had a cylindrical shape with an inner diameter of 278 mm. It was formed by a stepwise deformation of 304-quality stainless steel plate. The dimensions of the plate were (1000x200x20) mm. After deformation the two coinciding faces were welded through the vertical axis via TIG welding method. This part was then shaped with a turning machine to obtain the final cylindrical form

with reduced surface roughness. The base lid was prepared from a 304-quality stainless steel disk, which was 372 mm in diameter and 20 mm height. The center of the disk was drilled and machined to obtain a 102 mm diameter hole for the purpose of pump feedthrough connection, *i.e.* a Con-Flat, (CF), 6" flange welded with an extension pipe. Then this disk was welded to the main cylinder to form the base of the vacuum chamber.

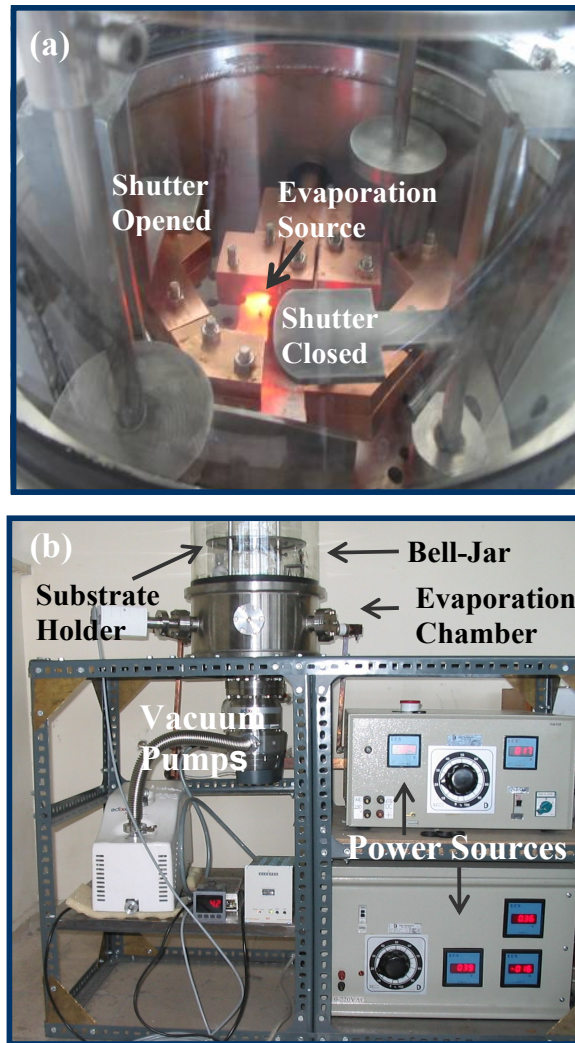


Figure 4.1 Thermal evaporation based on bell jar, (a) evaporation sources, (b) general view.

The cross-section, (top-side), of the chamber was machined carefully to obtain a defect free surface. Polishing was then applied to ensure the sealing between the chamber and the glass bell jar.

The bell jar was 450 mm in height and 300 mm in outer diameter. Wall thickness was 8 mm. An L-type Viton-ring was placed in between the bell-jar and the chamber and vacuum grease was also applied during pumping operations. There were six half-nipels with a $2 \frac{3}{4}$ " CF type flanges welded around the chamber. Each CF flanged half-nipel was placed on a cross sectional circle which separates the chamber into two, through the total height. They were all employed for a variety of connection purposes with the vacuum chamber without breaking the seal, *e.g.* for power or pressure measurement connections. The unit had two evaporation sources, which could be controlled independently. There were also two shutters which were operating under an applied magnetic field.

Evaporation system was equipped with a turbo-molecular pump set. This set has a turbo pump with 140 l/s pumping speed and supported by a 3.6 l/s dry mechanical pump. Pumping unit was integrated from the bottom of the chamber in vertical direction. Connection of the turbo molecular part to mechanical pump was made by a stainless steel bellow. This bellow had 25-QF flanges at both ends.

4.2.1.1 Substrate Holder

A stainless steel disk with a diameter of 180 mm and 3 mm thickness was used as a substrate holder. The disk was drilled following a circular pattern of holes. Each hole was 24 mm in diameter. Glass substrates were placed on these holes during deposition. There were also four guides (stainless steel rods) placed into the chamber. These guides are served to adjust the distance between the source and substrates. The direction of the motion was vertical. For all deposition experiments distance was set to 20 cm.

4.2.1.2 Power Sources

Two low voltage high current power supplies were used to provide Joule-heating of the evaporation sources. Supplies were both voltage output controlled and each evaporation source was connected to the positive (+) output of the power supply through an electrical feedthrough. Each supply could provide 200 A at a maximum of 6 V.

4.2.2 Deposition Conditions

All films in this study were produced under a base pressure of 2×10^{-6} mbar. Source to substrate distance was typically 200 mm. Substrates were microscope slide glass, 0.17 mm thick, with 24 mm diameter. Substrates were cleaned ultrasonically in an alkali detergent, de-ionized water, acetone and ethanol sequentially prior to deposition. The deposition rate was typically 3 \AA s^{-1} . Materials for evaporation were Mg (granules, 99.98 % pure, -4 mesh), Cu (chip, 500 μm thick), Au-36.23 wt. % Pd (chip, 200 μm thick) and Pd (pellet, 99.95 % pure, 3 mm diameter). Films produced were Mg based; namely pure Mg, Mg capped with Au-Pd and Pd, Mg-Cu in both co-deposited and multilayered forms.

4.2.3 Hydrogen Storage

Hydrogenation experiments were carried out in a constant volume, *i.e.* Sievert's type apparatus described in detail elsewhere, (Baybörü 2001). The reactor used had a volume of 94 cc heated with a vertical tube furnace capable of reaching 723 K.

During hydrogenation, hydrogen pressure (max. 10 bar), and temperature was kept constant in the reactor. Where necessary, the reactor was evacuated to 10^{-4} mbar by employing a 50 l/s capacity turbo-molecular pump system.

The structural characterization of the as-deposited and hydrogen exposed thin films were performed by conventional X-ray Diffraction (XRD), in Bragg-Brentano (θ - 2θ) geometry at 40 kV and 40mA, using Cu K α radiation. The morphology of the films was studied by scanning electron microscope and field emission scanning electron microscope (SEM and FESEM) for hydrogenated and dehydrogenated states.

4.3 RESULTS AND DISCUSSION

Thicknesses of thin films as measured by cross-sectional SEM images are given in Table 4.1. As seen the thickness values ranges between 0.4 μm - 1.5 μm . Films as viewed from the surface had micron-size grain structure. Grains followed a typical hexagonal plate shape or distorted HCP bulk growth where the basal plane parallel to the substrate surface. This is a typical morphology of vacuum deposited Mg (Schiller *et al.* 2004).

Table 4.2 Thickness values of films measured via scanning electron microscope.

<u>Thin Film</u>	<u>Thickness (μm)</u>
Pure Mg	0.42
Mg/Pd	1.4
Pd/Mg/Pd	1.4
Mg/Au-Pd	1.4
Mg-Cu co-deposited	0.57
Cu/Mg/Cu/Mg multilayered	1.5

Fig. 4.2 shows plane surface images of thin films grown under different conditions. A typical example for pure Mg thin film is given in Fig. 4.2 (a). Surface images of Pd and Au-Pd coated Mg and Mg-Cu multilayered thin films are given in Fig. 4.2.

(b), (c) and (d), respectively. Figure illustrates the variation of size and shape differences of the plates, belongs to different films. This variation is due to the thickness difference of the films and the surface coating. The surface morphology is also affected from the chemical make-up and roughness of the underlying layers, such as shown in Fig. 4.2 (d), for Mg-Cu multilayered system.

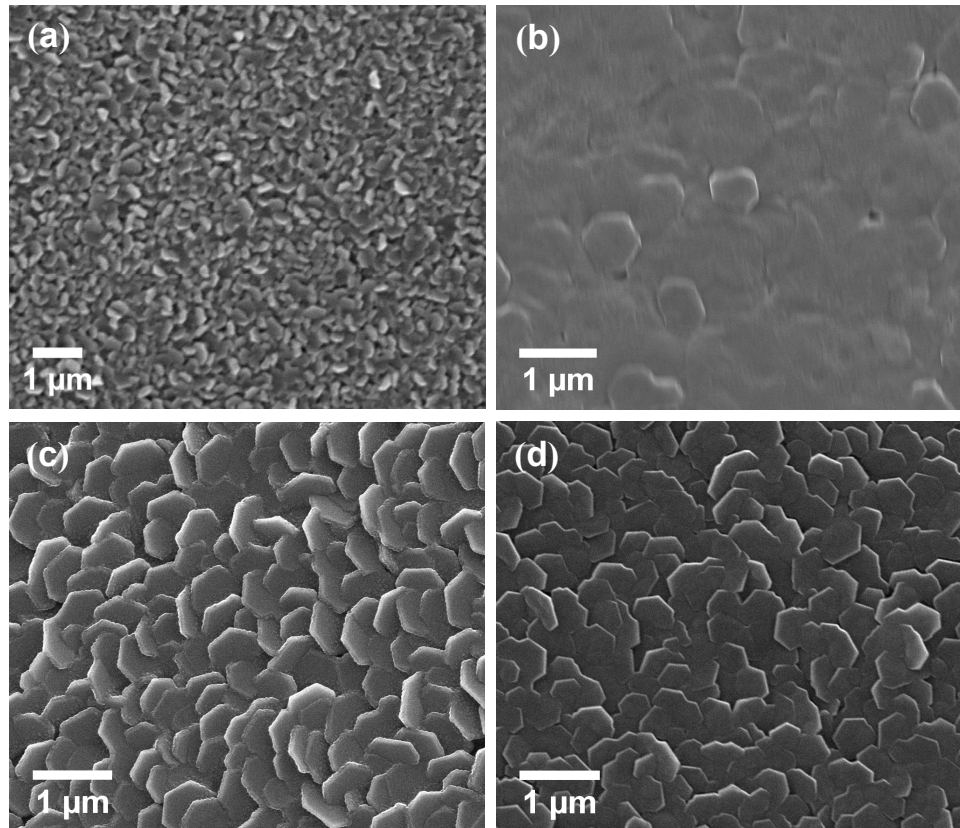


Figure 4.2 SEM images of a) pure Mg, and FE-SEM images of b) Pd/Mg/Pd, c) Mg/Au-Pd, d) Cu/Mg/Cu/Mg multilayered films in as-deposited states.

The through thickness fracture surface images of the films are given in Fig. 4.3. Films have a columnar structure. This structure can be observed easily in Fig. 4.3 (c) and (d). These films were 1400 and 1500 nm thick, respectively. The size and the

shape of the columns shows differences. As it is clear from the figure, this change is related to film thickness and thus the deposition time.

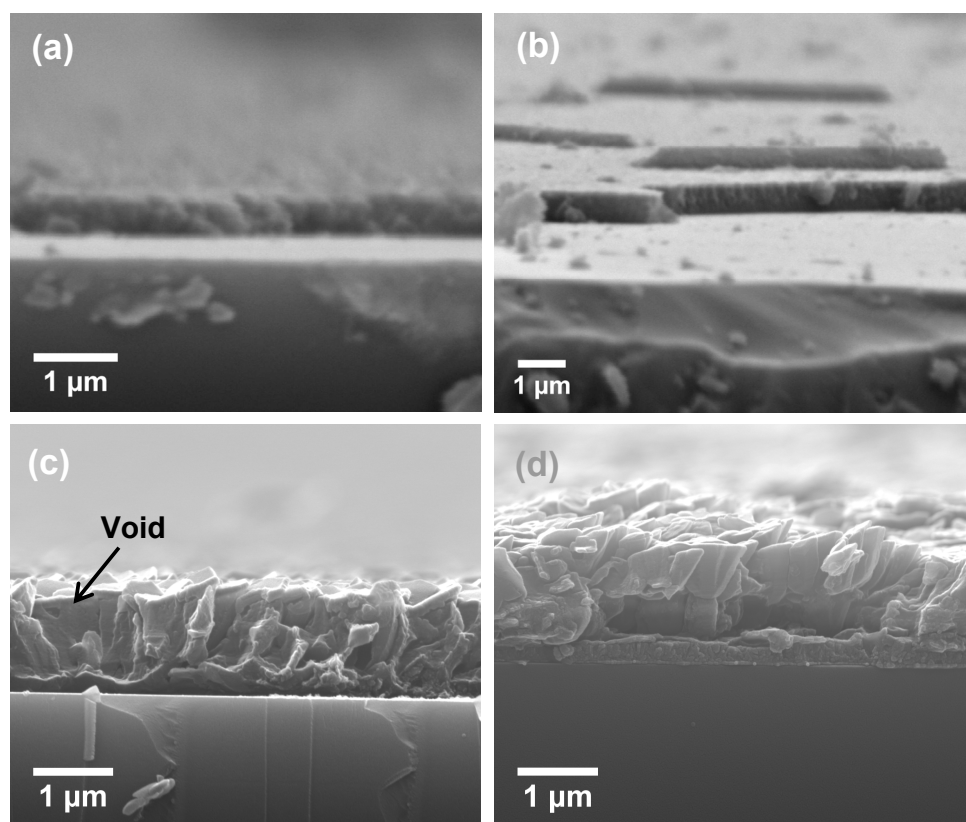


Figure 4.3 SEM images of a) pure Mg, b) Mg-Cu co-deposited, and FE-SEM images of c) Mg/Au-Pd, d) Cu/Mg/Cu/Mg multilayered films along the through thickness fracture surface.

According to Thornton 1977 the increase in diameter of the columns is directly proportional to the film thickness and may be due to longer exposure to elevated temperatures because of the radiation during deposition. This type of morphology formation was also reported by Srolovitz *et al.* 1988. According to their study the formation of the columns is the competition between discrete atomic deposition and higher amount of surface diffusion, because of the temperature increase during deposition.

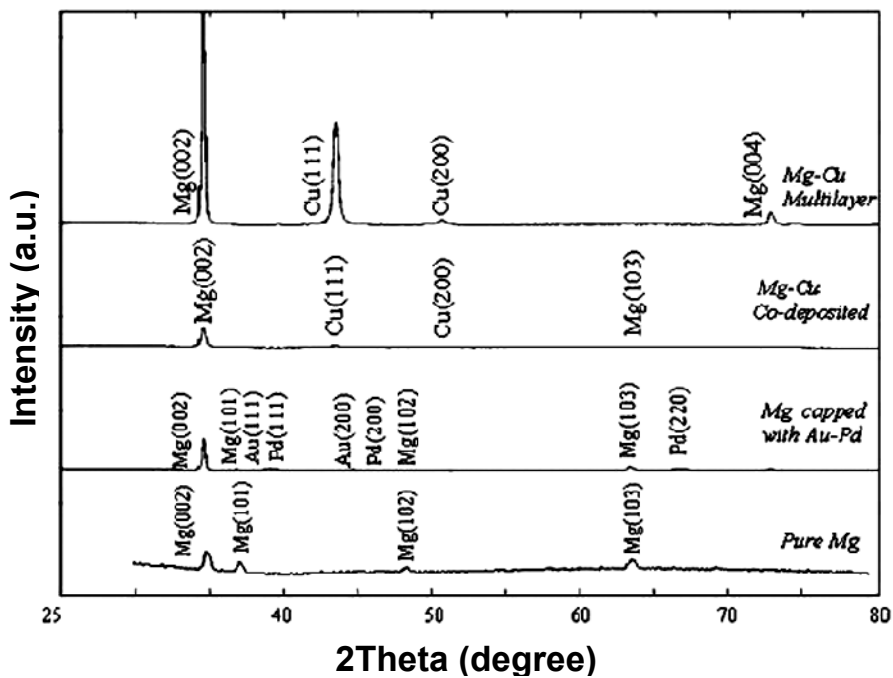


Figure 4.4 XRD patterns of Mg-based thin films in as-deposited state.

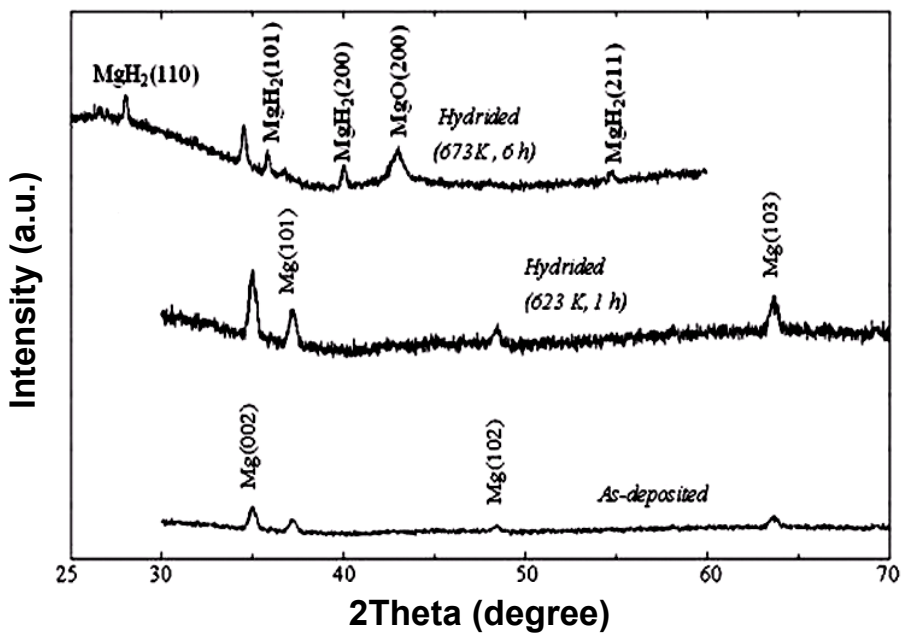


Figure 4.5 XRD patterns of pure Mg thin films after different processing steps, where indicated films were exposed to hydrogen atmosphere under 10 bar.

The structure observed here corresponds to zone II structure, with highly oriented granular epitaxy (Grovenor *et al.* 1984). Columns are separated by nano-size voids size voids and there are also some extra voids in the interior of the column itself. Such a formation is shown in Fig. 4.3 (c). When allowed the size of the columns may exceed values comparable to that of the film thickness. This is well illustrated in Fig. 4.3 (d) for Mg-columns in Mg-Cu multilayered thin film. On the other hand, co-evaporated Mg-Cu sample has a more equiaxed morphology as seen in Fig. 4.3 (b). This may be due to the pinning effect of different sized atoms during the film formation.

XRD data of as-deposited films implied differences in preferred orientation, as shown in Fig. 4.4. Mg-Cu multilayered system had strong preferred orientation, growth occurring mainly along the *c*-axis, facets being parallel to substrate surface. This observation also confirms the columnar structure seen in Fig. 4.3 (d). In this respect, pure Mg has the least preferred orientation.

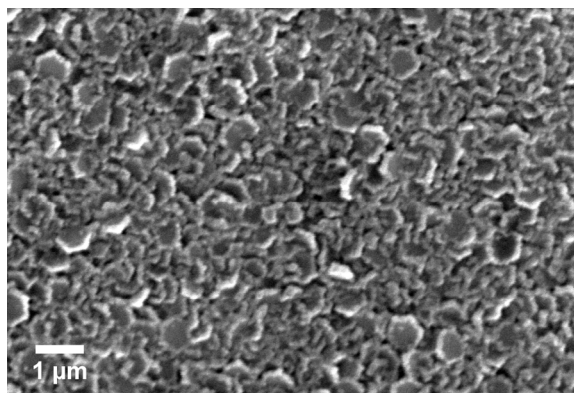


Figure 4.6 SEM image of pure Mg film after hydrogenation at 673 K, (10 bar hydrogen atmosphere for 6 h).

Hydrogenation experiments for pure Mg were carried out at 623 K and 673 K under 10 bar hydrogen pressure. There was no sign of hydrogen absorption at 623 K. Hydrogenation at 673 K (1 h) led to the formation of a small amount of MgH₂.

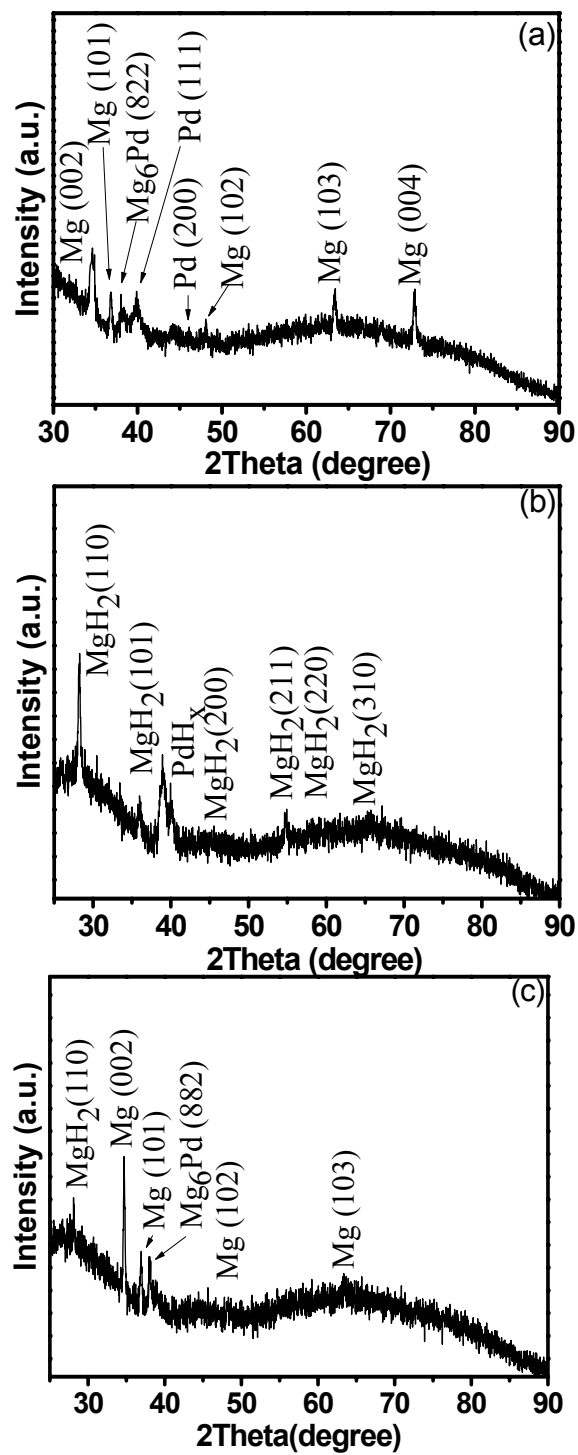


Figure 4.7 XRD patterns of Mg/Pd thin films a) as-deposited, b) hydrogenated at 423 K under 10 bar hydrogen, c) dehydrogenated at 473 K under 0.1 mbar residual gas pressure.

In an effort to completely hydrogenate the sample, the exposure time was increased to 6 hours. The amount of MgH₂ increased as expected but some portion of the film still remained as Mg, see Fig. 4.5. MgO was also present, which is probably due to oxygen pick up from glass substrate. A considerable grain growth occurred in the film by exposing the sample to a relatively high temperature (*e.g.* 673 K), Fig. 4.6. The difference may be well understood if this image is compared to Fig. 4.2 (a).

Pure Mg films were also deposited with a Pd overlayer coating. XRD data of these films are given in Fig.4.7. The strong preferred orientation along the *c*-axis is not observed for these samples, Fig.4.7 (a).

Diffractogramme imply the formation of Mg₆Pd intermetallic phase, probably during deposition. The formation of this phase is not desired due to its poor hydrogenation properties. According to Takeichi *et al.* 2007 Mg₆Pd phase can only absorb hydrogen after an activation process followed by a dissociation reaction under 20 bar hydrogen at 573 K.

Mg/Pd films were fully hydrogenated in one hour at 423 K, as shown in Fig 4.7 (b). All Mg peaks disappeared from the pattern after hydrogenation. Pattern comprises only MgH₂ peaks and (110) orientation has the highest intensity. It is not clear due to peak overlapping, whether the amount of Mg₆Pd was increased or a dissociation reaction was occurred, after hydrogenation. Fig 4.7 (c) shows the XRD pattern of the sample after dehydrogenation. Data reveals the complete release of hydrogen. Dehydrogenation was carried out under 0.1 mbar hydrogen pressure and almost all hydrogen desorbed from the sample at 473 K. The intensity of Mg₆Pd phase seems to be increased after dehydrogenation, probably because of relatively elevated temperature used for desorption. Pattern of dehydrogenated sample reveals Mg peaks as in the same orientation before hydrogenation. This may be accepted as a sign of reversible hydrogen storage in these samples.

In a similar approach, Pd layer was deposited from both side of the film to form a Pd/Mg/Pd sandwich multilayer. XRD data belongs to as-deposited, hydrogenated,

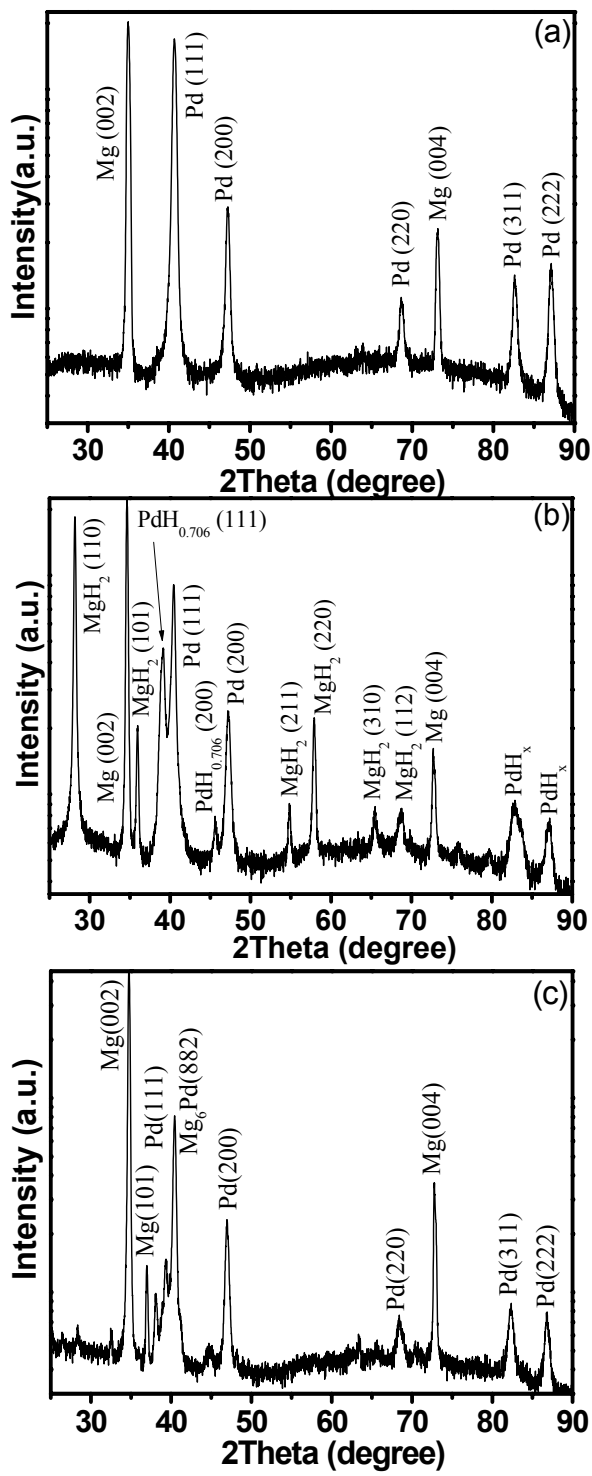


Figure 4.8 XRD patterns of Pd/Mg/Pd thin films a) as deposited, b) hydrogenated at 473 K, under 10 bar hydrogen, c) dehydrogenated at 473 K, under 0.1 mbar residual gas pressure.

and dehydrogenated state of this film is given in Fig. 4.8 (a-c). Films were hydrogenated under 10 bar of hydrogen at 473 K. Dehydrogenation was also performed at the same temperature.

In as-deposited state, Mg (002) and Pd (111) peaks showed the highest intensity. Pattern belonging to hydrogenated state has MgH₂ and Pd-H peaks together with the peak of unreacted Mg. Partial transformation to MgH₂ is probably due to kinetic limitations. Similar observations was also reported in literature and attributed to the formation of a hydride layer at the Mg-Pd interface which prevents further hydrogen diffusion through the interior of the film (Ostenfeld *et al.* 2007, Singh *et al.* 2007).

After dehydrogenation there are no more MgH₂ peaks exists on the pattern, implying the complete desorption of hydrogen, as shown in Fig. 4.8 (c). However, the formation of Mg₆Pd intermetallic phase is also observed for this sample, similar to Pd-capped Mg films.

XRD patterns belong to hydrogenated state of both Mg/Pd and Pd/Mg/Pd systems indicate formation of a Pd-H_x phase. It is well known that, Pd can absorb and desorb hydrogen reversibly at room temperature, (Frieske and Wicke 1973). Observation of the Pd-H_x phase in the current study may be due to fully hydrogenation of Pd layer, as reported by Higuchi *et al.* 2002. It is worth to point out that hydrogen solubility in the Pd layer, in case of thin films can be different than the hydrogen solubility in bulk Pd ($H/Pd \sim 0.67$). This was attributed to the lattice anisotropic strain of the Pd film, inducing a broadening of the interstitial site energy distribution, (Paillier and Roue 2005). According to Pundt 2004, restriction of the volume expansion due to the substrate as well as the presence of grain boundaries in large proportion may have also an incidence on the hydrogen solubility of Pd. This is the reason why some peaks were labelled as PdH_x in Fig. 4.7 and 4.8.

Mg film capped with Au-Pd was hydrogenated at 473 K. The results were more successful when compared to pure Mg films. After exposure to hydrogen for 1 hour, a considerable amount of MgH₂ formed, though some fraction remained as Mg. Pd

transformed to $\text{PdH}_{0.706}$ and Au stays unreacted, as shown in, Fig. 4.9. When hydrogenation temperature was increased to 523 K, the chemistry was modified and a greater portion of the film transformed into Mg_3Au intermetallic. Hydrogen absorption; therefore, did not improve with increasing temperature. Keeping in mind that Mg/Pd thin film was completely hydrogenated at 423 K, there is no use in employing Au-Pd alloy as a catalyst for hydrogen sorption of Mg thin films.

Mg-Cu produced via co-deposition was made up of separate phases, *i.e.* Mg and Cu, see Fig. 4.10. Upon hydrogenation at 473 K, the phases reacted with each other yielding Mg_2Cu intermetallic. Due to this internal reaction, nearly all Cu peaks disappeared from the diffractogramme. MgH_2 formed at this temperature but only in small amount.

Diffractogramme of as-deposited Mg/Cu multilayered film confirms the highly oriented nature of Cu and Mg phases in this film. The growth direction of Mg was perpendicular to (002) and that of Cu was perpendicular to (111), Fig. 4.11.

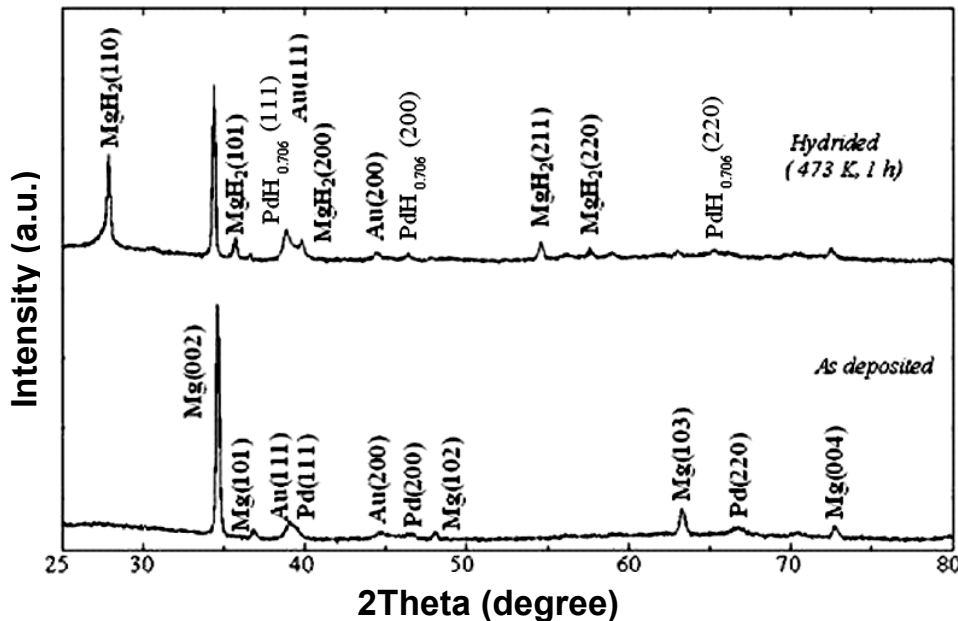


Figure 4.9 XRD patterns of Au-Pd capped Mg thin films in as-deposited and hydrogenated states, 10 bar.

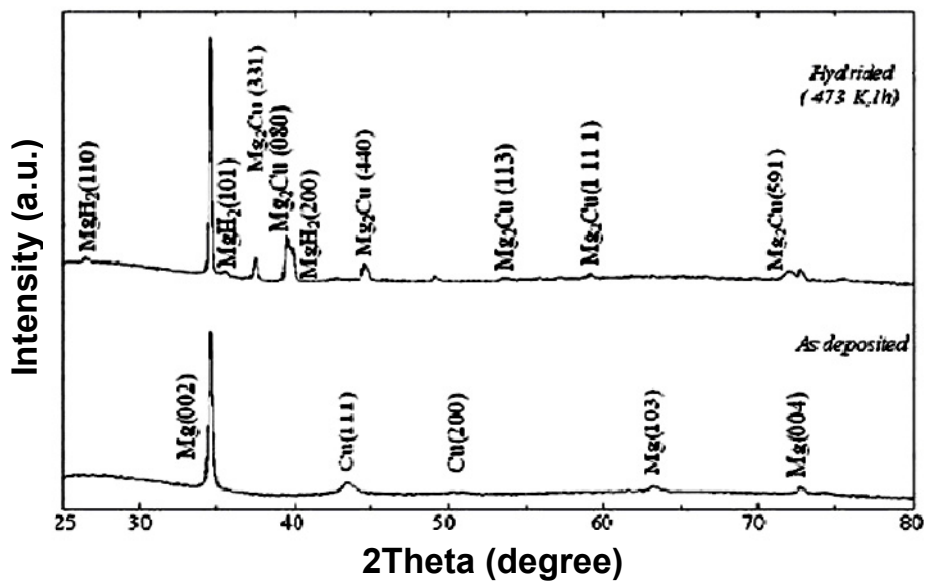


Figure 4.10 XRD patterns of Mg-Cu co-deposited thin films in as deposited and hydrogenated states, 10 bar.

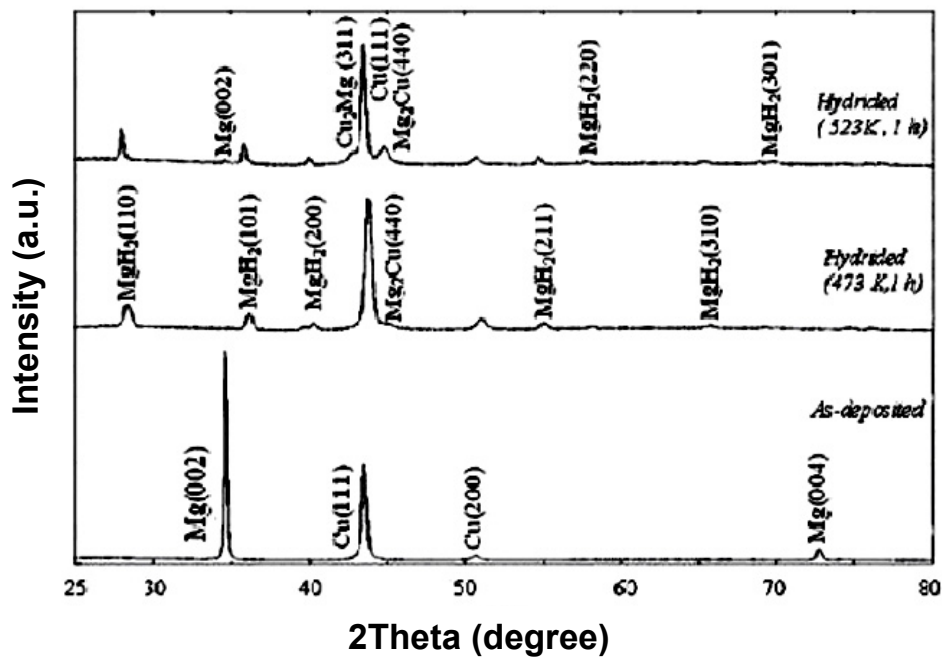


Figure 4.11 XRD patterns of Mg/Cu multilayered thin films in as-deposited and hydrogenated states, 10 bar.

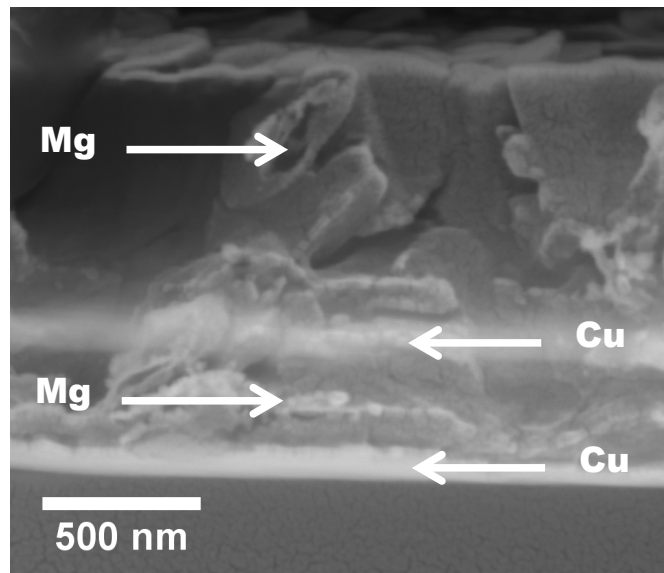


Figure 4.12 Back scattered FE-SEM image of a Mg/Cu multilayered thin film.

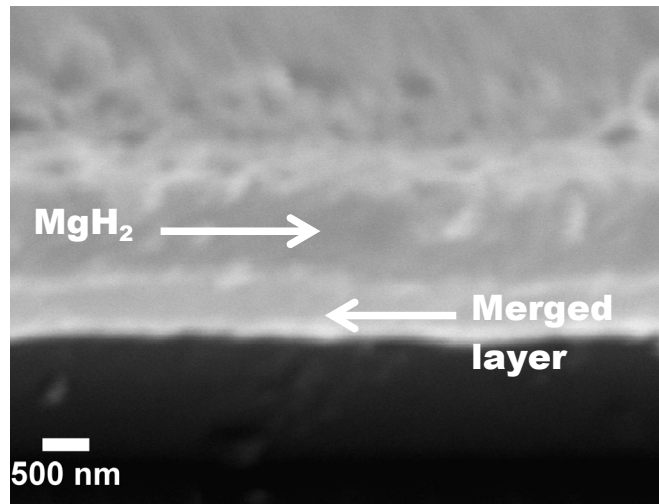


Figure 4.13 SEM image of a Mg/Cu multilayered thin film after hydrogenation at 473 K, 10 bar hydrogen.

Mg-Cu multilayer film was deposited in the form of four layers, *i.e.* Cu-Mg-Cu-Mg, starting from the glass substrate surface, Fig. 4.12. Upon exposure to hydrogen at

473 K, four layers in as-deposited state, transformed effectively into two-layer structure, Fig. 4.13. This probably occurred by merging of the first three layers into one and the upper -thicker-Mg layer remaining as the second layer. Result of hydrogenation at 473 K was quite successful in that nearly all Mg was transformed into MgH_2 , Fig. 4.11. There was a small amount of Mg_2Cu formed via internal reaction of the constituent elements.

According to Hong and d'Heurle 1992, Mg_2Cu was the first intermetallic to form in Mg-Cu multilayered systems independent from the atomic ratio of constituent elements. When hydrogenation temperature was increased to 523 K, there was a notable change in the chemical make-up. A considerable amount of MgH_2 was still present. Mg_2Cu was stronger in intensity and there was a presence of another intermetallic, namely Cu_2Mg . It has been proposed that the formation of Cu_2Mg is dependent on the existence of free Cu in the structure after the completion of the formation of Mg_2Cu , (Arcot *et al.* 1994). This yields that the formation of the secondary intermetallic may be due to further internal reactions because of the increase in hydrogenation temperature or it may be due to partial hydrogenation of Mg_2Cu phase. It has been known that Mg_2Cu phase absorbs hydrogen via disproportionation reaction, (Reilly and Wiswall 1967).



Considering all observations reported above, it is worth to emphasize that the current study aims at a methodology, whereby the chemistry of hydrogen storage materials could be adjusted freely, as this would be necessary to achieve hydrides less stable than that of pure MgH_2 . In this respect, the current results especially those concerning multi-component system imply that there is a narrow temperature interval for successful hydrogenation. At temperatures below this interval, the kinetics of sorption is slow, so films do not absorb hydrogen with acceptable rates. At temperatures above the interval, the internal reaction is dominant so the intermetallics dominate the structure. Unless intermetallics absorb hydrogen, there is

no use in employing high temperatures for hydrogenation. This has been the case for current systems.

For instance, when Mg capped with Au-Pd, hydrogenated at 523 K, the structure is dominated by Mg_3Au , which did not absorb hydrogen under current experimental conditions, *i.e.* under a pressure of 10 bar. Similarly, Mg-Cu, co-deposited or multilayered, when hydrogenated at 523 K formed Cu_2Mg with similar results. Thus, it appears that 473 K or a temperature in its vicinity is the upper limit for the working window for the current systems under consideration.

4.4 CONCLUSIONS

In this study, thin films of Mg, Mg capped with Au-Pd and only Pd, Mg-Cu co-deposited and Mg-Cu multilayer were produced via thermal evaporation with thicknesses ranging from 0.4 μm to 1.5 μm . Structural characterization and hydrogenation studies have shown that;

- 1- Under the deposition conditions employed, (10^{-6} mbar and $\geq RT$), all films are crystalline with columnar grains having some degree of preferred orientation.
- 2- No hydrogenation was observed at 623 K under 10 bar hydrogen pressure for pure Mg films. On the other hand, Pd-catalyst overlayer coated films could absorb and desorb hydrogen at 423 K and 473 K, respectively.
- 3- For multicomponent systems, the films are made-up of individual constituent elements in the as-deposited state, but upon hydrogenation at temperatures greater than 473 K, the constituent elements react with each other yielding the intermetallic phases such as Mg_3Au or Mg_2Cu .
- 4- Excluding the catalyst-capped films, of the systems studied in this work, Mg-Cu multilayer yielded the most favourable result in terms of useful storage system,

where Mg phase in the film can be totally converted into MgH₂ at temperatures not greater than 473 K.

Finally, the current study implies that if the as-deposited structure were to be used as hydrogen storage medium, useful temperature window exclude conditions that would bring about the formation of intermetallic phases. This aspect is important for the current crystalline thin films but perhaps more important for amorphous thin films, if crystallization is to be avoided. This case will be discussed in details, in Chapter 5.

CHAPTER 5

HYDROGEN STORAGE IN Mg-BASED AMORPHOUS/NANOCRYSTALLINE THIN FILMS

5.1 INTRODUCTION

Mg and Mg-based alloys are promising hydrogen storage materials due to their both high gravimetric and volumetric capacity (Sakintuna *et al.* 2007). However, the high stability of the hydride phase and poor sorption kinetics are obstacles that must be overcome before they can be seriously considered as a storage medium (Doppiu *et al.* 2005). Much effort has been put into finding possible processing routes that would destabilize MgH₂ and to improve its sorption kinetics. Mechanical milling has been usefully employed to improve the sorption kinetics (Andreasan *et al.* 2006), but the success in the destabilizing MgH₂ has been only partial (Recham *et al.* 2008).

Thin film processing is an alternative method of material synthesis that has recently found increasing use in hydrogen storage alloys. Mg (Leon *et al.* 2002), Mg-Nb (Bazzanella *et al.* 2004) and Mg-Ti (He *et al.* 2008) crystalline films as thick as 20-30 μm have been deposited, which have absorption and desorption characteristics that are very similar to those reported for bulk or powder-processed Mg-based alloys. Pranevicius *et al.* 2009 sputter deposited X-ray amorphous Mg-Ni films of 1.5 μm thickness, on quartz substrates, but have not reported data regarding its desorption characteristics.

Most thin film studies of relevance that are reported in literature are in the thickness range of 200-1000 nm (Vermeulen *et al.* 2006, Kumar *et al.* 2009, Baldi *et al.* 2009). Desorption temperature for this range are generally reported to be 373-473 K. For example, Higuchi *et al.* 2002 deposited 200 nm films of Mg on a glass substrate and observed a desorption temperature of 463 K. In this study, films of varying crystallinity were obtained by modifying the sputtering conditions, with the reported temperature referring to the film of lowest crystallinity.

Desorption temperatures are generally much lower for films of 15-100 nm thickness (Tang *et al.* 2009, Gremaud *et al.* 2005, Borsa *et al.* 2006, Bao *et al.* 2008). ¹Qu *et al.* 2009 sputter deposited 100 nm Mg films on Si and glass substrates, the films were X-ray amorphous and could desorb hydrogen in air at temperatures of 298 to 328 K. Similarly, Richardson *et al.* 2001 produced Mg-Ni films of 80 nm thickness on glass substrate, and examined their optical switching properties. The films with Mg:Ni= 10:1 to 3.5:1 were X-ray amorphous in the as-deposited state, but converted to a crystalline form when annealed at 398 K. The films could switch optically near ambient conditions. Yoshimura *et al.* 2006 in a similar study, deposited 40 nm films with Mg:Ni= 6.4 and 2, and reported that the films displayed similar absorption behaviors, while the kinetics of desorption improved with increasing Ni content. They reported that all compositions up to Mg₂Ni could desorb hydrogen at near ambient conditions. Mg-Ni-Ti films were examined by Gremaud *et al.* 2007 via sputter deposition. Using 3-inch sapphire substrates, they deposited 30-100 nm thick films with a composition gradient covering a greater portion of the ternary phase diagram. They reported a range of compositions near Mg₂Ni that could hydrogenate easily near ambient conditions.

In this work, following the previous chapter, we have investigated films of Mg-Cu system for the mid-thickness range, in both crystalline and amorphous forms. The study varies the Cu content as well as the substrate temperature so as to deposit films in different structures and compositions. But first, it would be useful to give details of the UHV system constructed for this purpose.

5.2 MATERIALS AND METHOD

5.2.1 Ultra High Vacuum Deposition System

This unit comprises of three main parts; vacuum chamber/base plate, pumping system and the bell jar, which were all modified from the system discussed in Chapter 4. Modification was done by replacing all relevant parts with their stainless steel counterparts to obtain ultra high vacuum levels. The number of feedthroughs were doubled and these 12 feedthroughs were placed on the chamber similar to previous design, Fig. 5.1.

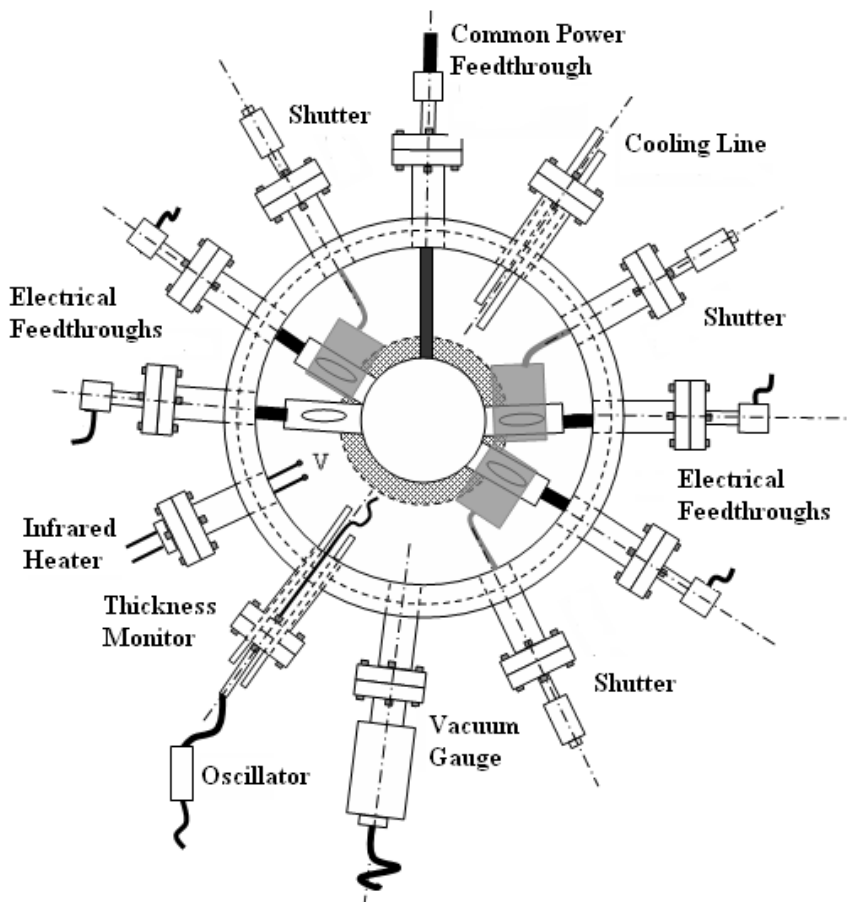


Figure 5.1 Schematic drawing of the vacuum chamber and feedthroughs as seen from z-axis, (dimensions of the system are given in Fig. 5.2).

Machined and polished surface of the chamber now replaced with a 14.5/8" wire seal flange to utilize a 3 mm diameter copper o-ring instead of an L-ring discussed before. The mating flange for the wire sealing flange is now on a stainless steel bell jar. As the bolts of a flange-pair are tightened, the flange design constrains the Cu-wire flow to form a seal between two faces. The base of the chamber was left as it was and utilized as a connection port to the pumping system as given in details before, Fig. 5.2.

5.2.1.1 Bell Jar

Bell jar was constructed in 278 mm inner diameter to assure well matching with the vacuum chamber, via wire seal male/female flanges, and 350 mm in height as shown in Fig. 5.2. For this purpose, a 5 mm thick stainless steel sheet was bended in a complete cylindrical shape and welded through the vertical axis. Upper lid was bulged to give a dome shape and again welded to the top of the cylindrical body. There is a viewport on the bell jar, which was welded at a height of 150 mm from the bottom. This viewport is actually an 8" CF flange with an extended welding pipe at one side and a window on the other side. There is also a shutter on the vacuum side, which has 70° of free motion along the vertical axis via a rotational feedthrough. The window allows monitoring the evaporation stage and the shutter basically protects the viewing port from contamination due to vapor stream inside.

5.2.1.2 Vacuum Pumps

Deposition system constructed in this study has a volume of approximately 40 l. Achievement of high vacuum levels depends on the design as well as the materials used, and also the characteristics of pumping set where the equipment has to provide a sufficient pumping speed. For this purpose, a turbomolecular pump was backed by a mechanical pump. The mechanical pump is a dry type, with a ~ 3.6 l/s pumping speed. A vacuum level of 5×10^{-2} mbar is possible with this pump.

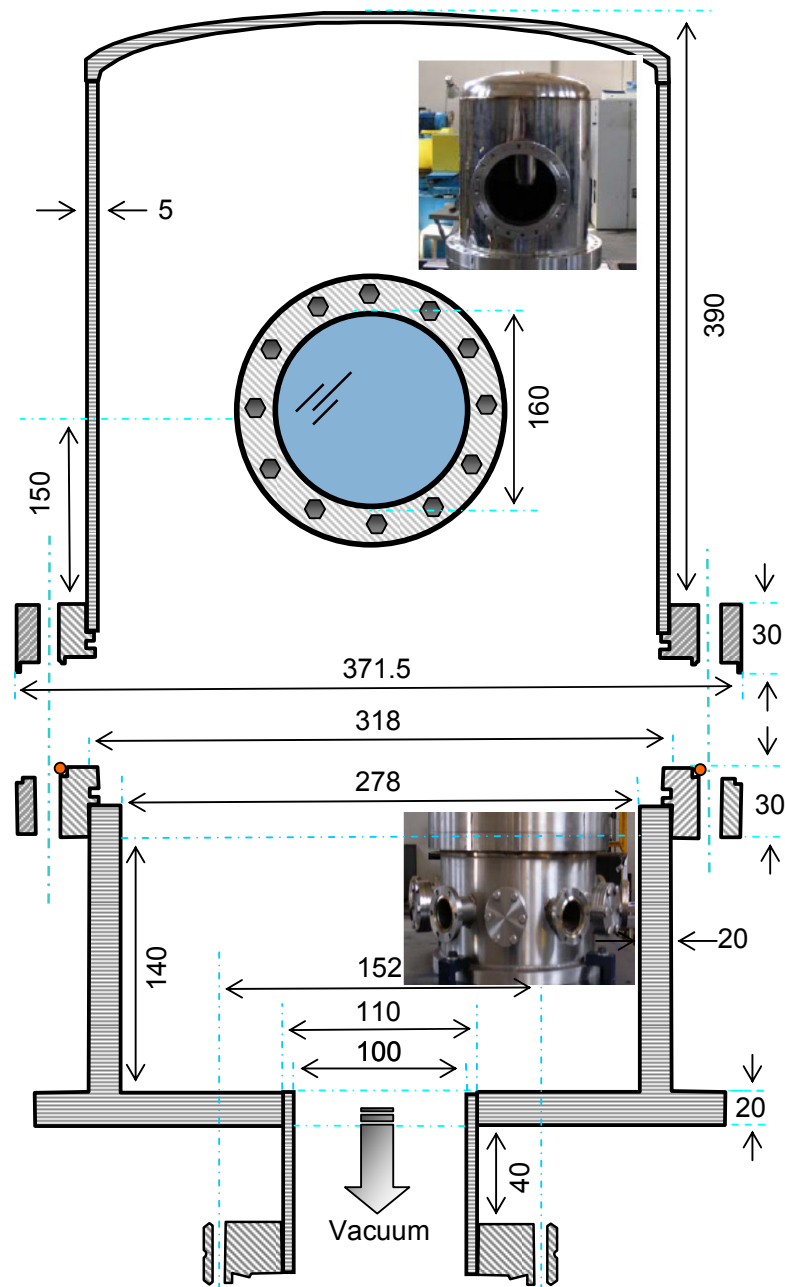


Figure 5.2 Schematic drawing of stainless steel bell jar and the chamber (all dimensions are given in mm).

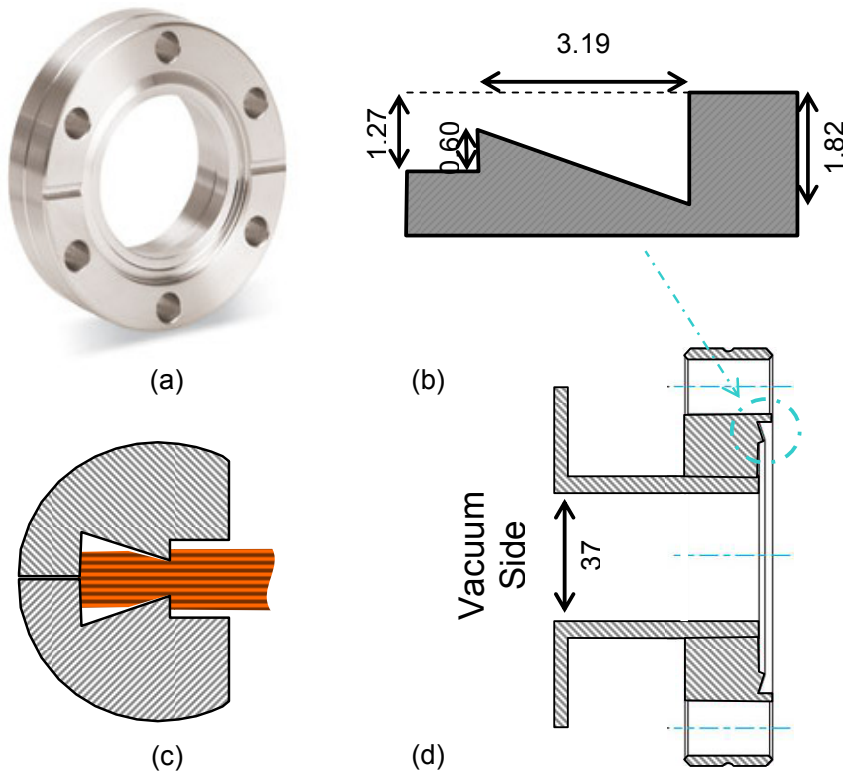


Figure 5.3: 2 $\frac{3}{4}$ " CF flange. Image on the left top shows the flange itself, whereas other drawings represent dimensions of the gasket and deforming region. For a leak-tight system, a copper gasket was used for flange connections with 48 mm diameter and 2 mm thick. Sealing was provided by tightening the flanges with six bolt and nut set, where the gasket deformed from 2 mm to 1.34 mm. (all dimensions given here are in mm).

The ultimate vacuum level of the turbo part is 5×10^{-10} mbar and it has a pumping speed of 140 l/s. Both of the pumps were cooled with air ventilation. This pump set is connected via a 6" CF flange to the vacuum chamber. On the other hand, a 25-QF flange ended bellow supplies the connection between the mechanical and turbo pump.

The type of the flange has a significant impact on the final vacuum level of the system. It is not possible to obtain ultra high vacuum levels by using QF or ISO

flanges, which are proper for elastomeric o-ring assembly. Therefore, all connections in this apparatus were chosen as CF type, which uses Cu gaskets (oxygen free high conductivity) for sealing. As mentioned before there are 12 feedthroughs around the base plate and all these were preferred as 2 $\frac{3}{4}$ " CF type flange.

The connection between the chamber and the bell jar is also possible by a CF type regular flange, but due to large gasket diameters, it is not economical. Thus, a wire seal type flange was preferred for this connection which uses a 3 mm diameter Cu wire for sealing. Details of this flange are given in Fig. 5.4.

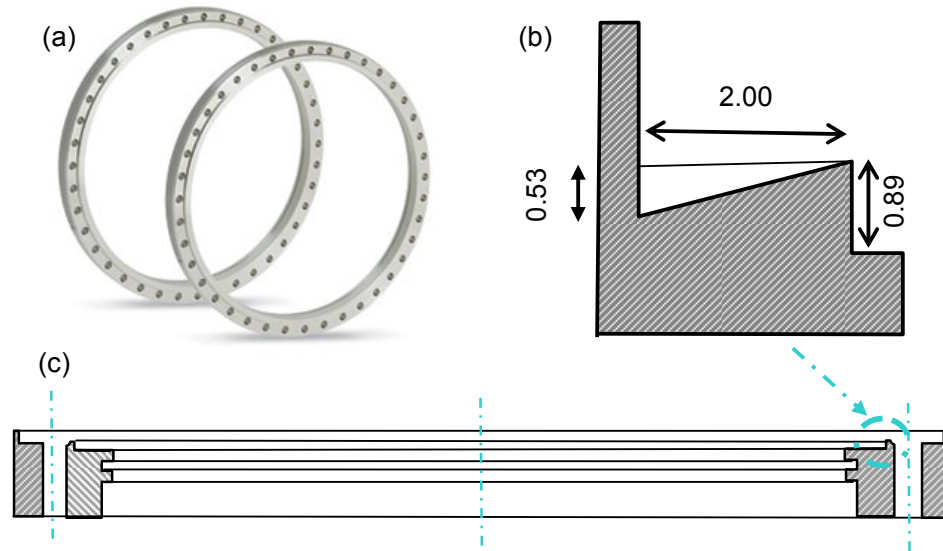


Figure 5.4 14 5/8" male wire seal flange. Image at the top left shows the flange itself, whereas other drawings represent the wire-deforming region and the schematic drawing of the flange. Sealing was provided by placing a 3 mm diameter Cu wire to 0.53 mm deep-2 mm wide conical region on the flange. Male and female flanges were tightened by 32 bolt and nut set to deform the wire from 3 mm to 1.06 mm (all dimensions given here are in mm)

As given in Fig. 5.1., the unit has 12 feedthroughs welded around the vacuum chamber. Five of those are used for power supply connections. One of them is

common for all sources, Fig. 5.5. This provides the production of thin films by sequential deposition or co-deposition methods.

It is possible to contaminate any source during operation due to vapor emitted from any other operating source especially during co-deposition. Thus, three of those feedthroughs were used for rotational shutters, placed just near the evaporation source feedthroughs. The position of the shutters inside the chamber can be adjusted manually and can be fixed at any position by locking the rotational feedthrough knob from outside. One of the feedthrough was used for providing power to quartz infrared lamp inside the chamber. This heater lamp was used for bake-out process. Another feedthrough was employed to provide cooling fluid entrance and exit from the system continuously.

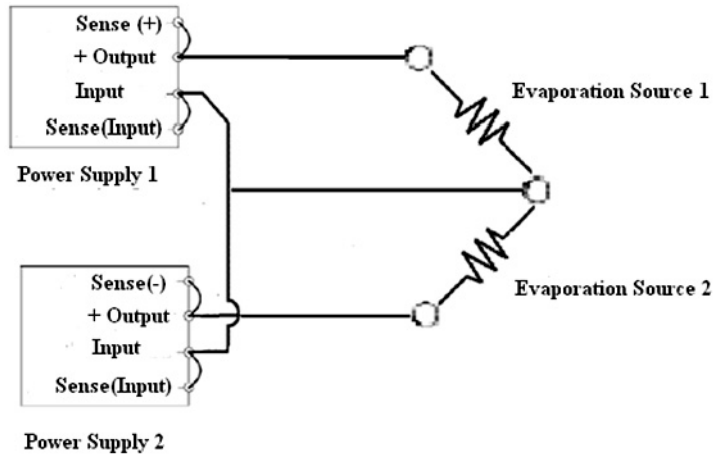


Figure 5.5 Power supply connection and control in thermal evaporation system. Input sense is common for all supplies, and positive output connections were made separately for each supply. Figure schematically shows the connections only for two power supplies.

A hot cathode ionization/quartz crystal friction type vacuum gauge with a CF flange connection was assembled to one of the feedthroughs. This gauge can measure the vacuum level in a range from 1000 to 4×10^{-10} mbar, with an accuracy of 15 % and

repeatability of 5 % of reading. A multi-channel controller was used to monitor and control the vacuum gauge. Finally, the last feedthrough was employed for the connection of the thickness monitor sensor and its cooling water entrance-exit to/from the system.

5.2.2 Substrate Cooling System and Operation

During resistive evaporation radiation evolves from the sources during operation. This radiation may rise the temperature of the depositing film to undesirable levels. Therefore, controlling the temperature of the substrates during deposition is essential for the final structure of the films.

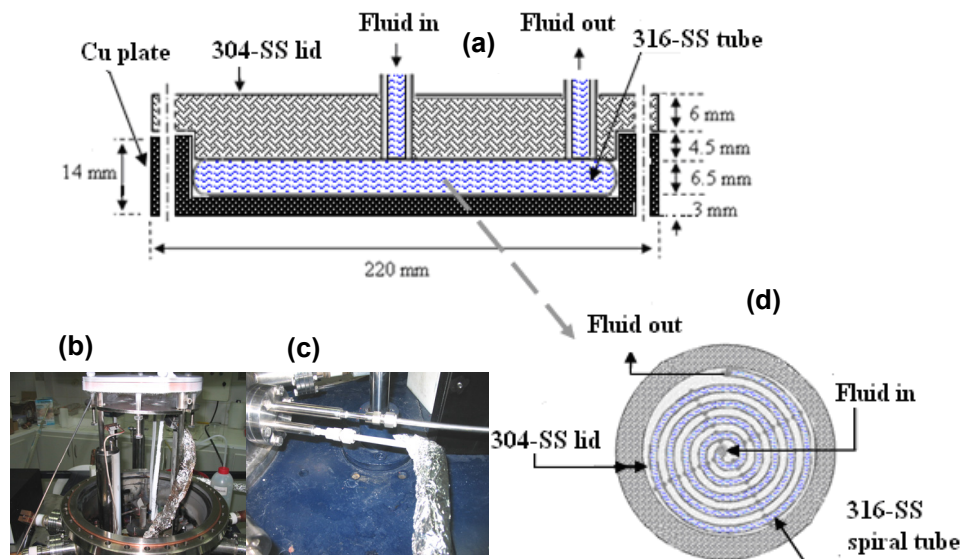


Figure 5.6 Substrate cooling system, a) dimensions of the cooling platform, b) interior cooling system, c) fluid entrance and exit to/from deposition system, d) schematic representation of welded part of the tube on SS lid.

Fig. 5.6 gives the detail of substrate cooling system. Cooling fluid enters the system from a CF flange, as mentioned above. Two stainless steel tubes with 6.35 mm in

diameter and 1.5 mm in wall thickness were welded in a horizontal manner on this flange, Fig 5.6 (c). With the help of proper fittings, cooling fluid can flow inside of the system from one tube, complete its circulation in the cooling platform and leaves the system from the other tube on the flange.

Cooling platform is given schematically in Fig. 5.6 (a), and the parts of this system inside the chamber are given in Fig. 5.6. (b). Platform consists of two separate plates. One of these plates was constructed from 304-quality stainless steel and the other was high purity copper. A stainless steel tube of 6.5 m length was used as a fluid carrier inside the chamber. 5.5 m of this tube was deformed into a spiral shape *i.e.* 180 mm in diameter, Fig. 5.6 (d). This part of the tube fixed to stainless steel lid by welding from proper points in a horizontal manner. Copper plate was machined to form an 11 mm deep blank at one side for the purpose of spiral tube placing inside. Opposite side of the copper disk was machined carefully to eliminate the surface roughness aiming perfect matching with the substrate surfaces. Substrates are placed on a substrate holder, which was made of a 5 mm thick and 220 mm diameter stainless steel disk. This plate was drilled such that there are six 22 mm diameter holes found at every 60°, on an 80 mm diameter circle where the center of this circle and the plate coincide with each other. Glass substrates are placed on those holes, and setup allows the plate to move up and down on four stainless steel guide. Substrate holder can be fixed at any position on these guides by fastening the bolts on each guide. This option provides a good contact of substrate surfaces with the lower side of the cooling platform.

Low substrate temperature was obtained either by water circulation or cooled nitrogen gas flowing through the system. In case of water-cooling, system was attached to tap water directly and no other precaution was taken for further cooling. On the other hand, cooling of substrates with nitrogen gas required a special set-up. For this purpose, high purity nitrogen gas coming from a pressurized container was fed into a Cu pipe, which passes through a liquid nitrogen tank. This pipe was 4 mm in diameter and it has 1 mm wall thickness. A portion of this pipe deformed into a helix shape with 40 mm outer diameter and 230 mm in height, and then this helix

was immersed into a 30 l of liquid nitrogen tank during gas flow. In such an application, ultimate cooling level was found to depend highly on the rate and time of nitrogen gas flow. The temperature of the cooling platform was measured during deposition by a thermocouple, which is in contact with the Cu plate discussed above. For this purpose, a thermocouple feedthrough was replaced with one of the electrical feedthrough on the system. Thermocouple was a K-type and can provide measurement in the temperature range of 73-1523 K.

5.2.3 Ultra High Vacuum Levels

Thermal evaporation system discussed in Chapter 4 was a pyrex bell jar system and ultimate vacuum level was about 10^{-6} mbar. This level can be assumed as the transition between HV to UHV. Therefore, all components of this system were modified according to the requirements essential for UHV. Pyrex bell jar was replaced with a stainless steel bell jar and all connections were converted to CF type flanges as discussed in details above. Obtaining such vacuum levels requires a standard cleaning procedure and special precautions. Therefore, all components in the system first exposed to ultrasonic alkali detergent cleaning in deionised water at 60 °C temperature. Then they all rinsed with distilled water for a few times and additional ultrasonic deionised water treatment was applied at 60 °C to remove residues of alkali detergent contamination. After ultrasonic cleaning all parts were exposed to acetone and rinsed with high purity ethyl alcohol. This assures the removal of water, detergent and hydrocarbon leftovers from the surfaces. After the cleaning procedure, components were dried in hot air flow, (drying under flowing nitrogen is recommended).

Bake-out or degassing of the whole system is another special precaution. Bake-out was achieved simply by turning on a quartz infrared heater for this study. This lamp is suitable for vacuum applications and it is 30 mm in length and 12 mm in diameter. It can be loaded from 0 to 100 % to a total output of 6000 W. Quartz heater was placed vertically in the evaporation chamber and for this purpose a special flange

and lamp holder was designed and constructed, Fig. 5.7. A pyrex shield was also placed around the lamp to avoid the contamination from the vapor stream in the system during deposition. After the integration of all the components, vacuum system was subjected to preliminary experiments. These experiments were done by loading quartz heater as to maintain a temperature level of 200-225 °C in the system.

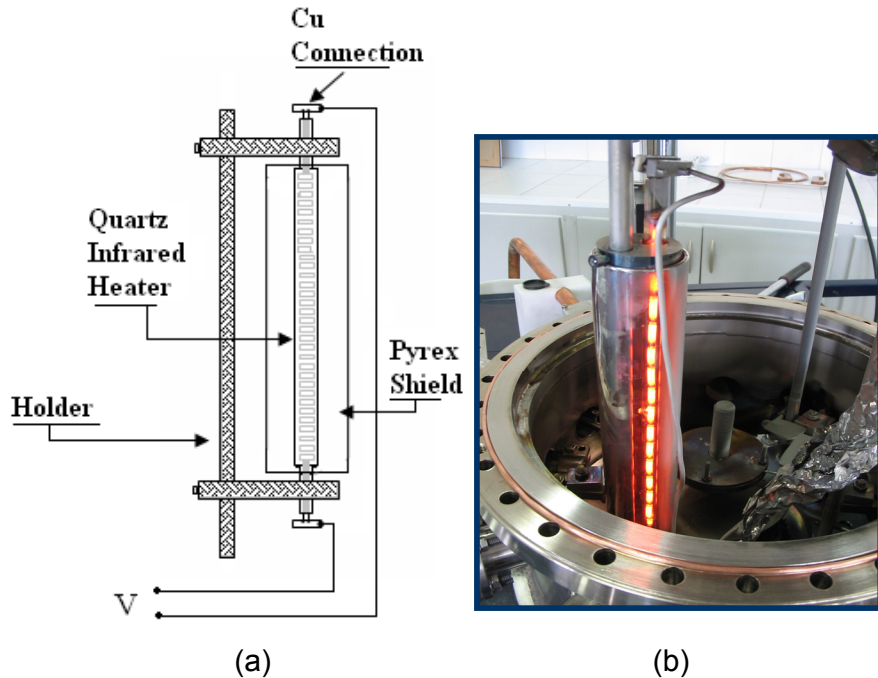


Figure 5.7 a) Schematic drawing of quartz infrared heater and lamp holder, and b) the lamp itself inside the chamber.

Fig. 5.8 shows the vacuum level before and after degassing of the system. Here, before bake-out process the vacuum level was 2.15×10^{-6} mbar after 12 hours of pumping, whereas it was possible to obtain 1×10^{-7} mbar vacuum after bake-out procedure within the same period. After 36 hours of pumping, vacuum levels were 1.17×10^{-6} mbar before bake-out and 6×10^{-8} mbar after bake-out. Experience with degassing showed that it is always possible to obtain 1×10^{-7} mbar within 16 h of continuous pump-down of the system even though significant contamination occurred for every deposition cycle.

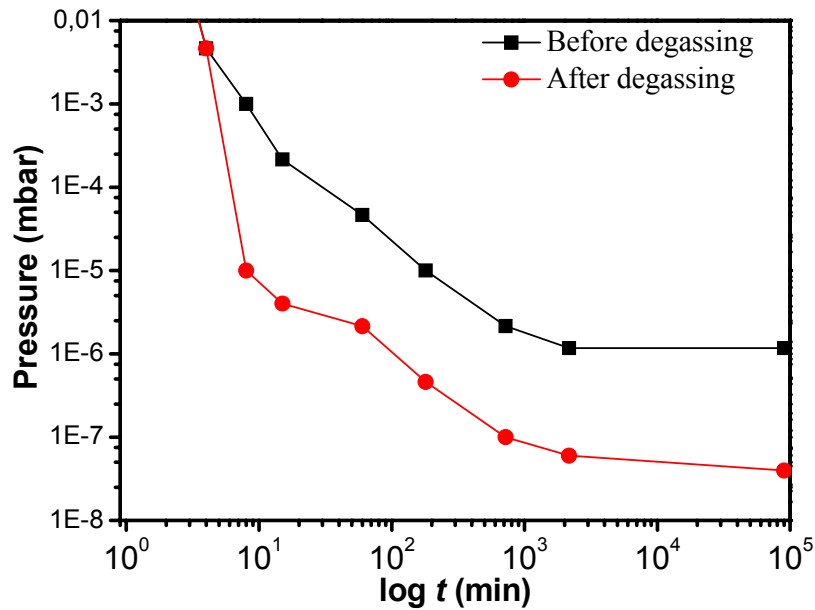


Figure 5.8 Measured vacuum level in the chamber as a function of pump down time before and after degassing operation.

5.2.4 Quartz Crystal Thickness Monitor

Thicknesses of the films were followed *in-situ* by a quartz crystal thickness monitor. The device composed of three main components, which are the control/display unit, a sensor positioned properly into vacuum and a flange, which provides the connection between the sensor, and the controller unit. A stainless steel cooling tube attached on the same flange to provide cooling of the sensor head with flowing water. Cooling of the sensor head is essential for maintaining the stability of the measurement.

The main controller has an interface for deposition programming and an ethernet connection option. It can measure and display deposition rate with 0.01 Å/s and 1.0 Å for thickness. 25 different film deposition programming can be possible up to 1000 steps in total. The controller is able to manage co-deposition of four materials at the same time. Thus, it controls all four power sources by a proper type of connections. This connection is given schematically only for one source in Fig. 5.9.

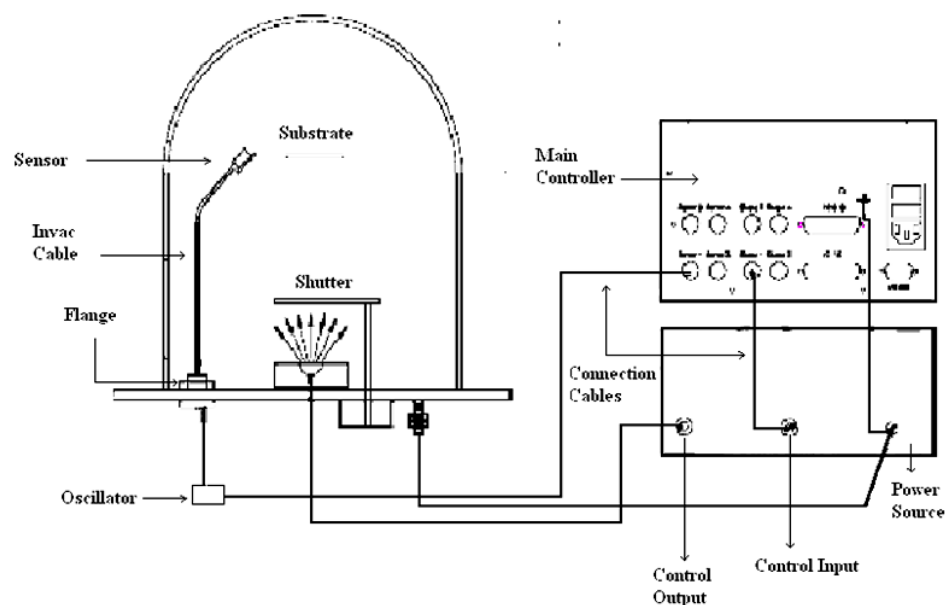


Figure 5.9 Connection of the thickness monitor to a power source and deposition system. Drawing shows the connection schematically only for one source. (Figure adapted from Sigma Instruments web-page)

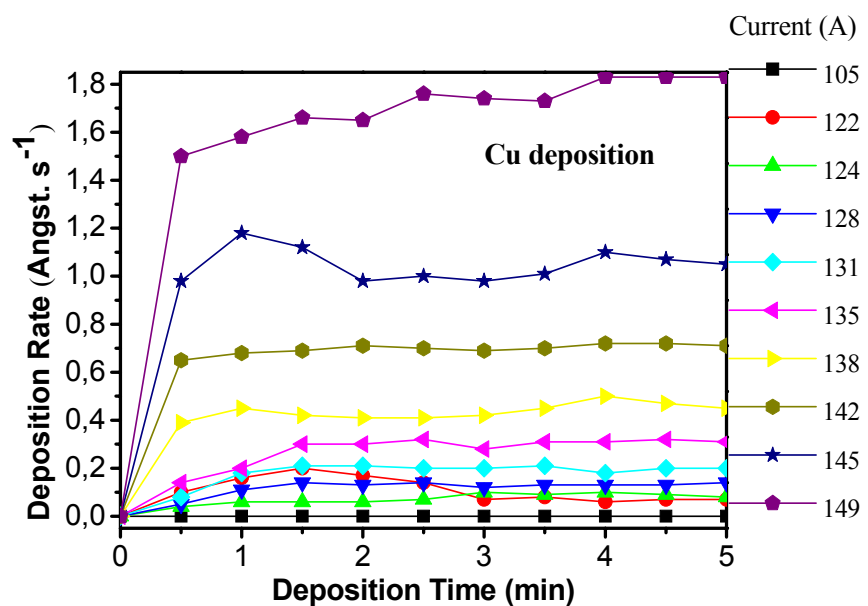


Figure 5.10 Change of deposition rate for 5.7 g Cu at 1×10^{-7} mbar as a function of applied current and time.

This operation requires 4 different sensors; however, the unit for the current study only has one, and so only single deposition rate can be followed during deposition. Due to single sensor available inside, preliminary deposition-rate experiments were carried out for Cu and Mg individually. The results are given for Cu in Fig. 5.10. Deposition rates were calibrated as a function of applied power and time, and obtained results were used during co-deposition of film samples.

5.2.5 Thin Film Production

5.2.5.1 Deposition Conditions

All films in this study were deposited under a base pressure of 1×10^{-7} mbar via co-deposition method. For this purpose Mg, Cu and Pd were evaporated from different sources. Materials for evaporation were Mg (granules, 99.98 % pure, -4 mesh), Cu (chip, 500 μm thick), and Pd (pellet, 99.95 % pure, 3 mm diameter). For controlled deposition 1 g Mg, 5.7 g Cu and 0.05 g Pd were used for each experiment. Source to substrate distance was typically 300 mm. Substrates were glass, 0.17 mm thick, with 24 mm diameter. They were cleaned ultrasonically in alkali detergent, DI water, acetone and ethanol subsequently before placing them to vacuum chamber. Prior to deposition substrate temperature was set to the necessary value and cooling process was continued during film formation.

Constant deposition rates were used both for Mg and Cu for the current study. Deposition rates of these elements were recorded depending on the applied power precisely by a set of preliminary experiments, Fig. 5.11 and 5.12.

The rate was set to 10 \AA/sec for Mg, and for Cu it was set to 0.43, 0.86 and 1.29 \AA/sec , to provide concentrations of 5, 10 and 15 at. % Cu in the final film composition. During the study, constant vacuum level and source material weight was used for each experiment to assure reproducible results. On the other hand, Pd

deposition was made by quick evaporation to avoid tungsten contamination from the source and 5-25 nm thick Pd was applied to all films as a catalyst cap-layer.

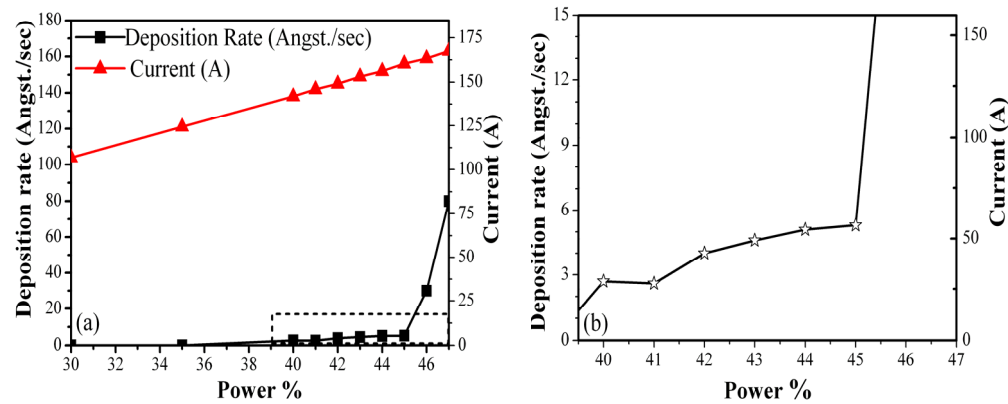


Figure 5.11: Deposition conditions for Mg, a) change of deposition rate as a function of applied power and current, b) details of marked region in (a).

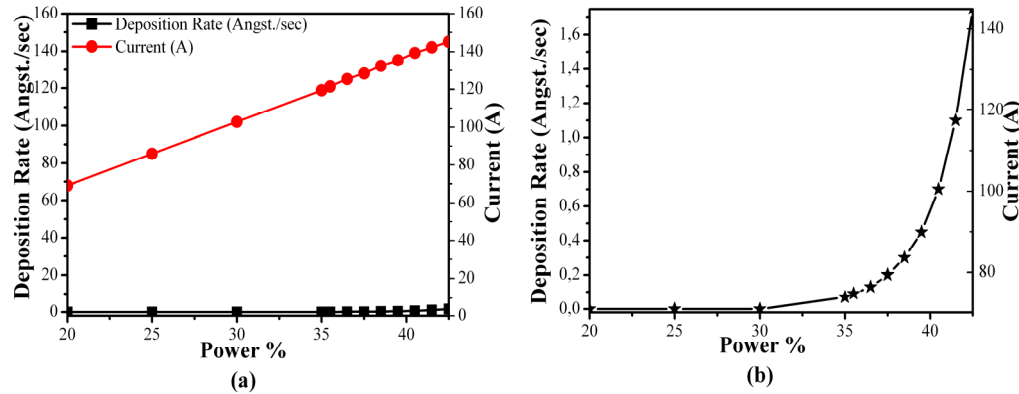


Figure 5.12 Deposition conditions for Cu, a) change of deposition rate as a function of applied power and current, b) details of change.

5.2.6 Hydrogenation and Characterization of Thin Films

Hydrogen storage properties of thin films were followed by resistance measurement method. For this aim, a resistance measurement set-up was constructed.

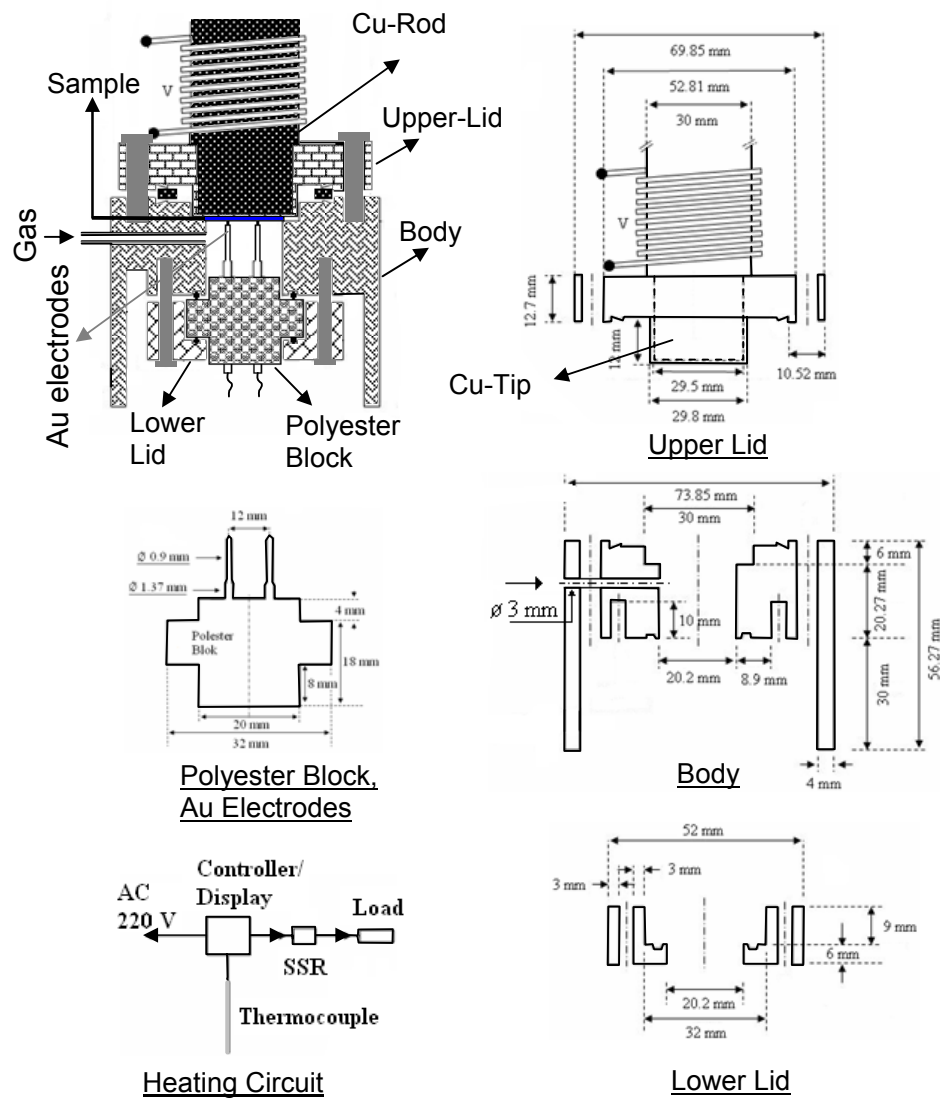


Figure 5.13 Resistance measurement set-up (Özgit 2009).

5.2.6.1 Resistance Measurement Set-up

Resistance or resistivity measurement method is generally applied in-situ for thin films, where 4-point probe process is commonly used (Hjort *et al.* 1996, Ingason and Olafsson 2005). In this study, 2-point probe method was applied, ignoring the arising ohmic contact resistance, which is a disadvantage of this method. Schematic view of the set-up is given in Fig. 5.13 and 5.14.

Set-up consists of four main components; which are measurement cell, heater, gas/vacuum line, and pressure measurement equipments. The measurement cell has three subcomponents; upper lid, main body and lower lid, Fig. 5.13. Upper lid was in contact with a Cu heater rod, and it is actually a CF type flange to provide a leak tight connection with the main body. There is a proper cavity on the upper part of the main body, and sample touches to electrodes when housed in this cavity. Electrodes have a spring system inside them and this mechanism helps to make the contact between the film and upper lid when the cell is closed.

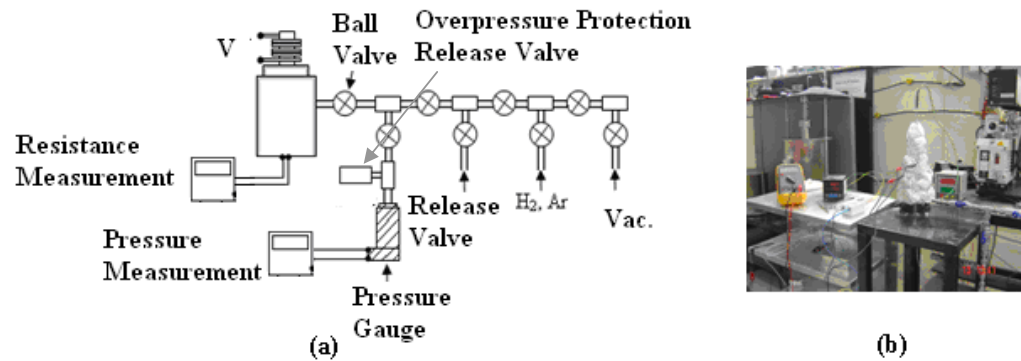


Figure 5.14 Resistance measurement set-up a) schematic drawing, b) general view of the set-up during experiment (Özgit 2009).

Electrodes were mounted properly in a polyester block in a vacuum tight manner. This polymeric block was fixed to the reactor from the lower side. An O-ring was placed in between to seal the system. Lower lid was fastened to complete the

measurement cell, while it is in contact with the bottom of the polyester block. There is also an O-ring in-between them and fastening was made by relatively long bolts to main body. Electrodes were Au coated and the distance between the centers of two electrodes was 12 mm. Measurement cell and gas line was assembled with proper vacuum tight fittings. Gas line allows hydrogen and argon loading, vacuum pumping and evacuation of the system, with the help of several ball valves placed at different locations on the line.

A maximum pressure of 10 bar, high purity hydrogen or argon can be exposed on the sample. There is also a pressure gauge, release valve and an overpressure protection release valve mounted on the gas line. This gauge is suitable for pressure measurements between 0-2000 mbar with a typical resolution of 1 mbar. Overpressure protection valve can be set in the range of 700-15500 mbar. General view of this set-up is given in Fig. 5.14. (b). Heating of the system is made by employing a spiral resistance placed on the copper rod at some distance. When the resistance is on, it heats up the Cu rod. This rod is in contact with the upper lid of the reactor and it is 30 mm in diameter and 220 mm in length. The heat is transferred by this Cu rod to a specific region of the upper lid, which is actually in contact with the film sample, under consideration. Temperature measurement was carried out by employing a K-type thermocouple and controlled by a PID controller. Schematic view of this heating circuit is given in Fig. 5.13.

5.2.6.2 Hydrogen Loading and Dehydrogenation

Hydrogenation of samples was carried out under constant pressure gas mixture atmosphere, *e.g.* 100 mbar H₂ + 1000 mbar Ar. Before gas loading, the system was evacuated at least half an hour down to a vacuum level of 10⁻¹ mbar. After gas loading, heating process was applied in two steps. Sample was heated with a 10 °C temperature intervals with a rate of 1 °C/min. After every 10 °C temperature increase a dwell time of 15 min applied and the resistance value was recorded after this duration. Once the required resistance value obtained, gas mixture was removed

from the system. For this purpose, the pressure inside the cell was set back to 0.1 mbar again. During dehydrogenation, heating of the sample and data recording was maintained as in the same way discussed above. Most of the time process was terminated with complete dehydrogenation. Where the partial desorption is the case, at most a temperature of 150 °C was applied in the system. Cooling was carried out under vacuum. Then the samples were characterized by XRD and SEM.

Table 5.1 XRD measurement conditions used during the study.

	Thin Film (θ-2θ)	Thin Film (2θ)
B (rpm)	10	10
DS (mm)	Variable	0.1
DHLS (mm)	10	5
IA (°)	-	0.5
SW (°)	0.02	0.02
SS (°/min)	1	1
RS (mm)	0.3	0.3

B: sample rotating speed, **DS:** divergence slit, **DHLS:** divergence height limiting slit, **IA:** incidence angle, **SW:** sampling width, **SS:** scanning speed, **RS:** receiving slit

5.2.6.3 XRD

Structural characterization of the films was carried out by XRD method. Two different diffraction geometry was applied, *i.e.* 2θ and θ -2θ. Cu K_{α} radiation was employed as X-ray source.

All samples were rotated by 10-rpm speed during measurements and receiving slit was fixed to 0.3 mm to assure enough intensity recording with sufficient resolution.

X-ray diffraction measurement conditions were summarized for this study in Table 5.1.

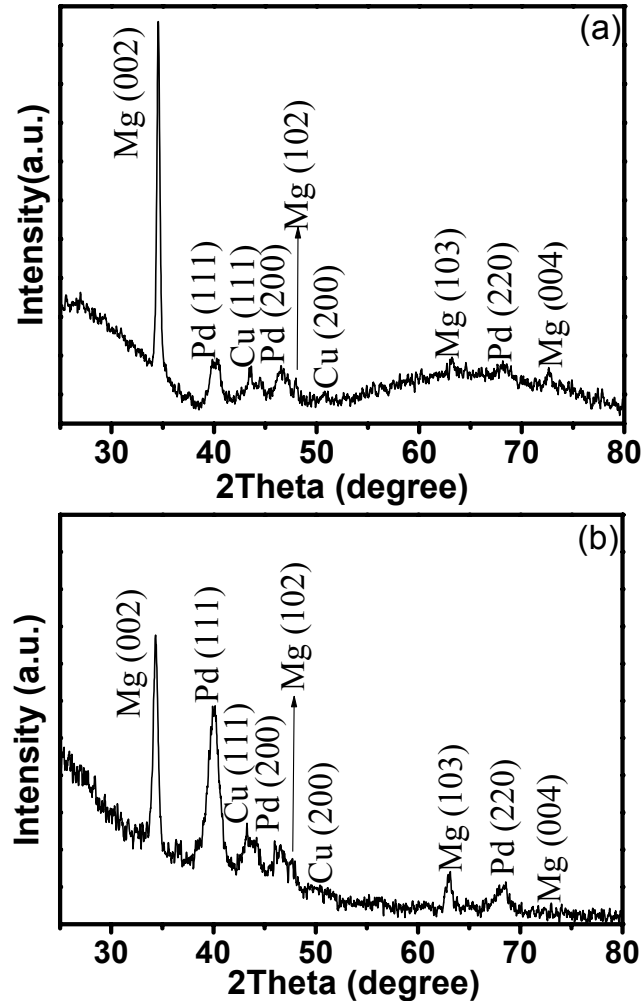


Figure 5.15 XRD patterns of as-deposited Mg-Cu/Pd thin film, a) θ - 2θ diffraction geometry, b) 2θ diffraction geometry.

As mentioned in details in Table 5.1, two diffraction geometries were applied for thin films, results of which are given in Fig. 5.15 (a) and (b). This two patterns illustrates that, for each diffraction conditions, there are no difference in the positions and numbers of the peaks obtained. The only difference is the intensity, as

expected. After this statement, all measurements were decided to carry out under θ - 2θ conditions.

5.3 RESULTS AND DISCUSSION

Mg-Cu films were produced via co-deposition method on glass substrates at two different substrate temperatures. Deposition was carried out to provide $[Cu/Mg] = 0.052, 0.111,$ and 0.176 atomic ratio in the final composition. Each composition (Mg-5,10, and 15 at. % Cu) was condensed at both 298 and 223 K. Hydrogen storage properties of thin films were followed by resistance measurements and X-ray diffraction methods.

5.3.1 Structural and Morphological Characterization

XRD patterns of 298 K deposited thin films are given in Fig. 5.16. Data reveals the crystalline nature of all compositions produced at this temperature. Increase in Cu concentration yielded a shift in the peak positions, and further line broadening was observed with increasing Cu content. As it has been well known, crystallite sizes can be calculated by employing Scherrer equation, (Wang *et al.* 2004, Huang *et al.* 2006). Although the results in thin films are controversial, it could be logical to interpret the trend of size change by this equation, depending on the conditions employed.

Crystallite sizes of thin films calculated by this approach are given in Table 5.2. The calculated crystallite size decreases as the Cu concentration increases in the film. In this respect, table confirms the refining effect with increasing Cu concentration, and explains the reason for peak broadening observed in XRD patterns. It is interesting to note that the calculated crystallite sizes for 298 K deposited Mg:Cu = 85:15 and 223 K deposited Mg:Cu=95:5 are so close to each other. This is an indication of refining also with substrate temperature reduction.

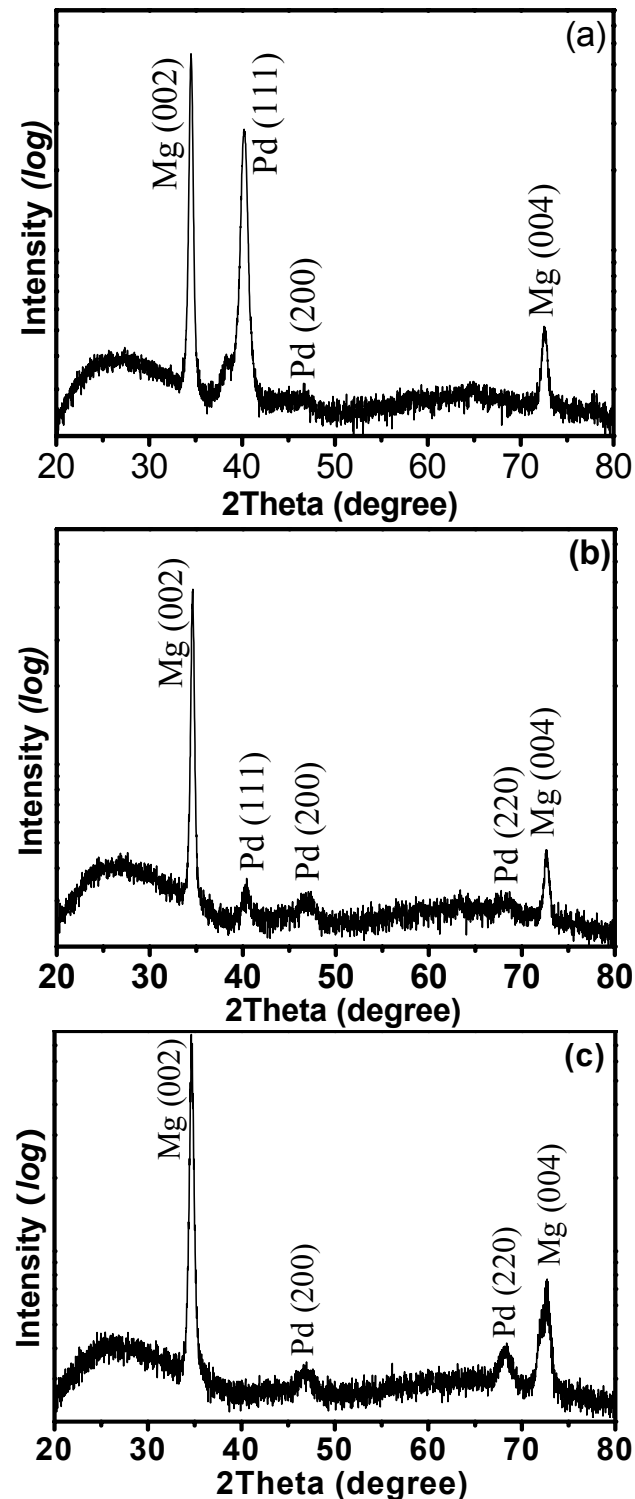


Figure 5.16 XRD patterns of 298 K as-deposited thin films, a) Mg:Cu=95:5, b) Mg:Cu=90:10, c) Mg:Cu=85:15.

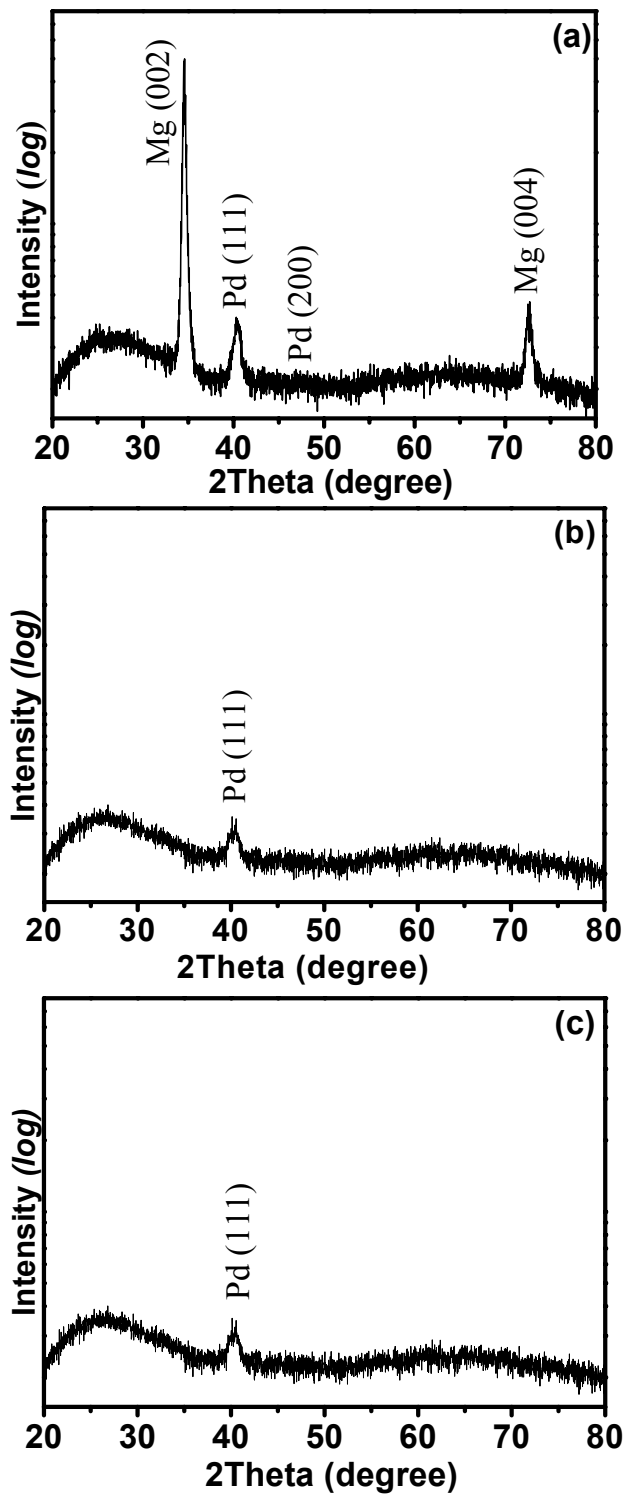


Figure 5.17 XRD patterns of 223 K as-deposited thin films, a) Mg:Cu=95:5, b) Mg:Cu=90:10, c) Mg:Cu=85:15.

XRD patterns of 223 K deposited thin films are given in Fig. 5.17. It is clear that at this substrate temperature, Mg:Cu=95:5 thin film deposits in crystalline structure. On the other hand, films with 10 and 15 at. % Cu was obtained to be amorphous.

Table 5.2 Crystallite sizes of thin films estimated from Scherrer equation.

<i>Crystallite sizes</i>	5 at. % Cu	10 at. %Cu	15 at. % Cu
T _S = 298 K	51.5 nm	44.8 nm	30.4 nm
T _S = 223 K	35.5 nm	Amorphous	Amorphous

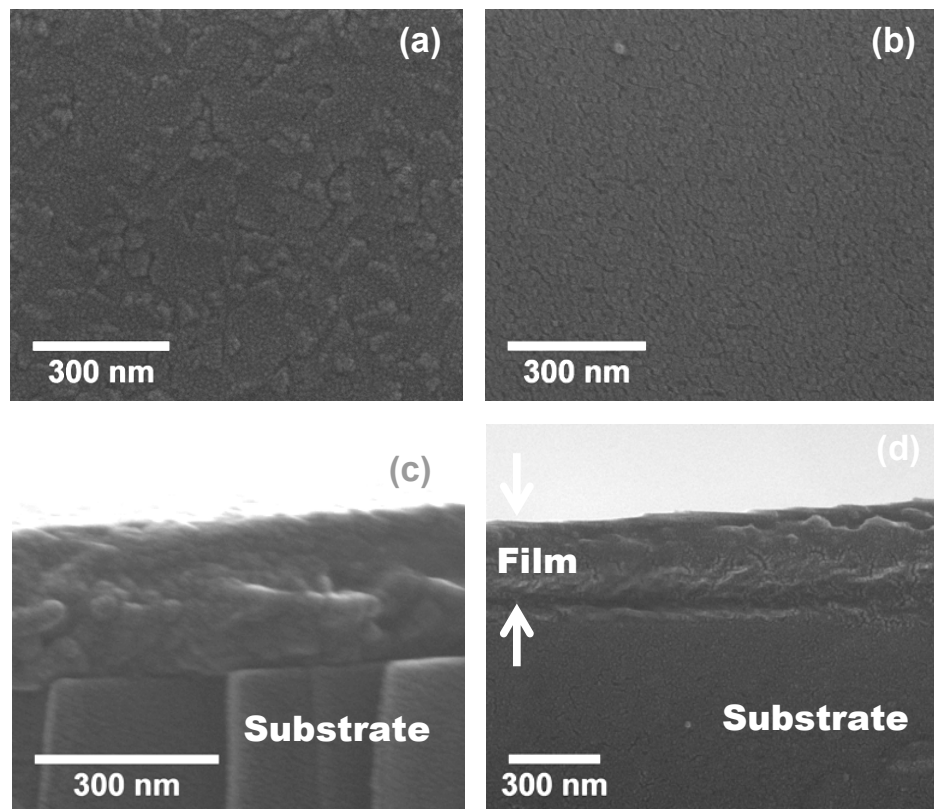


Figure 5.18 FE-SEM plane view and through thickness fracture surface images of Mg:Cu = 90:10 thin films, a) and c) 298 K deposited, b) and d) 223 K deposited.

Morphological examination by scanning electron microscope also confirms this statement. Fig. 5.18 shows FE-SEM images of the plane view and through thickness fracture surface of Mg:Cu = 90:10 thin film in as-deposited state, for two different substrate temperatures. Image for 223 K deposited sample illustrates that films deposited at 223 K substrate temperature has a rather smooth surface, when compared to the surface of the ones deposited at 298 K, please compare Fig. 5.18 (a) and (b). Cross sections also look rather different. High temperature film has a polycrystalline structure with equiaxed grains approximately 40 nm in size as measured with FE-SEM, as shown in Fig. 5.18 (c). With decreasing the substrate temperature, the film loses its grainy structure, as shown in Fig. 5.18 (c). The morphology observed here is also different than the morphology previously observed for crystalline thin films in Chapter 4, see Fig. 4.2.

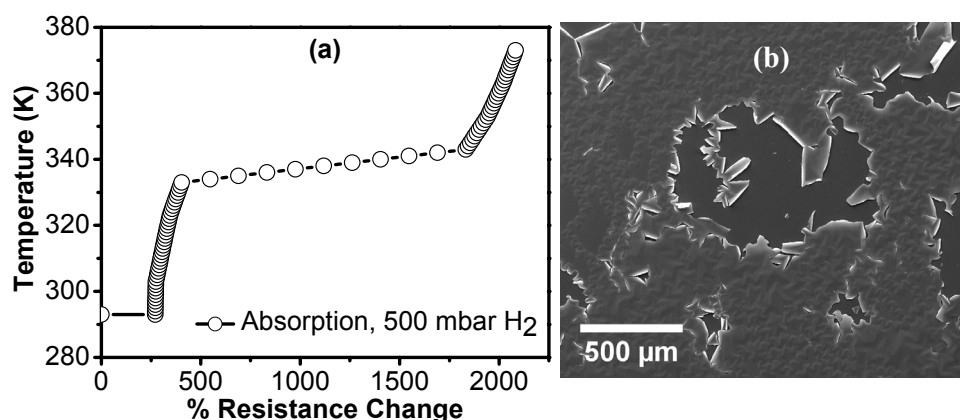


Figure 5.19 a) variation of the film resistance during hydrogenation as a function of temperature,(Mg:Cu=95:5, 500 mbar H₂) b) SEM surface image of the film after hydrogenation.

Fig. 5.19 (a) shows a typical temperature versus resistance plot obtained during hydrogenation. As a preliminary experiment, this sample was loaded with 500 mbar H₂ and heated up to 373 K. Heating rate was typically 1 K / min. As can be seen from Fig. 5.19 (a), resistance of the film is increasing with increasing temperature under constant hydrogen pressure. Scanning electron microscope image of the surface reveals the effect of hydrogenation on the film integrity, Fig. 5.19 (b). A

severe damage observed after hydrogenation where crack formation associated with peeling of the film from the substrate. This is a well known phenomenon for hydride materials, where hydrogenation of Mg leads to a volume expansion of approximately 34 %. Hydrogenation-resistance measurement experiments showed that a complete transformation to MgH₂ will eventually lead the film to failure. Due to this reason, it was decided to continue experiments under 100 mbar H₂ +1000 mbar Ar pressure, up to three different resistance values, relative to initial resistance of the films. For this purpose after initial hydrogen loading at RT, films were hydrogenated to 2, 3, and 5 times of the initial resistance values.

Table 5.3 Resistivity of as-deposited films

<i>Initial Resistivity</i>	5 at. %Cu	10 at. %Cu	15 at. %Cu
<i>Values ($\mu\Omega\text{cm}$)</i>			
T_S= 298 K	5.02	5.02	5.7
T_S= 223 K	5.55	8.32	9.67

As-deposited resistivity values of the films are given in Table 5.3. These values were calculated by conversion of the as-deposited resistance of the films to resistivity. During this conversion the thickness of the films were assumed as 300 nm without a thickness gradient in between the two measurement probes. The contact area of the probes with the film surface was also assumed as constant for all samples and the value was $62.4 \times 10^{-5} \text{ cm}^2$. Table illustrates that the values are varying as a function of Cu content and substrate temperature. This variation is in good agreement with the discussion given above for structural refinement in thin films. Further, the calculated resistivity values are similar to resistivity values reported in literature for pure Mg films (Gremaud *et al.* 2006 and Giebels *et al.* 2004). On the other hand, Mg-Ni, Mg-Al and Mg-Ti films were reported with resistivity values between 14.5 to 100 $\mu\Omega\text{cm}$ (Westerwaal *et al.* 2006, Gremaud *et al.* 2006 and Borsa *et al.* 2007). A 20 nm thick Pd capping layer was reported having

a resistivity value about $75 \mu\Omega\text{cm}$ (Giebels *et al.* 2004). So, the low resistivity obtained for the current study may be due to Cu content of the film.

A preliminary heating experiment was performed on a random sample with pure Ar (1100 mbar), to check whether temperature increase have any effect on the resistance of the film or not. As given in Fig. 5.20 there is only a 4 % change observed in the initial resistance of the film in between a temperature range of 293-433 K and further the initial value was recovered upon cooling the sample to room temperature. This proves that, any resistance increase observed during hydrogenation can only be related to hydrogen absorption. In addition, Pd layer also absorbs hydrogen but it will not cause any increase in the resistance due to it is metallic behaviour irrespective of its hydrogen concentration (Huiberts *et al.* 1996).

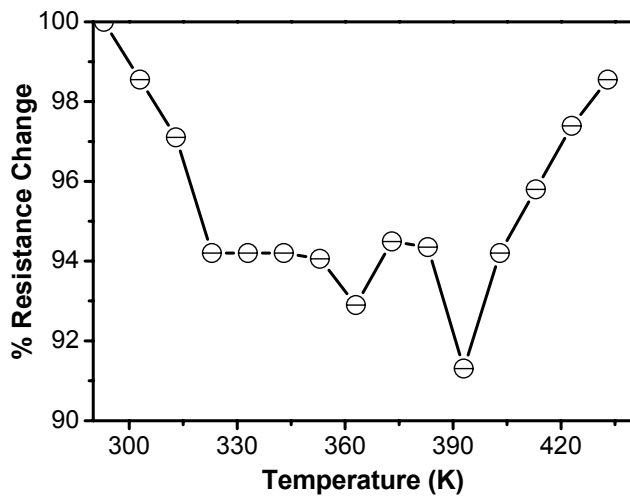


Figure 5.20 Resistance change of a random thin film sample under 1100 mbar Ar as a function of temperature.

Hydrogen sorption graphs of thin films are given in Fig. 5.21, 5.22, and 5.23. In these plots samples were hydrogenated to 5, 3, and 2 times of the initial resistance values of the samples, respectively. Each figure comprises of graphs that belongs to films deposited at 298 and 223 K. We will first discuss the results of 298 K deposited films.

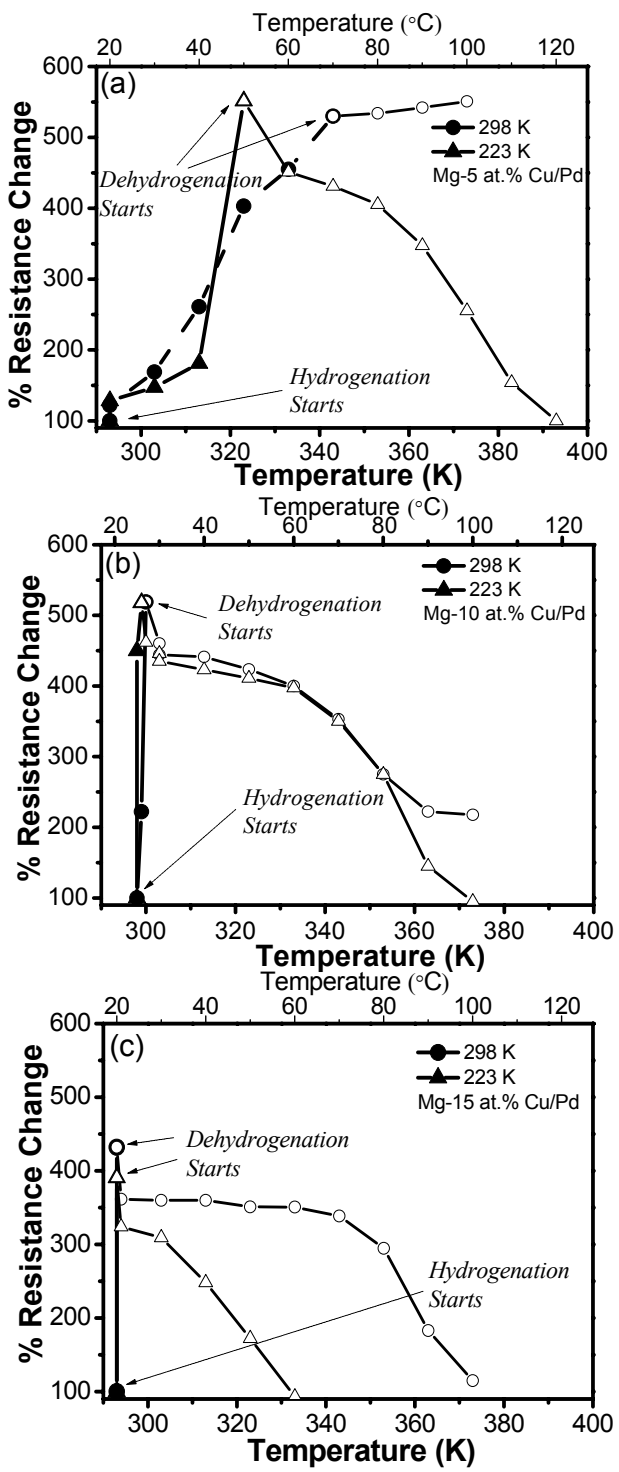


Figure 5.21 Temperature dependence of resistance (x5) for hydrogen absorption (solid markers) and desorption (open markers) a) Mg:Cu=95:5, b) Mg:Cu=90:10 and c) Mg:Cu=85:15 (Each figure comprises both 298 and 223 K deposited films).

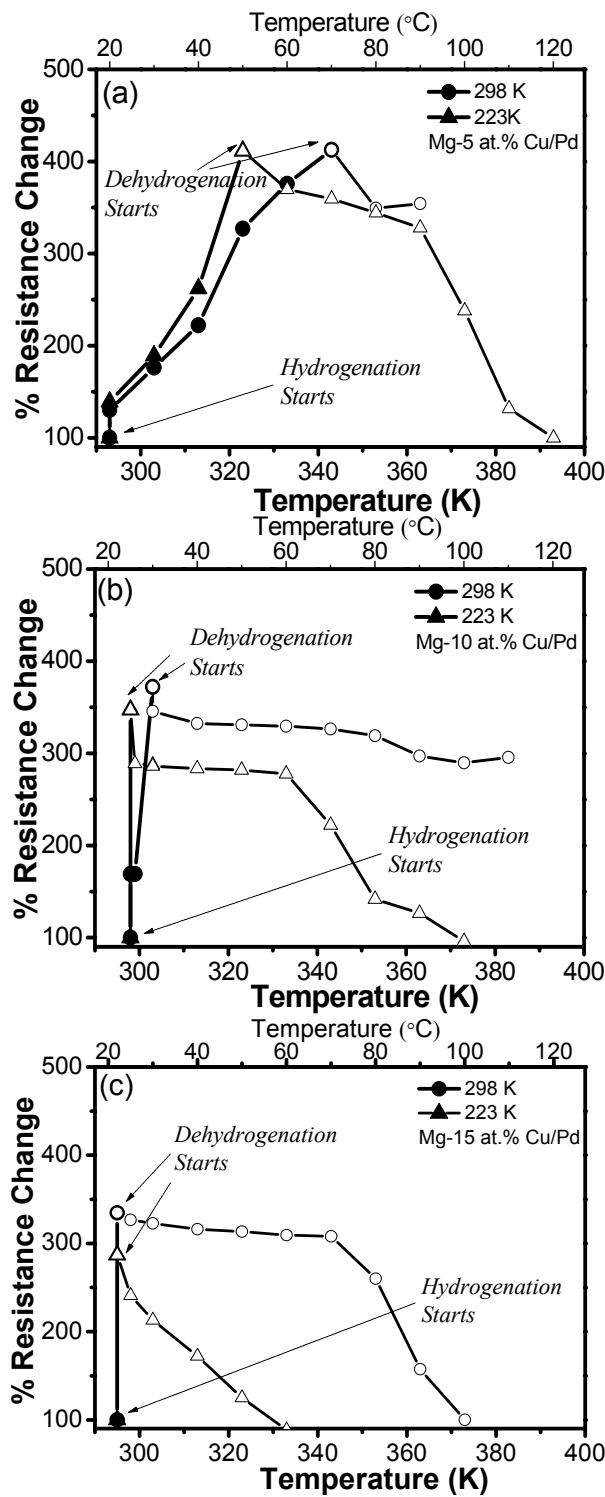


Figure 5.22 Temperature dependence of resistance (x3) for hydrogen absorption (solid markers) and desorption (open markers) a) Mg:Cu=95:5, b) Mg:Cu=90:10 and c) Mg:Cu=85:15 (Each figure comprises both 298 and 223 K deposited films).

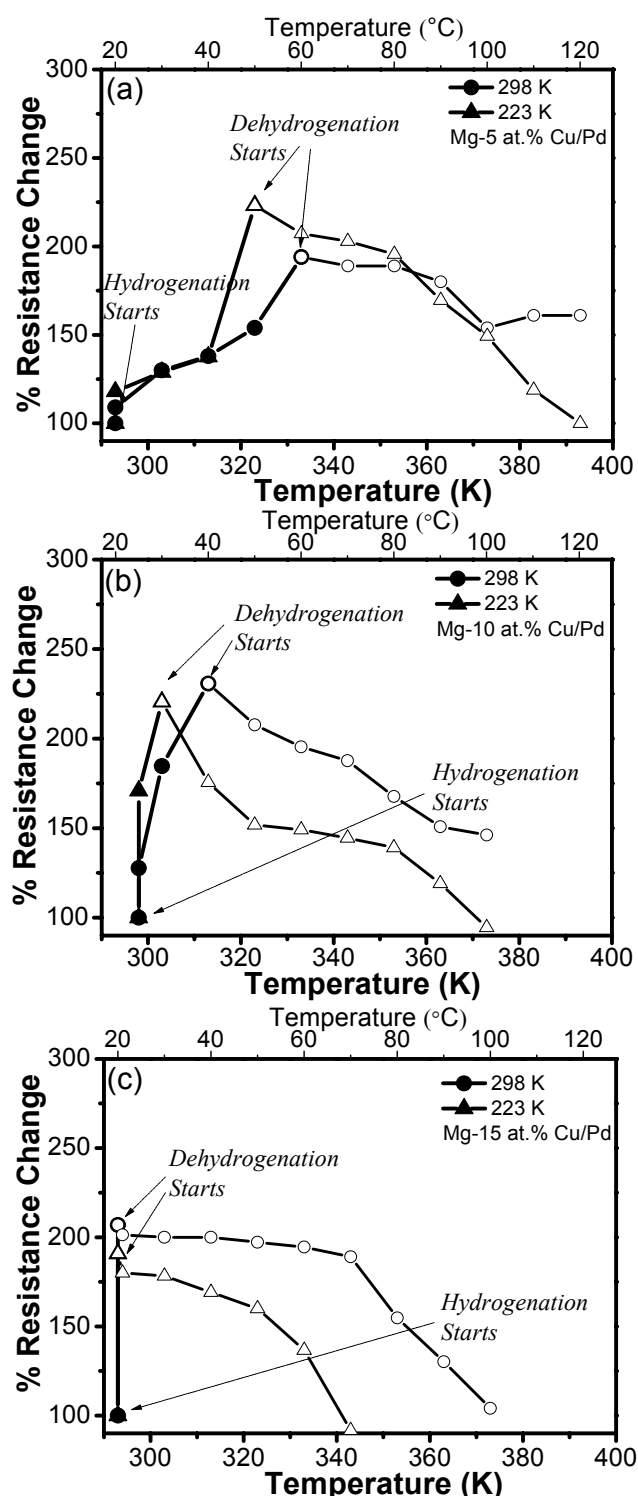


Figure 5.23 Temperature dependence of resistance (x2) for hydrogen absorption (solid markers) and desorption (open markers) a) Mg:Cu=95:5 b) Mg:Cu=90:10 c) Mg:Cu=85:15, (Each figure comprises both 298 and 223 K deposited films).

Fig. 5.21 (a) shows the resistance change for Mg:Cu=95:5 film composition. The resistance of the film is increasing up to 343 K with temperature. Once the resistance reached 5 times that of its initial resistance value, the gas in the cell was evacuated to a vacuum level of 10^{-1} mbar. After this point, we observed that the resistance keep rising up to the maximum temperature applied in this experiment, *i.e.* 423 K, accompanying a change in slope. While no drop observed in the resistance of this sample after evacuation of the cell, it is concluded that dehydrogenation was not occurred in this film. Here, a resistance drop was expected due to dehydrogenation as an analogy to relationship between resistance increase and hydrogen absorption. Further, it may be assumed that the dehydrogenation temperature of Mg:Cu=95:5 film is higher than 423 K.

Similarly, Fig. 5.21 (b) shows the variation of the film resistance with temperature for Mg:Cu=90:10 thin film. Graph indicates that the film absorbs hydrogen immediately after gas loading at room temperature. In addition to this, a substantial decrease in resistance occurs with increasing temperature up to 373 K just after evacuation of the gas mixture. However, this drop did not continue to the level of initial resistance value, which means that dehydrogenation was partial. Mg:Cu=85:15 reveals a similar behaviour, but this time the amount of resistance decrease was much higher. This sample could release almost all hydrogen up to 373 K, where absorption occurred at 293 K upon hydrogen loading, please see Fig. 5.21 (c).

Fig. 5.22 and 5.23 present results for each composition again for 298 K deposition, but hydrogenated to lower value of resistance increase, *i.e.* 3 and 2 times the initial resistance values, respectively.

Compositions of the films deposited at 223 K were evaluated within the same approach. Results were superimposed onto Fig. 5.21, 5.22 and 5.23 for comparison. Figures clearly indicate that films deposited at 223 K can dehydrogenate completely after evacuation of the cell. Further, recovery of the initial resistance value occurs at a much lower temperature.

Table 5.4 Hydrogen sorption temperature of thin films.

<i>Absorption temperature</i>	5 at. % Cu	10 at. % Cu	15 at. %Cu
T _s = 298 K	70 °C	25 °C	≤20 °C
T _s =223 K	50 °C	25 °C	≤20 °C
<i>Desorption temperature</i>			
T _s =298 K	>150 °C	>150 °C	100 °C
T _s =223 K	120 °C	100 °C	60 °C

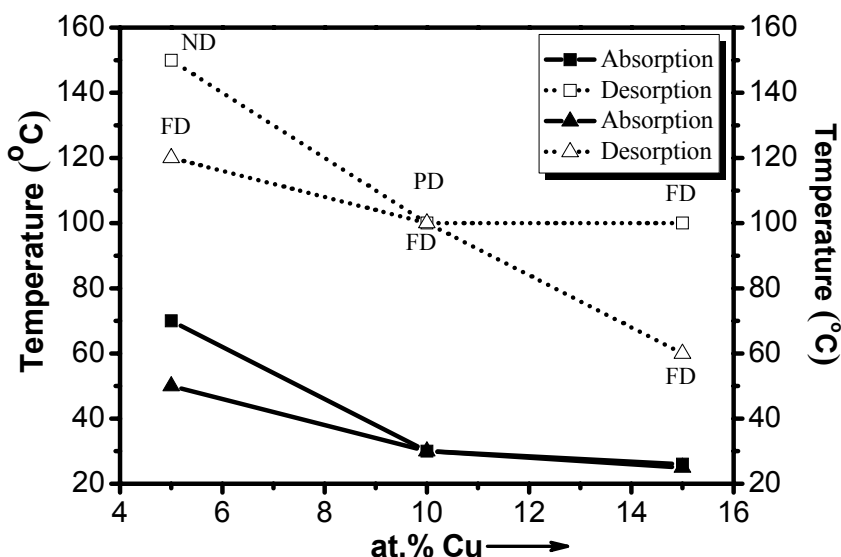


Figure 5.24 Hydrogen sorption temperatures of thin films as a function of Cu content and deposition temperature.

Hydrogen sorption temperatures of each composition estimated from resistance measurements are summarized in Table 5.4. Here T_s denotes the temperature of the substrate during deposition. Sorption temperatures as a function of Cu concentration are also given in Fig. 5.24 for both substrate temperatures. Abbreviations seen in the figure such as, ND, PD, and FD refers to no-desorption, partial desorption and full

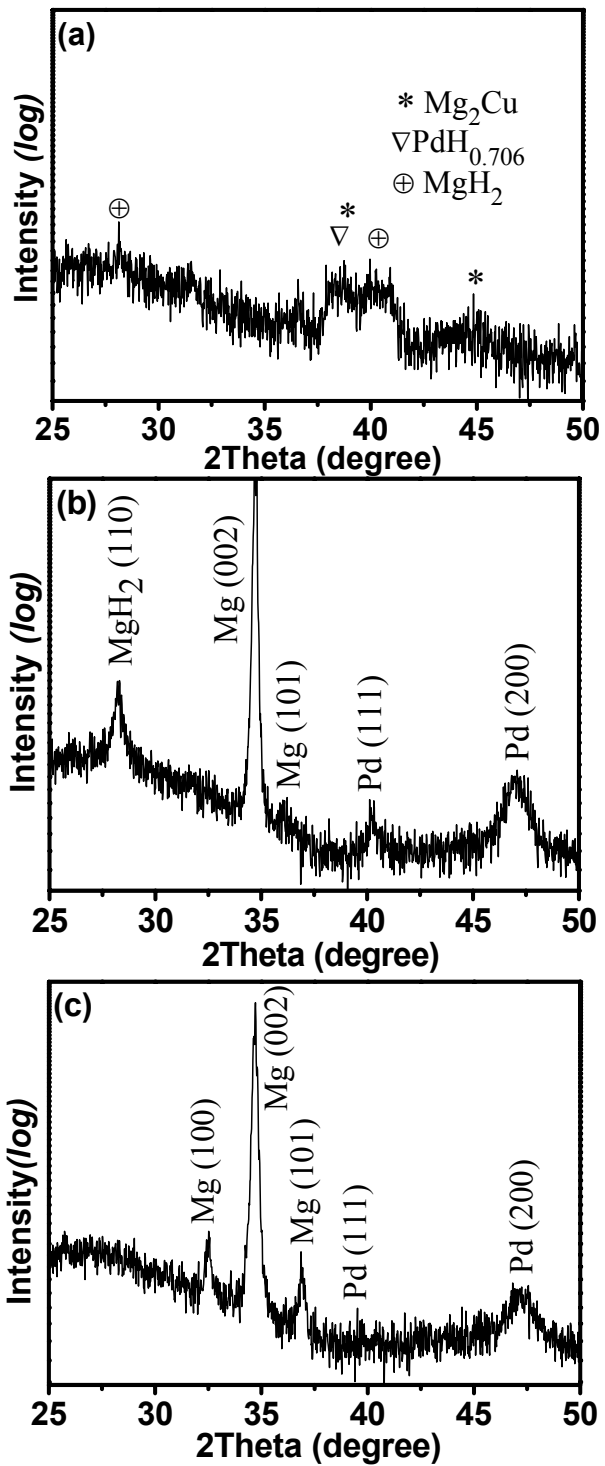


Figure 5.25 XRD patterns of 298 K deposited thin films after dehydrogenation, a) Mg:Cu=95:5, b) Mg:Cu=90:10, c) Mg:Cu=85:15 (Hydrogenation was performed up to five times of the initial resistance value).

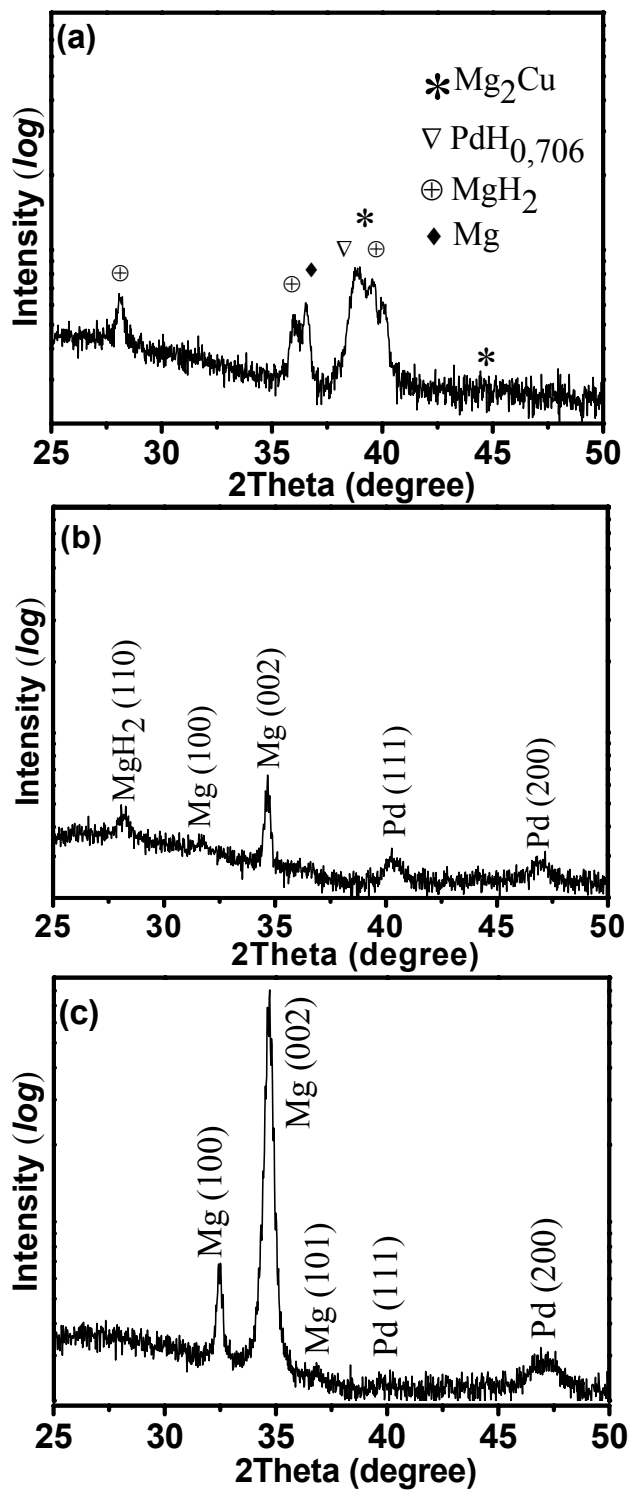


Figure 5.26 XRD patterns of 298 K deposited thin films after dehydrogenation, a) Mg:Cu=95:5, b) Mg:Cu=90:10, c) Mg:Cu=85:15, (Hydrogenation was performed up to three times of the initial resistance value).

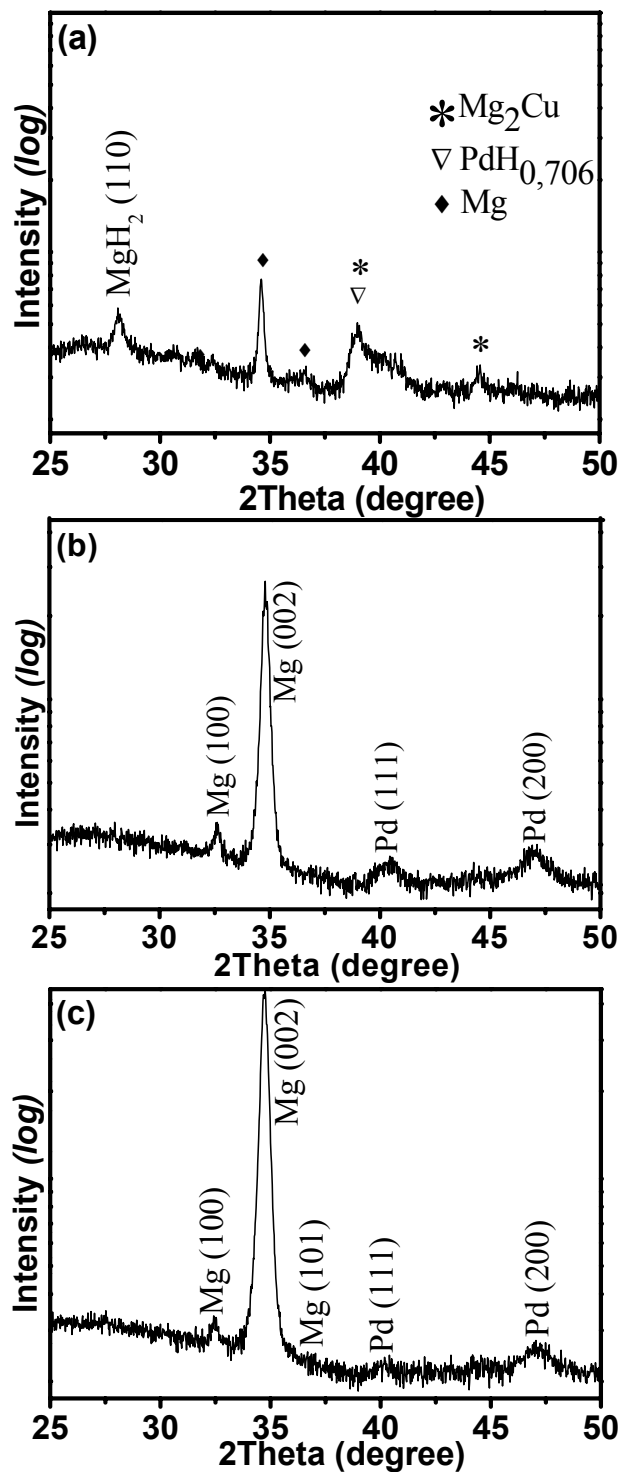


Figure 5.27 XRD patterns of 298 K deposited thin films after dehydrogenation, a) Mg:Cu=95:5, b) Mg:Cu=90:10, c) Mg:Cu=85:15, (Hydrogenation was performed up to two times of the initial resistance value).

desorption, respectively. Table 5.4 and Fig. 5.24, together proves that the sorption temperatures are decreasing with increasing Cu content whether the films were deposited at 298 or 223 K.

The temperature reduction for desorption is more pronounced, when the Cu content in the films increase from 10 to 15 at. %, *i.e.* 50 °C reduction and completed at a temperature of 100 °C, for 298 K deposited films. On the other hand, for 223 K deposited films, desorption already started at RT, and completed at around 60 °C, for 15 at. % Cu.

Films were structurally characterized in detail after resistance measurements. XRD patterns for 298 K deposited thin films are given in Fig. 5.25, 5.26, and 5.27 for Mg:Cu=95:5, Mg:Cu=90:10, and Mg:Cu=85:15 compositions, respectively. XRD data for 223 K deposited films are given in Fig. 5.28, 5.29 and 5.30 similarly for each composition.

Fig. 5.25 (a) shows XRD pattern of Mg:Cu=95:5 film after resistance measurement. As stated before, this film was hydrided up to 343 K and the curve showed no decline after unloading the gas mixture from the reactor.

Diffraction data reveals significant differences when compared to the data of as deposited film, see Fig. 5.17 (a) and 5.25 (a). It seems that hydrogenation leads to an amorphization in the structure. The profile does not provide clear indication of any phases similar to as-deposited state or MgH₂ and PdH_{0.706}, which may be expected after hydrogenation.

As discussed above, Mg:Cu=90:10 composition release most of the hydrogen after removal of the gas mixture from the cell; however, the resistance drop was not reached the initial value. Fig. 5.25 (b), confirmed this behaviour, and revealed that there is a substantial amount of Mg exists in the film, with a residual amount of MgH₂. It is also important to note that, Mg shows an orientation difference after dehydrogenation. In as deposited state film have a textured structure and Mg (002)

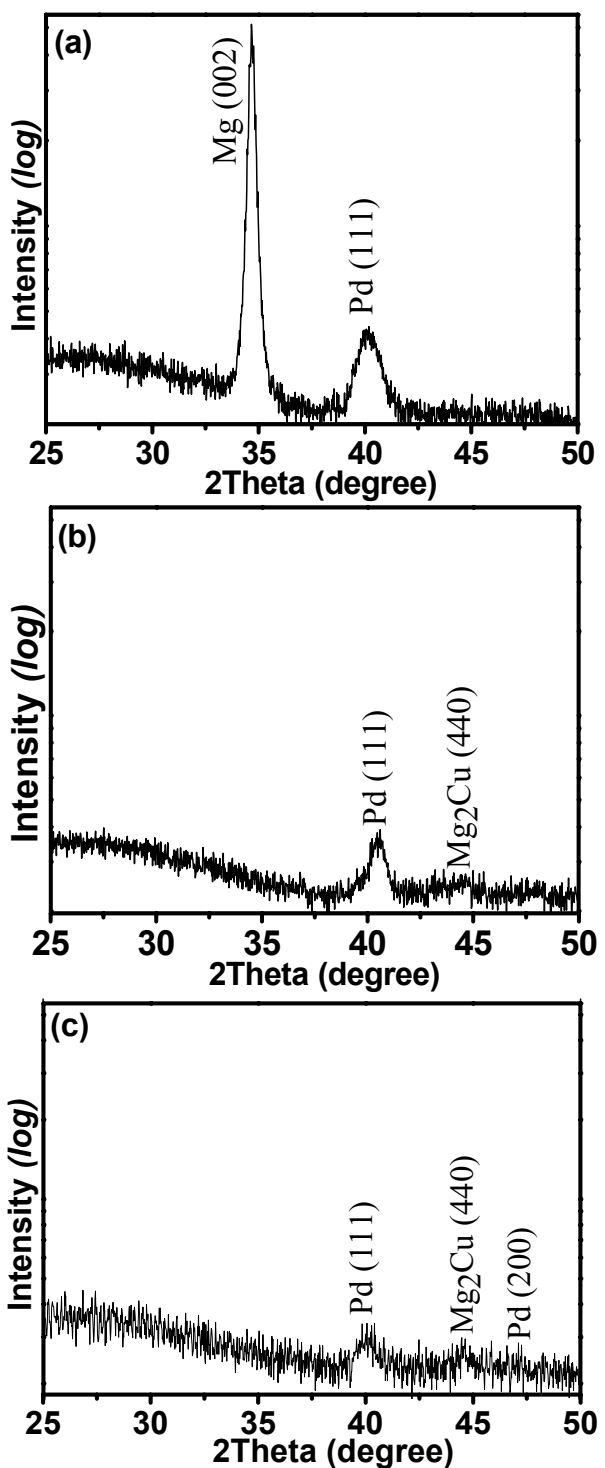


Figure 5.28 XRD patterns of 223 K deposited thin films after dehydrogenation, a) Mg:Cu=95:5, b) Mg:Cu=90:10, c) Mg:Cu=85:15, (Hydrogenation was performed up to five times of the initial resistance value).

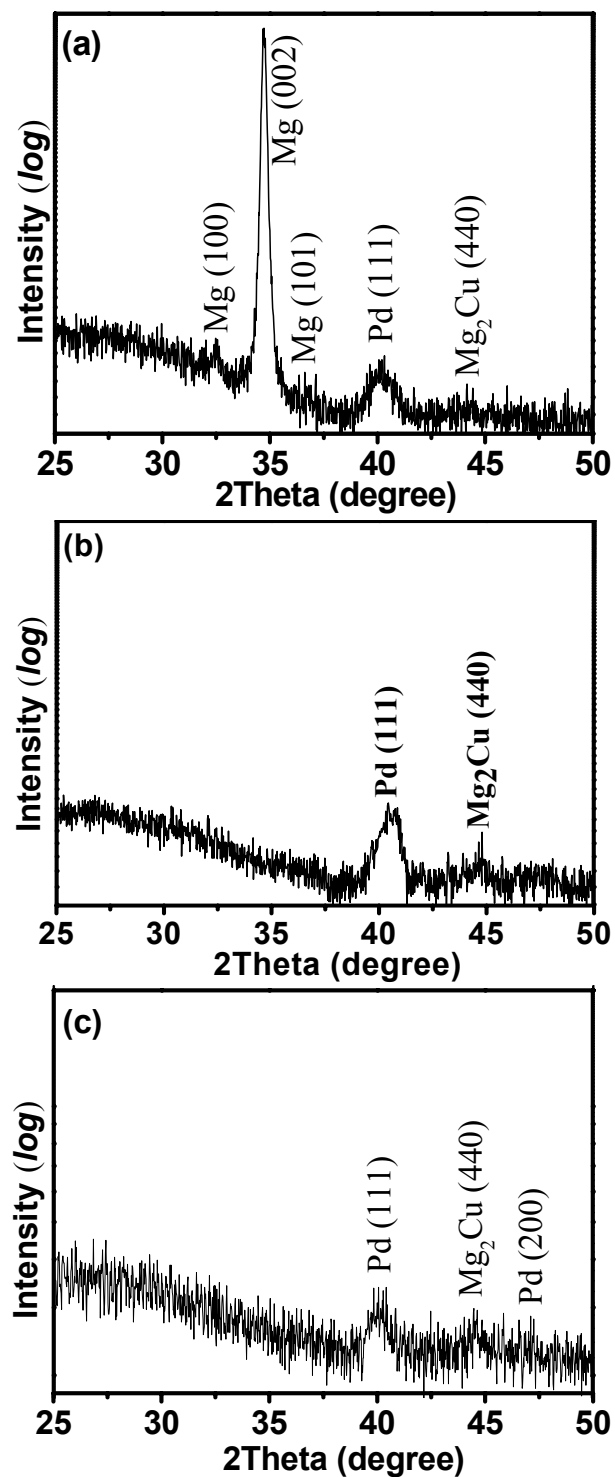


Figure 5.29 XRD patterns of 223 K deposited thin films after dehydrogenation, a) Mg:Cu=95:5, b) Mg:Cu=90:10, c) Mg:Cu=85:15, (Hydrogenation was performed up to three times of the initial resistance value).

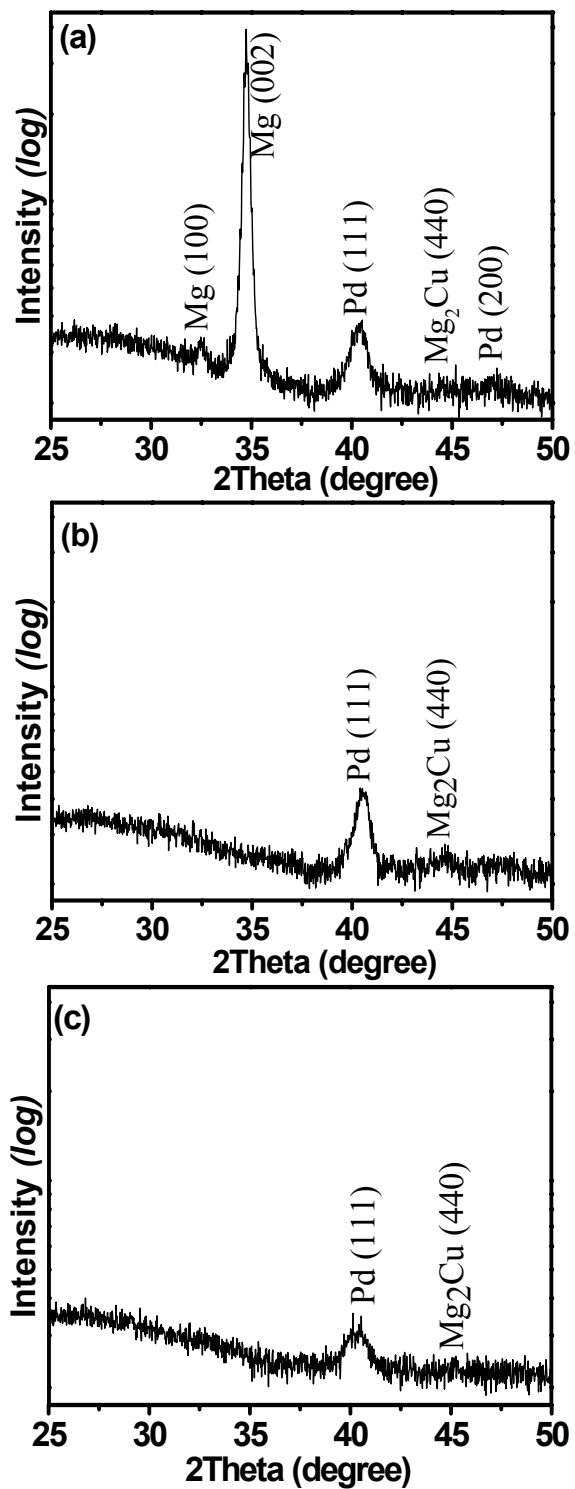


Figure 5.30 XRD patterns of 223 K deposited thin films after dehydrogenation, a) Mg:Cu=95:5, b) Mg:Cu=90:10, c) Mg:Cu=85:15, (Hydrogenation was performed up to two times of the initial resistance value).

and Mg (004) were the only diffracted planes, see Fig. 5.17 (b). On the other hand, after resistance measurements, an additional component of Mg observed, *i.e.* (101).

As indicated in resistance measurements, Mg:Cu=85:15 composition dehydrided completely. XRD profile of this film after dehydrogenation is consistent with those discussions and only reveals the peaks of Mg, but with three components in this case, *i.e.* (002), (100), and (101), Fig. 5.25 (c).

XRD pattern of 298 K deposited thin films after hydrogen loading up to 3 and 2 times of the initial resistance value are given in Fig. 5.26 and 5.27, in the same order within each figure. Measurements were performed after desorption. Data reveals similar results as discussed above for XRD measurement of the films for dehydrogenation after loading the samples up to 5 times the initial resistance of the films. All data obtained from XRD are consistent with the resistance measurements.

XRD profiles of thin films deposited at 223 K after dehydrogenation are given in Fig. 5.28 (a-c). These films were hydrogenated up to a resistance value of approximately five times of the initial resistance value. As can be seen from the profiles, no significant differences is observed between the as-deposited state and after dehydrogenation, refer to Fig. 5.18 (a-c) and Fig. 5.28 (a-c). As mentioned previously, these films were successfully hydrogenated and hydrogen was released completely for all compositions. XRD profiles of 223 K deposited thin films at lower hydrogenation levels (up to three and two times) are also given in the same order in Fig. 5.29 and 5.30. Patterns illustrate complete dehydrogenation for those films, consistent with the resistance measurement data.

Fig. 5.31 (a-c) shows FE-SEM planar surface images of the 298 K deposited thin films after dehydrogenation. Compositions of these films were Mg:Cu=95:5, Mg:Cu=90:10, and Mg:Cu=85:15. XRD patterns of these films are given above in Fig. 5.25, as in the same order.

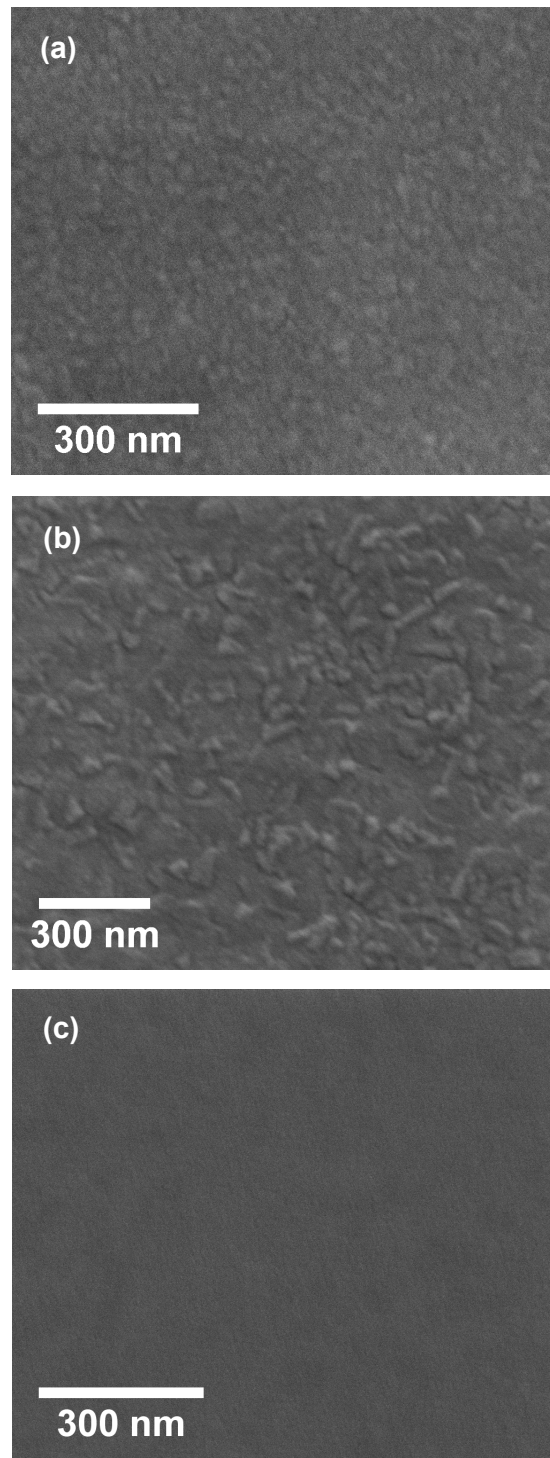


Figure 5.31 FE-SEM surface images of thin films after resistance measurement, (deposited at 298 K) a) Mg:Cu=95:5, b) Mg:Cu=90:10, c) Mg:Cu=85:15 (films were hydrogenated up to approximately 5 times of the initial resistance value).

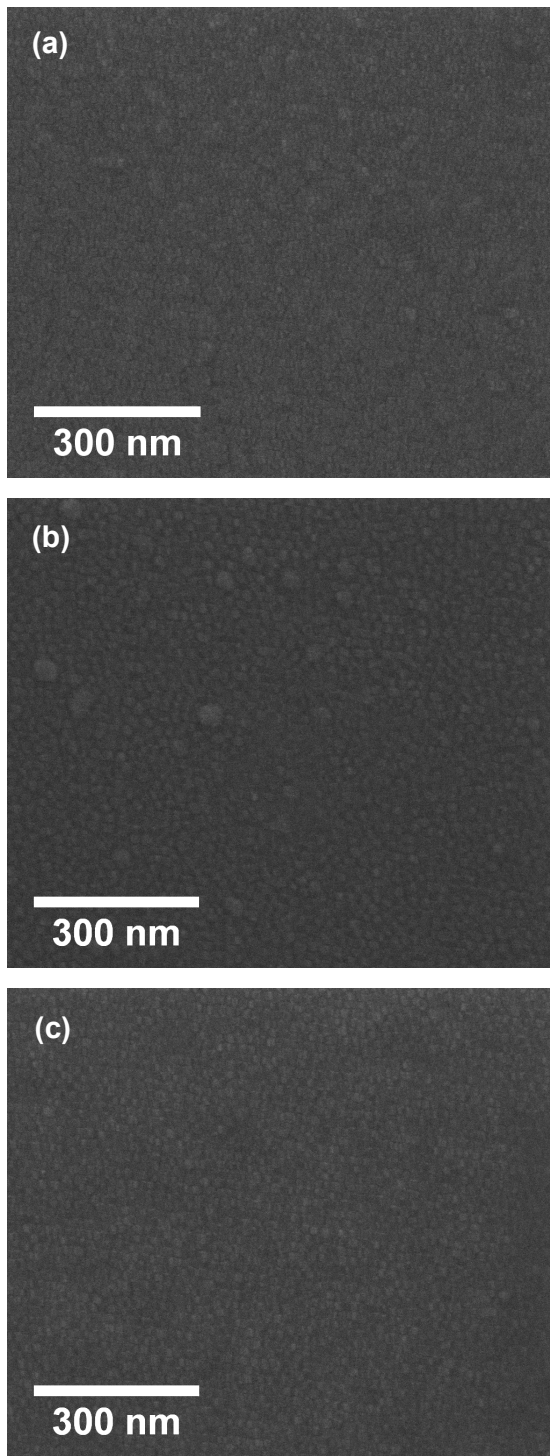


Figure 5.32 FE-SEM surface images of thin films after resistance measurement, (deposited at 223 K) a) Mg:Cu=95:5, b) Mg:Cu=90:10, c) Mg:Cu=85:15 (films were hydrogenated up to approximately 5 times of the initial resistance value).

Scanning electron microscope images illustrate formation of an altered surface topography after resistance measurements. Grain sizes of the films as measured with FE-SEM are in between 30-50 nm for Mg:Cu=95:5, and 40-50 nm for Mg:Cu=90:10 which are given in Fig. 5.31 (a) and (b), respectively. Measurements are in good agreement with the crystallite size estimations given before in Table 5.2. The surface image of Mg:Cu=85:15 after dehydrogenation does not reveal any feature, as shown in Fig. 5.31 (c).

Fig. 5.32 (a-c) shows FE-SEM planar surface images of 223 K deposited thin films after dehydrogenation. These were Mg:Cu=95:5, Mg:Cu=90:10, and Mg:Cu=85:15. XRD patterns of these films were given above in Fig. 5.28 as in the same order.

After resistance measurements, Mg:Cu=95:5 sample has equiaxed grains on the surface around 30-35 nm in size, Fig. 5.32 (a). With increasing Cu content, grains are also decreasing in size and reducing to 10-15 nm for Mg:Cu=85:15 sample, Fig. 5.32 (c). However, the image for Mg:Cu=90:10 film illustrates a bimodal grain distribution as measured by FE-SEM, *i.e.* 15 nm and 40 nm, Fig. 5.32 (b). As discussed earlier, this film remained as X-ray amorphous after resistance measurements. So, these larger grains observed on the surface may also be due to the Pd overlayer on the surface. On the other hand, the same is not valid for Mg:Cu=85:15 sample, which was behaved almost similar to Mg:Cu=90:10 sample during resistance measurements.

Mg:Cu=85:15 film was subjected to subsequent hydrogenation-dehydrogenation experiments to examine the cyclic behaviour of the sample. For this purpose, 100 mbar of hydrogen was exposed on the sample at 323 K. After completion of absorption, the system was opened to vacuum then the valve was closed and the system isolated. Dehydrogenation behaviour was followed by plotting the change in resistance as a function of time for each cycle and collected data given in Fig. 5.33. As can be seen from figure, dehydrogenation kinetics improved with cycling and for the 3rd cycle all hydrogen could be desorbed within 30 min. from the sample. After the 3rd cycle, the reaction time for complete desorption increased with subsequent

loading-unloading and reached to 100 min. at the 8th cycle. Dramatic change in time occurs after the 6th cycle where after dehydrogenation, resistance decreases of about to 30% lower than the initial resistance of the film in as deposited state. Similar behaviour was reported by Hjort *et al.* 1996 and Ingason and Olafsson 2005. However, they indicated an irreversible increase in the initial resistance-resistivity value after each successive sorption cycle. Hjort *et al.* 1996 attributed this irreversible increase to the morphological changes (*i.e.* lattice defects, changes in grain size and micro-cracks in the sample) induced by the volume expansion-contraction accompanying the sorption cycles. In our case, the decrease in resistance may be occurred due to redistribution of the Cu atoms in the structure with each cycle.

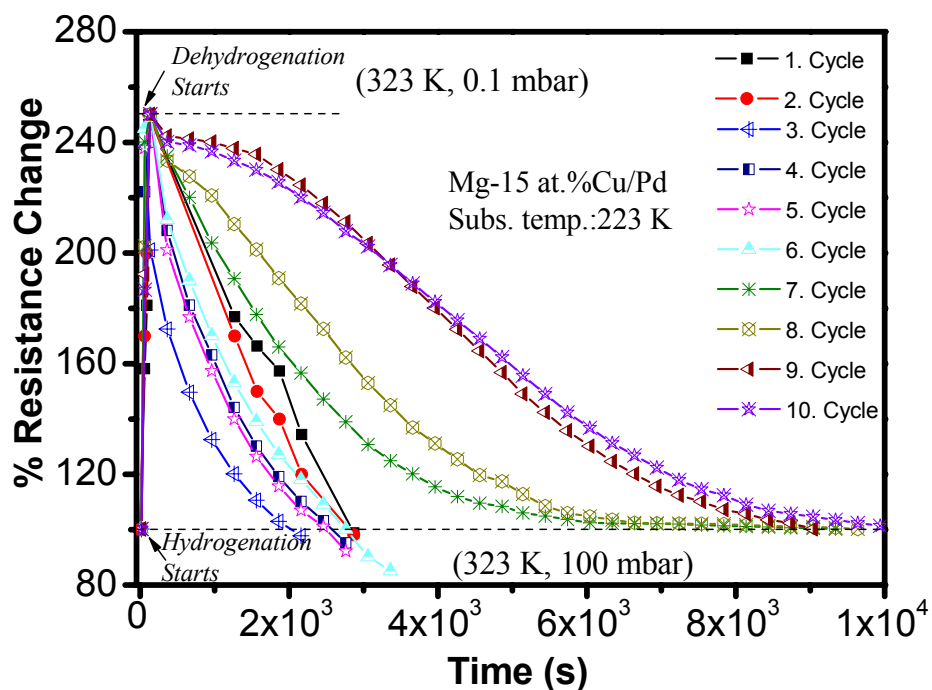


Figure 5.33 Resistance change in 223 K deposited Mg:Cu=85:15 thin film during hydrogen loading-unloading cycles at 323 K. (Sorption experiments were applied at constant temperature and pressure, absorption at 100 mbar H₂ and desorption at 0.1 mbar residual hydrogen atmosphere).

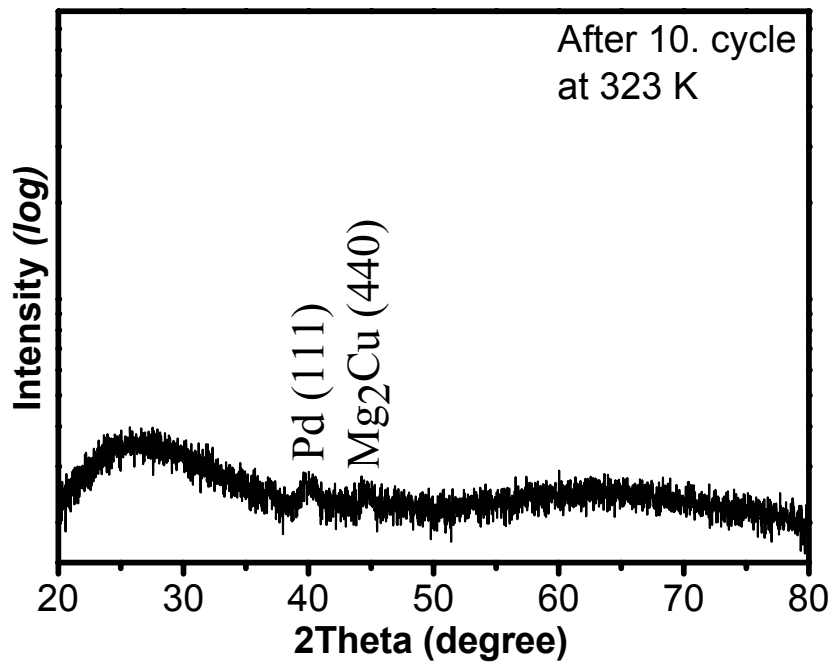


Figure 5.34 XRD pattern of Mg:Cu=85:15 thin film after 10 hydrogen loading-unloading cycle.

XRD pattern of this film after 10th cycle is given in Fig. 5.34. The profile is almost similar to as-deposited state, see Fig. 5.18 (c), except the intermetallic phase formation, which is Mg₂Cu. The formation of this intermetallic phase may be accepted as an indication of severe effect of hydrogen loading/unloading cycles on the chemical make-up of the structure, because all these cycles were performed at just 50 °C.

Fig. 5.35 gives the FE-SEM images of the same sample in as-deposited, hydrided and dehydrided states. It is clear that with repeated hydrogen loading-unloading cycles structural disintegration was occurred in the sample. It is also interesting to note that XRD patterns did not revealed any peaks, whereas grains are clearly visible from fracture surfaces in Fig. 5.35 (b) and (c). This may be due to severe pulverization at the interior of the grainy features during hydrogenation-dehydrogenation cycles.

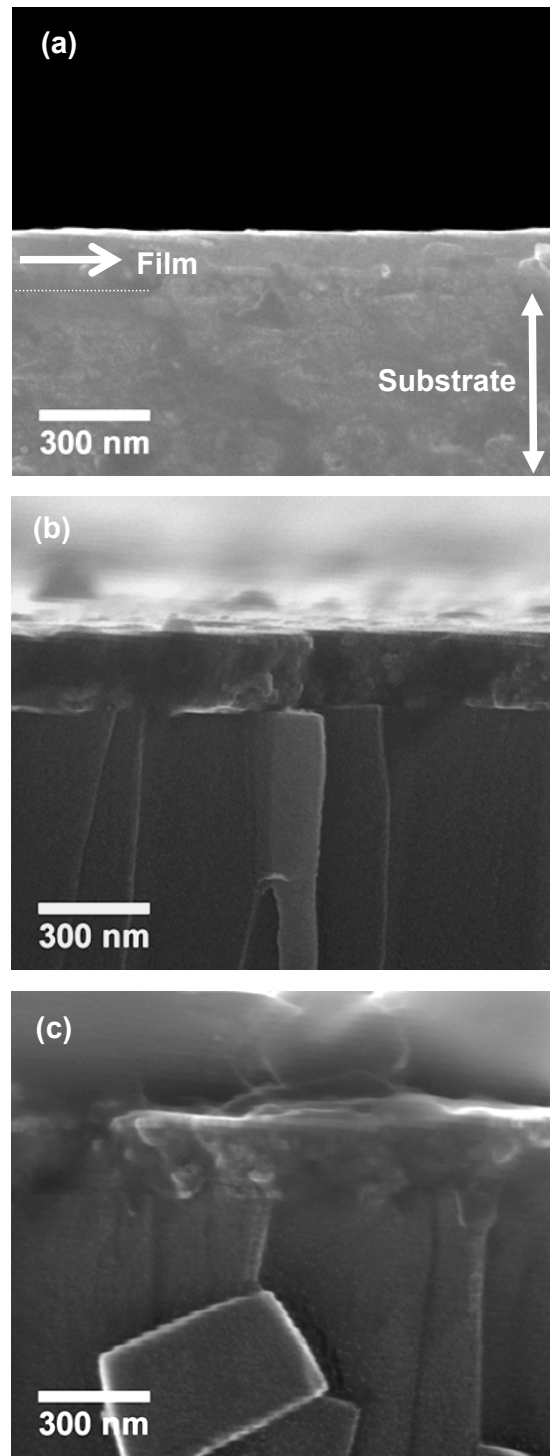


Figure 5.35 Through thickness fracture surface FE-SEM images of Mg:Cu=85:15 thin film deposited at 223 K a) as-deposited, b) hydrogenated under 100 mbar hydrogen pressure at 323 K up to approximately 5 times of the initial resistance value c) dehydrided after 10th cycle.

The study showed that films with nano-sized grains as well as amorphous structures have advantages in terms of hydrogen sorption behaviour compared to crystalline and coarser grained counterparts. Further, it can be decided that, deposition method and substrate temperature are the two important parameters affecting the final structure of the films. Andrievski 2007 has discussed on the details of hydrogen in nanostructures. In his review, based on the literature data, he stated that maximum hydrogen content in nano- and amorphous hydrides are generally lower compared to ordinary hydrides of the same composition. He further stated that, in terms of nanostructures it is important to clarify how hydrogen is localized in the interior of the grains and at the grain boundaries and what are the possible interactions of this with the defects within the structure of the material. In fact, most of the predictions or indications in this study based on the powder processed samples (*e.g.* Ares *et al.* 2005), and this does not generalize the same for thin film structures.

On the contrary to scattered and scarce data in literature, in this study we observed a systematic relationship for absorption/desorption of hydrogen and structure refining and reproducibly improved results with amorphization. Finally, it is worth to mention that, the relationship between the improved hydrogen sorption behaviour and structure refining/amorphization needs further study with advanced techniques on kinetics and thermodynamics of hydrogen sorption to clarify the obscureness on the topic.

5.4 CONCLUSIONS

In this study, thin films of Mg-Cu were produced via co-deposition by thermal evaporation method, under UHV conditions. Deposited compositions were Mg:Cu=95:5, Mg:Cu=90:10 and Mg:Cu=85:15. All films capped with a Pd layer of 5-25 nm and film thicknesses were 250-300 nm. Two different substrate temperatures was used for film formation, *i.e.* 298 and 223 K. Structural characterizations and hydrogen sorption studies have shown that;

1- Increasing Cu content leads to structural refinement. In addition to this, decrease in substrate temperature yields a finer structure for the same composition. Further, it was shown that films with compositions Mg:Cu=90:10 and Mg:Cu=85:15 were formed in X-ray amorphous state at a substrate temperature of 223 K.

Resistance measurements revealed that;

2- A strong relationship was examined between the structural refinement and hydrogen sorption temperatures. By reduction in size, hydrogenation behaviour was observed to improve in terms of sorption temperature such that both necessary temperatures for hydrogenation and dehydrogenation were decreased. Under the experimental conditions applied, Mg:Cu=85:15 thin film composition deposited at a substrate temperature of 223 K yielded the best results in terms of hydrogen storage. This film could easily absorb hydrogen at room temperature and desorption occurs at temperatures not higher than 323 K starting from room temperature.

Based on the current work, it is further concluded that an amorphous alloy of Mg:Cu=90:10 can be recommended as a hydrogen storage medium as it can be expected to store theoretically 5.9 wt.% hydrogen in near ambient conditions, and can desorb it at around 100 °C.

CHAPTER 6

MAXIMIZING HYDROGEN STORAGE CAPACITY OF Mg-BASED THIN FILMS

This chapter aims to maximize the storage capacity for the purpose of obtaining amorphous Mg with as little alloying addition as possible. In Mg-Cu system as reported in the previous chapter the following have been observed. Mg-10 at. % Cu and Mg-15 at. % Cu deposited at 223 K resulted in amorphous thin films. The former alloy *i.e.* Mg-10 at. % Cu was recommended as hydrogen storage medium as it can store 5.9 wt. % hydrogen at room temperature and can desorb it at around 100 °C. 10 at. % Cu corresponds to 21.87 wt. % Cu and therefore a considerable portion of the alloy is a non-absorbing element.

Since our target is to maximize the storage capacity it would be ideal to use Mg in its pure state. Therefore, we will investigate whether or not it is possible to obtain Mg in amorphous form. However, before questioning this, we will first evaluate the cooling rate as it is achieved in the present experimental condition.

The evaporation rate is a product of the vapor density multiplied by the propagation velocity. If the vapor originates from a melt, the density is governed by Arrhenius law, *i.e.* it depends exponentially on the temperature of the source. Atoms or molecules which are evaporating from solid surfaces are usually assumed to have a Maxwellian velocity distribution, characteristic of a temperature, equal to that of solid (Arthur and Brown 1975). Thus, the average kinetic energy, E_{av} , of the vapor molecules leaving the surface corresponds to the surface temperature T_w , which is defined by;

$$E_{av} = \frac{3}{2} kT_w \quad (6.1)$$

where k is the Boltzmann constant.

For most materials $(3/2)kT$ is about 0.2 eV per atom (Berry *et al.* 1968). Thus, for amorphization that much energy has to be absorbed from each atom during condensation.

In addition, we know that the particles undergo frequent collisions and will not have a constant velocity or mobility in a specific direction. The Maxwell-Boltzman frequency distribution is used to describe the non-uniform distribution of particle velocities, (v) brought about by collision and given by;

$$f(v) = \frac{4}{\sqrt{\pi}} \left(\frac{M}{2RT} \right)^{3/2} v^2 \exp - \frac{Mv^2}{2RT} \quad (6.2)$$

Here M is the molecular weight, T is the temperature and R is the gas constant per mole. From Maxwell-Boltzmann distribution, most probable (v_m), average (\bar{v}) and mean square velocities (v^2) are given respectively as;

$$v_m = \sqrt{\frac{2RT}{M}} \text{ ms}^{-1}, \quad \bar{v} = \sqrt{\frac{8RT}{\pi M}} \text{ ms}^{-1}, \quad v^2 = \sqrt{\frac{3RT}{M}} \text{ ms}^{-1} \quad (6.3)$$

Considering the current experimental conditions and assuming the vapor flux is directional in the apparatus, then the mean square velocity; v^2 of Mg can be calculated as; 973 ms^{-1} . The distance between the substrate and the source is 30 cm. Thus, the time required for a Mg atom (which was emitted normal to substrate surface) to reach the substrate after vaporization is; $3.082 \times 10^{-4} \text{ s}$.

In fact, vaporized atoms obey the cosine law, which relates the distance to angle of substrate and source normal. From literature, we know the vaporization temperature of Mg and the temperature of the substrate where the Mg atoms are depositing.

Then, the corresponding cooling rate when the substrate was cooled to 298 K is 2.028×10^6 K/s. Similarly, it is 2.27×10^6 K/s when the substrate was cooled to 223 K.

A more realistic estimate of cooling rate may be obtained by taking into account the evaporation temperature of Mg corresponding to vacuum level of the chamber. The evaporation temperature of Mg at the vacuum level of 1×10^{-7} mbar is 480 K. Under these conditions cooling rate is expected to be; 5.9×10^5 K/s for 298 K and 8.3×10^5 K/s for 223 K deposited films.

The whole calculation assumes that the mean free path (λ_{mfp}), is higher than the distance between the substrate and the source (at 10^{-6} mbar, it is about 100 m), thus the collision occurs only with the walls of the vacuum chamber. According to cooling rates calculated above, in the current experimental conditions, it seems that the cooling rate achieved is typical of that associated in melt spinning or splat quenching (Tkatch *et al.* 2002, Kang *et al.* 1994)

Table 6.1 gives a list of elements from IA, IIA, early and late transition metals, poor metals, metalloids and non-metals. This table is constructed from the reported elements in literature, which was amorphized upon quenching from the liquid or from the vapor phase. Table also includes elements which do not form amorphous structure and those which can be obtained in amorphous form only when alloyed with other elements. The classification here based on the bond energy, given in the second column of the table. The values are calculated using the heat of atomization and bulk coordination number of the metal under consideration, (Vijh 1975). The shaded elements, except Mg, on the table, could all be obtained in amorphous form when quenched with a sufficiently high cooling rate.

Table 6.1 Pure amorphous elements classified according to their bond energy and quenching technique. Elements which could form amorphous structure when alloyed with other elements are also included.

Element	Bond Energy (kcal/mole)	T _M (°C)	Cryst. Str.	Pure/Alloy	Prod. Met.
K	5.4	63.65	BCC	No data	-
Na	4.4	97.8	BCC	No data	-
Be	13	1278	HCP	When Pure	VD
Mg	6	650	HCP	When Alloyed	VD
Ca	7.3	839	FCC	When Alloyed	MS
Ti	18.8	1660	HCP	When Pure, Cryst.	IBS,SQ
Y	16.7	1523	HCP	When Alloyed	SQ
Zr	24.4	1852	HCP	When Pure	VD
Hf	28	2150	HCP	When Pure	VD
Re	-	3180	HCP	When Pure	VD
Nb	43.1	2408	BCC	When Pure	VD
Ta	46.7	2996	BCC	When Pure	VD
Cr	23.6	1857	BCC	When Pure	VD
Mo	39.6	2617	BCC	When Pure	VD
W	50.5	3410	BCC	When Pure	VD
V	30.8	1890	BCC	When Pure	VD
Fe	16.6	1535	BCC	When Pure	VD
Ru	25.8	2250	HCP	When Pure	IBS
Os	31.2	3045	HCP	When Alloyed	VD
Co	16.9	1495	HCP	When Alloyed	VD
Rh	22.1	1966	FCC	When Pure	SQ
Ir	26.5	2410	FCC	When Alloyed	VD
Ni	16.9	1453	FCC	When Pure, crystalline	VD, SQ
Pd	15	1552	FCC	When Pure	SQ
Pt	22.7	1772	FCC	When Alloyed	SQ

Table 6.1. Continued,

Element	Bond Energy (kcal/mole)	T _M (°C)	Cryst. Str.	Amorp. State	Prod. Met.
Cu	13.5	1083	FCC	When Alloyed	VD
Ag	11.4	961.98	FCC	When Alloyed	VD
Au	14.6	1064.48	FCC	When Alloyed	VD
Zn	10.4	419.48	HCP	When Alloyed	RFS
Cd	8.9	320.9	HCP	When Alloyed	VD
Al	12.5	660.37	FCC	When Pure	VD
Ga	25.5	29.78	Orthorh.	When Pure	VD
Pb	7.8	327.5	FCC	When Pure	VD
In	9.5	156.61	Tetrag.	When Pure	FE
Sn	12.1	231.9	Tetrag.Cubic,A4	When Pure	VD
Bi	16.6	271.3	Rhomb.	When Pure	VD
Tl	7.2	303.5	HCP	When Alloyed	VD
Si	53.02	1410	Cubic,A4	When Pure	VD
Ge	44.9	937.4	Cubic,A4	When Pure	VD
B	69.98	2300	Rhomb.	When Pure	VD
Sb	20.9	630	Rhomb.	When Pure	VD
As	34.87	817	Rhomb.	When Pure	VD
Te	14.9	449.5	Hex,A8	When Pure	VD
C	80	3500	Cubic,A4Hex.	When Pure	VD
Se	49.2	217	Hex,A8	When Pure	VD

(VD: Vapor Deposition, FE: Flash Evaporation, RFS: RF Sputtering, SQ: Splat Quenching, IBS: Ion-Beam Sputtering, MS: Melt Spinning) Table adapted from Barman *et al.* 2006, Boakye 1993, Buckel 1969, Chandramohan *et al.* 2006, Chopra 1969, Comberg *et al.* 1974, Companian 1972, Deiss 1988, Hunderi and Myers 1974, Kewei 2002, Khelfa *et al.* 1994, Kolk 1988, Takayama 1976, Tan *et al.* 2006, Vijh 1975.

It should be noted that the elements that form amorphous structure are those that have high bond energy when compared with other elements in their own group. For instance, in alkaline earth elements, Be has the highest bond energy, *i.e.* 13 kcal/mol,

and only Be was reported to be amorphous when vapor deposited. Mg and Ca which are in the same group have lower bond energy (6 and 7.3 kcal/mol) and can be produced in amorphous form when alloyed with other elements. The bond energy appears to be an applicable parameter in explaining the formation of amorphous phase in almost all groups. However, there are some exceptions like Pt in late transition metals and Al, Pb in poor metals group. For metalloids and non-metals all elements have high bond energy and they can all be obtained in amorphous structure when deposited by evaporation. In early transition metals, Ti, Zr, Hf, Nb, Ta, Cr, Mo, W, and V have high bond energy except Y. In this group Y is the only element which does not form amorphous structure.

According to the bond energy classification discussed in Table 6.1, it seems that it is not possible to obtain Mg in amorphous form. While the pure state does not provide an amorphous thin film, now we will search for an alloying option. The candidate alloying element should have a light weight and it has to provide the formation of amorphous form with possible minimum addition. Before going into details of alloying it is useful to carry out similar calculations on cooling rate for Mg-Cu. The phase diagram of this binary system is given in Fig. 6.1.

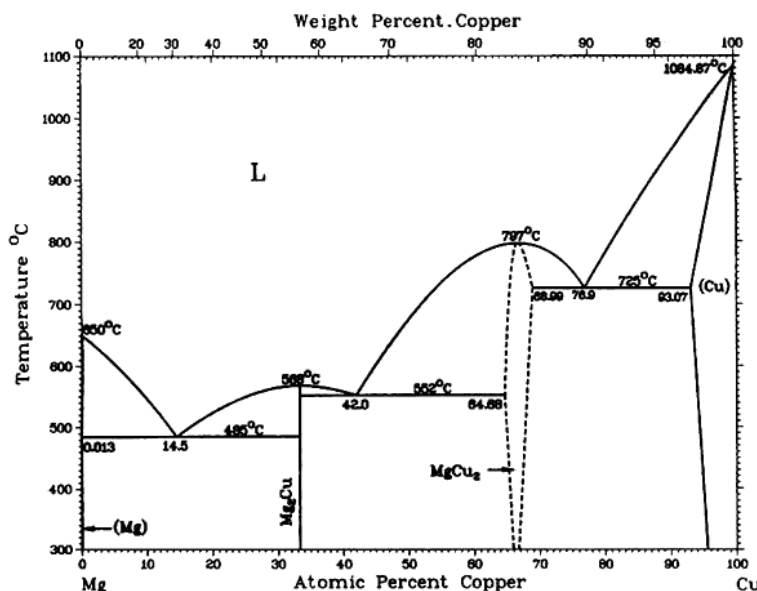


Figure 6.1 Mg-Cu binary phase diagram (Nayeb-Hashemi and Clark 1988).

This calculation for Mg:Cu=90:10 and Mg:Cu=85:15 assumes a homogenous mixture of vapor phase. No data is available on the critical cooling rate of Mg₉₀Cu₁₀, required for amorphous phase formation. The value given for Mg:Cu=85:15 by Reda *et al.* 1982 as $q_{cr} = 3.9 \times 10^5$ K/s at a reduced glass temperature of $T_{rg} \approx 0.45$.

The liquidus temperature of Mg:Cu=90:10 from Mg-Cu binary diagram is 818 K. Then the corresponding cooling rate when the substrate was cooled to 298 K is 1.62×10^6 K/s. Similarly, it is 1.86×10^6 K/s when the substrate was cooled to 223 K.

Similar calculations for Mg₈₅Cu₁₅ (liquidus temperature = 768 K) yields values of 1.44×10^6 K/s and 1.67×10^6 K/s for deposition on substrates held at 298 and 223 K, respectively. Our calculated cooling rate is about 4 times faster than the required cooling rate given by Reda and co-workers. Thus the amorphization which was observed in the alloy is consistent with the current estimation.

In order to preserve the amorphous structure, the substrate temperature has to be lower than T_g , glass transition temperature. Calculation of T_g using data given by Reda, yields a value of $T_g \approx 345$ K. Similar values were reported by Sommer *et al.* 1980 and Bailey *et al.* 2004, *e.g.* 380 and 350 K, respectively. The substrate temperature of 223 and 298 K used in the current experiment, 122 and 47 K, are below the T_g value. Under this condition both temperatures were expected to yield amorphous structure. The fact deposition of 298 K yielded crystalline structure both for Mg:Cu=90:10 and Mg:Cu=85:15 may be due to an increase in substrate temperature during deposition.

The amorphization conditions of Mg-Cu alloys present a very scattered data in literature. These data are summarized in Fig. 6.2. Figure clearly indicates that the production of an amorphous binary alloy depends on the processing parameters and may cover a wide range of compositions. Figure showed that, the theoretical amorphization range of Mg-Cu binary alloy is quite wide, *i.e.* at. %12-82 Cu. On the other hand, it indicates that the production temperature is substantially important in the selection of that range.

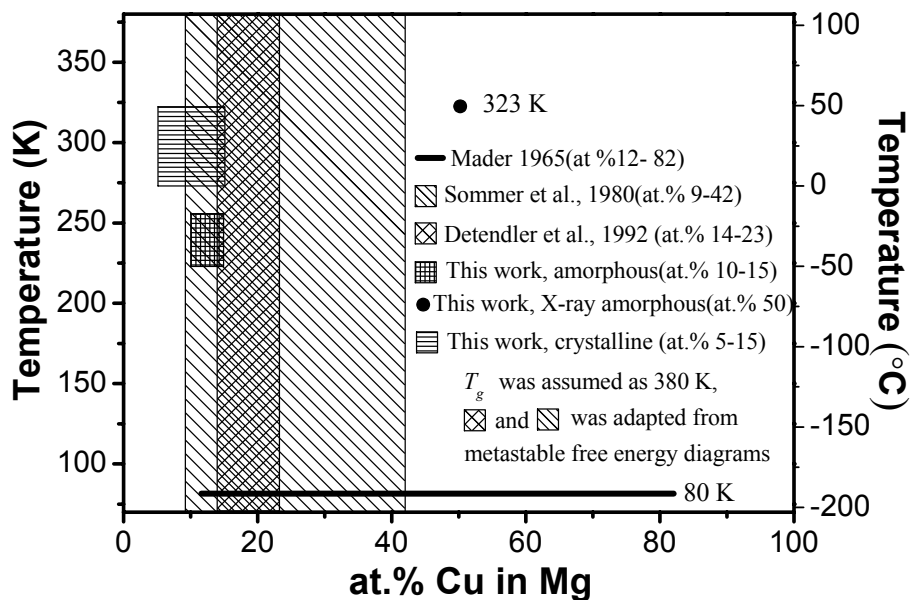


Figure 6.2 Amorphous composition range in Mg-Cu binary system as a function of temperature, without regarding the product is fully or X-ray amorphous.

In a recent study, Chou *et al.* 2009, showed that Mg-Cu binary alloys could be produced by co-sputtering in the range of 32 to 82 at.% Cu. However, according to transmission electron microscopy (TEM) investigations, the films are not actually amorphous, instead they are consisting of Cu₂Mg nanoparticles about 10-20 nm, embedded in an amorphous Mg-Cu matrix. Our thin films are X-ray amorphous in most cases. But this does not rule out a mixture structure for the films produced in this study, as similar to Chou's study, without a detailed TEM examination.

Following the evaluation of Mg-Cu system, the other alloying elements may be considered. Table 6.2 gives a list of binary systems collected from the literature. Table has two columns one for size difference and the other is “complexity”. It clearly shows that glass forming conditions in different systems show a great variety. This can be followed easily by examining the size difference values of the elements given in the table.

Table 6.2 Amorphous binary systems collected from the literature.

Alloy (A-B)	Comp. (at. % B)	$\left(\frac{r_A - r_B}{r_A} \right)$ %	Indication on the Phase Diagram and Composition (at. %)
<i>Cu-Al</i>	17.3	10.5	Eutectic, 17.3
<i>Ag-Si</i>	17-30	8.3	Eutectic , 89
<i>Fe-C</i>	16	-11.8	Eutectic, 16.2
<i>Mn-Si</i>	23-28	-1.5	Peritectic-(Intermetallics), 17.3
<i>Ti-Si</i>	15-20	18.4	Eutectic-Intermetallic, 14-25
<i>Re-Si</i>	35	26.5	Intermetallic-Eutectic, 33-38
<i>Au-Sn</i>	29-31	-12.5	Eutectic-Intermetallic, 28-50
<i>Pd-Si</i>	15-23	3.6	Eutectic-Intermetallic, 15-25
<i>Pt-Ge</i>	17-30	0.7	Eutectic-(Intermetallic)-Peritectic, 17.6-10.3
<i>Zr-Cu</i>	40-75	20	Peritectic-Eutectics-Intermetallics
<i>La-Ni</i>	86	33.5	Intermetallic-Eutectic, 16.6-7
<i>Y-Fe</i>	70-83	29.4	Eutectic-(Intermetallic)-Peritectic, 12.9-42.4
<i>Ca-Al</i>	25-50	31.25	Peritectic-(Intermetallic)-Eutectic, 9.5-65
<i>Be-Ti</i>	37-41	-66	Eutectic-Peritectic, 30-49
<i>Be-Zr</i>	30-50	82.3	Eutectic-Peritectic, 8.4-33
<i>Mg-Sb</i>	40	0.6	Intermetallic, 40
<i>Mg-Ca</i>	55-80	-23.1	Eutectic-Intermetallic, 10.5-33.3
<i>Mg-Cu</i>	35	20	Intermetallic-(Eutectic)- Intermetallic, 33.3-64.66
<i>Mg-Cu*</i>	10	20	Eutectic, 14.5
<i>Mg-Cu*</i>	15	20	Eutectic, Intermetallic, 14.5-33.3

(Table adapted from, Anglezio *et al.* 1994, ASM Handbook, Vol.3, 1992, Biggs *et al.* 2005, Cahn 1996, Chen *et al.* 1980, Cuevas and Hirscher 2003, Heiman and Kazama 1979, Okamoto 2006, Okamoto 2008, Predel 1992, Predel 1993, Predel 1995, Predel 1997, Predel 1998, and Takayama 1976, * this study)

Table 6.3 Comparison of candidate alloying elements as a substitution for Cu.

Alloy System	Atomic weight (B)	$\Delta r_{Mg,B}$ (%)	Complexity		
			Intermetallic Close to Mg	Composition at. % Mg	Structure of the Intermetal.
Mg-Cu	63.54	20	Mg ₂ Cu	66.67	oF48
Mg-Co	58.93	21.9	MgCo ₂	33.33	hP12
Mg-Ni	58.69	22.5	Mg ₂ Ni	66.67	hP18
Mg-Fe	55.84	21.2	No data	-	-
Mg-Mn	54.93	20.6	No data	-	-
Mg-V	50.94	16.2	Immiscible	-	-
Mg-Ti	47.86	8.1	Immiscible	-	-
Mg-Sc	44.95	-1.2	No data	-	-
Mg-Ca	40.07	-23.1	Mg ₂ Ca	66.67	hP12
Mg-K	39.09	-41.8	Immiscible	-	
Mg-Si	28.08	31.2	Mg ₂ Si	66.67	cF12
Mg-Al	26.98	10.6	Al ₁₂ Mg ₁₇	58.6	cI58
Mg-Na	22.98	16.2	Immiscible	-	-
Mg-B	10.81	46.8	MgB ₂	33.33	hP3
Mg-Be	9.01	30	MgBe ₁₃	7.14	cF112
Mg-Li	6.94	5	-	-	-

Depending on the discussions given above, a list of candidate alloying elements as a substitution for Cu is given in Table 6.3. All elements in this table have a lower atomic weight than Cu. This table compares the size difference, atomic weight and complexity as a criterion for candidate selection.

Shaded regions in the table show the candidate system that might possibly have a superior storage capacity. Starting from Cu, Ni with a weight of 58.69 g.mole⁻¹, is slightly lighter than Cu and has a similar size difference as well as phase diagram. Thus, Mg-Ni is expected to behave similar to the current Mg-Cu system.

V and Ti are roughly 22 % lighter than Cu and are interesting because of their catalytic effect in hydrogenation *i.e.* they could replace Pd capping as element embedded in the bulk of the film. Thus, Ti and V has been the subject of considerable interest in the literature (Baldi *et al.* 2009).

On the lighter side, elements of interest are Si, Al, Na, B, Be and Li. In terms of size difference elements Si, B and Be are similar, though B is extremely small with atomic radius of 82 pm. In terms of complexity of the phase diagram Mg-B system is interesting, comprising of 3 intermetallics, Fig. 6.3.

Mg-Si system has a eutectic very close to pure Mg which might be helpful in forming Mg-rich amorphous phase, Fig. 6.4. Mg-Al has also a eutectic with an intermetallic phase which has relatively complex crystal structure *i.e.* cI58, Fig. 6.5. It is possible to evaporate boron from a carbon or vitreous carbon crucible by e-beam deposition at excellent rates. RF sputtering may also be used. Si deposition can be achieved by both DC or RF sputtering, e-beam deposition and resistive evaporation by employing thick BeO, Ta or vitrous carbon crucibles.

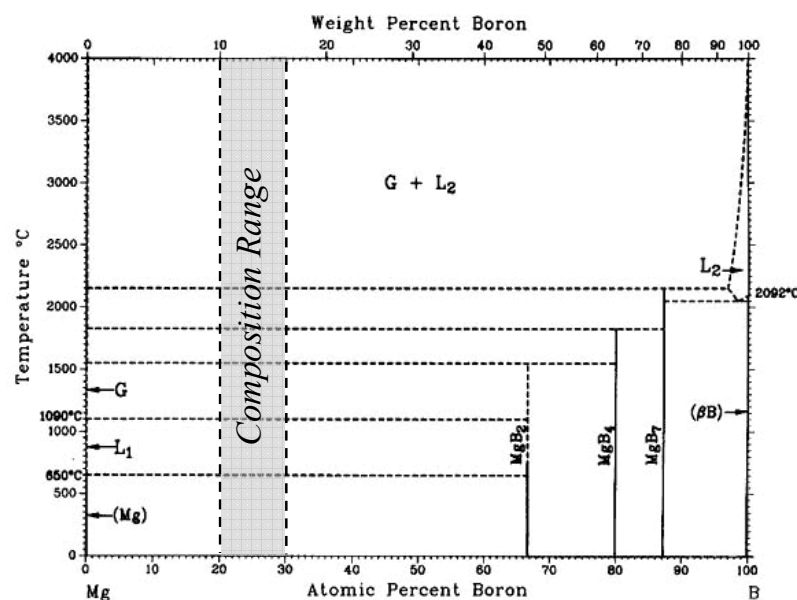


Figure 6.3 Mg-B binary phase diagram (Nayeb-Hashemi and Clark 1988).

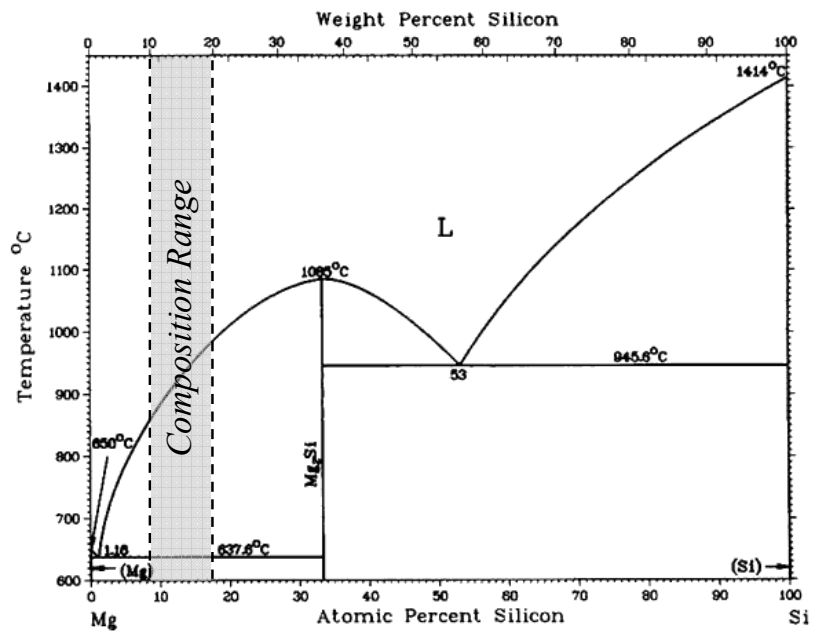


Figure 6.4 Mg-Si binary phase diagram (Nayeb-Hashemi and Clark 1988).

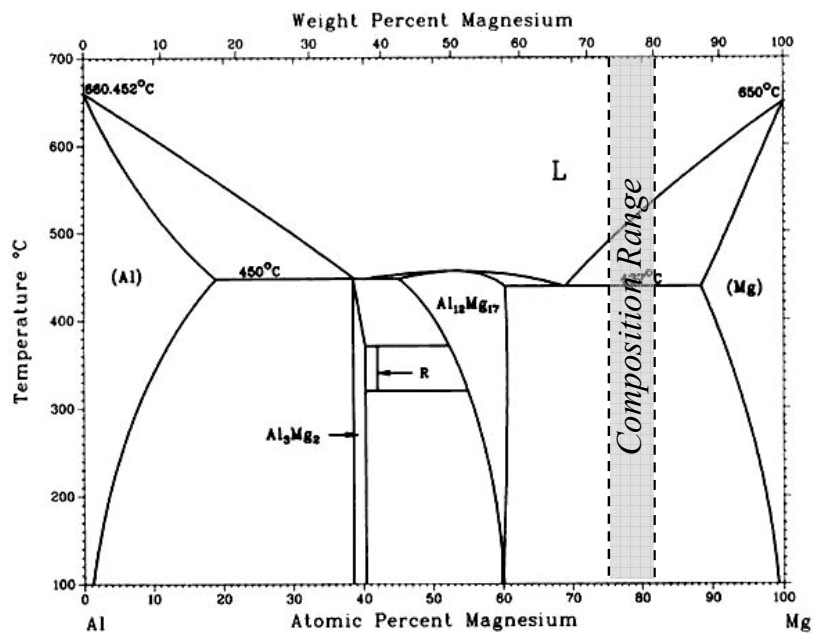


Figure 6.5 Mg-Al binary phase diagram (Nayeb-Hashemi and Clark 1988).

And finally, Al deposition can be performed successfully with all vapor deposition techniques.

The shaded regions on the phase diagrams, indicates possible compositions of interest. For a specific composition, (min. addition), when compared to pure Mg, hydrogen storage medium weight is increasing by just 3.4, 3.3, and 15.5 % for B, Si, and Al addition, respectively. This increase was 41.5 % in case of 10 at. % Cu alloying.

CHAPTER 7

CONCLUSIONS

A study was carried out for the production of Mg-based thin films which can absorb and desorb hydrogen near ambient conditions, with fast kinetics. For this purpose, Mg and Mg-based thin films were produced via physical vapor deposition method. Two units were constructed; one HV and the other UHV deposition system.

The HV system was based on a pyrex bell jar and had two independent evaporation sources. The unit was used to deposit thin films of Mg, Mg capped with Pd and Au-Pd as well as Mg-Cu both in co-deposited and multilayered form. The films were crystalline with columnar grains with some degree of preferred orientation.

Hydrogenation of these films has shown that;

- 1) Whether the films are single-or multilayered, if the as-deposited structure were to be used as hydrogen storage medium, there is always a narrow temperature window for hydrogenation. The upper limit of this window is determined by the formation of intermetallic phases.

The UHV deposition system had four independent evaporation sources and incorporated substrate cooling by circulating cooled nitrogen gas through the substrate holder. Deposition of Mg-Cu films using the UHV system yielded nanocrystalline and amorphous thin films. The hydrogen sorption of these films was followed by resistance measurements, with the samples heated isochronally, initially under hydrogen and then under vacuum.

The resistance data have shown that;

- 2) Hydrogen sorption behaviour of the thin films was improved by size refinement, and further by amorphization. Amorphous Mg:Cu=85:15, thin film could absorb hydrogen at room temperature and could desorb it at 50 °C with fast kinetics.

In terms useful storage medium;

- 3) Amorphous Mg:Cu=90:10 alloy can be recommended as the storage composition since it can store 5.9 wt. % of hydrogen with desorption temperature not exceeding 100 °C.

To maximize the storage capacity, elements that are lighter than Cu have been questioned as possible candidates for alloying addition instead of Cu. Of these elements, B, Si and Al appear to be potential alloying additions which are recommended for further studies.

Finally, it can be concluded that, thin film processing enables the tailoring of the composition, geometry, and structure of the material. This capability gives the opportunity to tune the microstructure and chemical make-up so as to develop materials with improved hydrogen sorption characteristics.

REFERENCES

- Aballe L., Barinov A., Locatelli A., Mentes T.O., Kiskinova M., Phys. Rev. B, 75, 11, (2007)
- Adamik M., Barna P.B., Tomov I., Key. Eng. Mat., 103, (1995)
- Aguey-Zinsou K.F., Ares-Fernandes J.R., Klassen T., Bormann R., Int. J. Hydrogen Energy, 32, (2007)
- Aguey-Zinsou K.F., Ares-Fernandes J.R., Energy Environ. Sci., 3, (2010)
- Ahmadzadeh M., Cantor B., J. Non-Cryst. Solids, 43, (1981)
- An K.S., Park R.J., Kim J.S., Park C.Y., Kim C.Y., Chung J.W., Kinoshita T., Kakizaki A., J. Electron Spectrosc. Relat. Phenom., 80, (1996)
- An K.S., Park R.J., Kim J.S., Park C.Y., Lee S.B., Abukawa T., Kono S., Kinoshita T., Kakizaki A., Ishii T., J. Appl. Phys., 78, 2, (1995)
- Andersson G., Aits K., Hjörvarsson B., J. Alloys Compd., 334, (2002)
- Andreasen A., Sørensen M.B., Burkarl R., Møller B., Molenbroek A.M., Pedersen A.S., Vegge T., Jensen T.R., Appl. Phys. A, 82, (2006)
- Andrievski R.A., Usp. Fiz. Nauk., 50, 7, (2007)
- Anglezio J.C., Servan C., Ansara I., Calphad, 18, 3, (1994)
- Alloy Phase Diagrams, Vol. 3, in ASM Handbook, Ed. Baker H., ASM International, Materials Park, Ohio, (1992)
- Arcot B., Murarka S.P., Clevenger L.A., Hong Q.Z., Ziegler W., Harper J.M.E., J. Appl. Phys., 76, (1994)
- Ares J.R., Cuevas F., Percheron-Guègan A., Acta Mater., 53, (2005)
- Arthur J.R., Brown T.R., J. Vac. Sci. Technol., 12, 1, (1975)
- Bailey N.P., Schiotz J., Jacobsen K.W., Phys. Rev. B., 69, 14, (2004)
- Baier P., Z. Phys., 213, 80, (1968)
- Baldi A., Gremaud R., Borsa D.M., Balde C.P., van der Eerden A.M.J., Kruijtzer G.L., Jongh P.E., Dam B., Griessen R., Int. J. Hydrogen Energy, 34, 3, (2009)
- Barna P.B., Adamik M., Thin Solid Films, 317, 1-2, (1998)
- Barna P.B., Autumn School on Advanced Materials Science and Electron Microscopy, Berlin, (2005)

- Bao S., Tajima K., Yamada Y., Jin P., Okada M., Yoshimura K., J. Ceram. Soc. Jpn., 116, 6, (2008)
- Bauer E., Poppa H., Todd G., Davis P.R., J. Appl. Phys., 48, 9, (1977)
- Bauer E., Van der Merwe J.H., Phys. Rev. B, 33, 6, (1986)
- Bauer E., Z. Kristallogr. 110, (1958)
- Baybörü E., Mechanical Milling of Magnesium Powders and Measurement of Their Hydrogen Sorption Characteristics, (Master Thesis), Middle East Technical University, Department of Metallurgical and Materials Engineering, (2001)
- Bazzanella N., Checchetto R., Miotello A., Appl. Phys. Lett., 85, 22, (2004)
- Behrndt K.H., J. Vac. Sci. Technol. 7, (1970)
- Berlouis L. E.A., Aguado R.P., Hall P.J., Morris S., Chandrasekaran L., Dodd S.B., J. Alloys Compd., 356–357, (2003)
- Berube V., Radtke G., Dresselhaus M., Chen G., Int. J. Energy Res., 31, (2007)
- Berry R.W., Hall P.M., Harris M.T., Thin Film Technology, Litton Educational Publishing, (1968), pp. 117, 124
- Biggs T., Taylor S.S., Van Der Lingen E., Platinum Metals Rev., 49, 1, (2005)
- Boakye F., AdanuK.G., Thin Solid Films, 279, 1-2, (1996)
- Bobet J.L., Chevalier B., Song M.Y., Darriet B., Etourneau J., J. Alloys Compd., 336, 1-2, (2002)
- Borsa D.M., Baldi A., Pasturel M., Schreuders H., Dam B., Griessen R., Vermeulen P., Notten P.H.L., Appl. Phys. Lett., 88, 24, (2006)
- Borsa D.M., Gremaud R., Baldi A., Schreuders H., Rector J.H., Kooi B., Vermeulen P., Notten P.H.L., Dam B., Griessen R., Phys. Rew. B., 75, (2007)
- Bouaricha S., Dodelet J.P., Guay D., Huot J., Boily S., Schulz R., L. Alloys Compd., 307, (2000)
- Bouaricha S., Huot J., Guay D., Schulz R., Int. J. Hydrogen Energy, 27, (2002)
- Bowman R.C., Attala A., Maeland A.J., Johnson W.L., Solid State Commun., 47, (1983)
- Buckel W., Z. Phys., 138, (1954)
- Buckel W., J. Vac. Sci. Technol., 6, 4, (1969)
- Buckel W., J. Vac. Sci. Technol., 10, 5, (1973)
- Bucur R.V., Flanagan T.B., Z. Phys. Chem., 88, (1974)

- Bunshah R.F., J. Vac. Sci. Technol., 11, 4, (1974)
- Bülow H., Buckel W., Z. Phys. 145, 141, (1956)
- Cahn R.W., Physical Metallurgy Part 2, Ed. Cahn R.W. and Haasen P., North Holland Physics Publishing, Netherlands, (1996), pp. 1725-6, 1736-39, 1744-45
- Chandramohan S., Sathyamoorthy R., Lalitha S., Senthilarasu S., Sol. Energy Mater. Sol. Cells, 90, (2006)
- Chen H.S., Rep. Prog. Phys. 43, (1980)
- Chen K., Yu Y., Mu H., Luo E.Z., Sundaravel B., Wong S.P., Wilson I.H., Surf. Coat. Tech., 151-152, (2002)
- ¹Chen J., Yang H.B., Xia Y.Y., Kuriyama N., Xu Q., Sakai T., Chem. Mater., 14, 7, (2002)
- Chopra K.L., Thin Film Phenomena, McGraw-Hill, New York, 1969, p.195
- Chou H.S., Huang J.C., Lai Y.H., Chang L.W., Du X.H., Chu J.P., Nieh T.G., J. Alloys Compd., 483, 1-2, (2009)
- Christmann K., Surf. Sci. Rep., 9, (1988)
- Cohen M.H., Turnbull D., Nature, 203, (1964)
- Cohen M.H., Grest G.S., Phys. Rev. B., 20, 3, (1979)
- Comberg A., Ewert S., Bergmann G., Z. Phys., 271, 3, (1974)
- Cuevas F., Hirscher M., Acta Mater., 51, 3, (2003)
- Dam B., Gremaud R., Broedersz C., Griessen R., Scr. Mater., 56, 10, (2007)
- Darnaudery J.P., Darriet B., Pezat M., Int. J. Hydrogen Energy, 8, (1983)
- Davies H.A., Phys. Chem. Glasses, 17, (1976)
- Deiss J.L., Elidrissi B., Robino M., Tapero M., Zielinger J.P., Weil R., Phys. Scr., 37, 4, (1988)
- Detendler R.H., Kovacs J.A., Alonso J.A., J Mater. Sci., 27, 18, (1992)
- Doppiu S., Solsona P., Spassov T., Barkhordarian G., Dornheim M., Klassen T., Suriñach S., Baró M.D., J. Alloys Compd., 404–406, (2005)
- Dubey K.S., Ramachandrarao P., Int. J. Rapid Solidif., 5, (1990)
- Egami T., Mater. Trans., 43, 3, (2002)
- Eliaz N., Eliezer D., Adv. Perf. Mat., 6, (1999)
- Eliaz N., Fuks D., Eliezer D., Acta Mater., 47, 10, (1999)

- Farangis B., Nachimuthu P., Richardson T.J., Slack J.L., Meyer B.K., Perera R.C.C., Rubin M.D., Solid State Ionics, 165, (2003)
- Feenstra R., DeGroot D.G., Rector J.H., Salomons E., Griessen R., J. Phys. F: Met. Phys., 16, (1986)
- Frederick M.J., Goswami R., Ramanath G., J. Appl. Phys., 93, 10, (2003)
- Frieske H., Wicke E., Bunsengesel. Phys. Chem., 77, 48, (1973)
- Fujii H., Orimo S., Physica B, 328, 1-2, (2003)
- Galkin K.N., Dotsenko S.A., Galkin N.G., Kumar M., Govind R., Shivaprasad S.M., Semiconductors, 42, 4, (2008)
- Ge L., Hiu X.D., Chen G.L., Liu Z.K., Acta Phys-Chim. Sin., 23, 6, (2007)
- Giebels I.A.M.E., Isidorsson J., Griessen R., Pyys. Rev. B., 69, (2004)
- Glang R., Handbook of Thin Film Technology, Ed. Maissel L. I. and Glang R., McGraw-Hill, New York, (1970), Chap.1
- Gremaud R., Broedersz C.P., Borsa D.M., Borgschulte A., Mauron P., Schreuders H., Rector J.H., Dam B., Griessen R., Adv. Mater., 19, 19, (2007)
- Gremaud R., Borgschulte A., Chacon C., Van Mechelen J.L.M., Schreuders H., Züttel A., Hjörvarsson B., Dam B., Griessen R., Appl. Phys. A, 84, (2006)
- Grima R., DeGraffenreid J., Venables J.A., Phys. Rew. B., 76, 23, (2007)
- Grovenor C.R.M., Hentzell H.T.G., Smith D.A., Acta Metall., 32, 5, (1984)
- Grochala W., Edwards P.P., J. Alloys Compd., 404-406, (2005)
- Gross K.J., Chartouni D., Leroy E., Züttel A., Schlapbach L., J. Alloys Compd., 269, (1998)
- Gutfleisch O., DeBoer N. S., Pratt A.S., Walton A., Speight J., Harris I.R., Züttel A., J. Alloys Compd., 356–357, (2003)
- Guthrie S.E., Thomas G.J., Hydrogen in Semiconductors and Metals, in Materials Research Society Symp. Proc., Eds. Nickel N.H., Jackson W.B., Bowman R.C. and Leisure R.G., 513, (1998), pp. 93-98
- Güvendiren M., Baybörü E., Öztürk T., Int. J. Hydrogen Energy, 26, 5, (2004)
- Hafner J., Phys. Rev. B, 28, 4, (1983)
- Hashimoto T., Okamoto K., Hara K., Kamiya M., Fujiwara H., Thin Solid Films, 91, 2, (1982)
- He Y., Liu Y., Zhao Y., Nanotechnology 19, (2008)

- Heiman N., Kazama N., Phys. Rev. B., 19, 3, (1979)
- Hentzell H.T.G., Anderson B., Karlsson S.E., Acta Metall., 31, 12, (1983)
- Hentzell H.T.G., Grovenor C.R.M., Smith D.A., J. Vac. Sci. Technol. A, 2, 2, (1984)
- Higuchi K., Kajioka H., Toiyama K., Fujii H., Orimo S., Kikuchi Y., J. Alloys Compd., 293, (1999)
- Higuchi K., Yamamoto K., Kajioka H., Toiyama K., Honda M., Orimo S., Fujii H., J. Alloys Compd., 330, (2002)
- Hirth J.P., Moazed K.L., Thin Films Physics, Ed. Hass G. and Thun R.E., Vol. 4, Academic Press, New York, (1967), p. 97
- Hjort P., Krozer A., Kasemo B., J. Alloys Compds, 234: L11-L15, (1996)
- Hjort P., Krozer A., Kasemo B., J. Alloys Compd., 237, 1-2, (1996)
- Hjörvarsson B., Ryden J., Karlsson E., Birch J., Sundgren J.E., Phys. Rev. B, 43, 8, (1991)
- Hoffman K.C., Reilly J.J., Salzano F.J., Waide C.W., Wiswall R.H., Winsche W.E., Int. J. Hydrogen Energy, 1, 2, (1976)
- Hong Q.Z., Dheurle F.M., J. Appl. Phys., 72, (1992)
- Hu W.K., Zhang Y.S., Song D.Y., Shen P.W., Int. J. Hydrogen Energy, 21, 8, (1996)
- Huang Z.G., Guo Z.P., Wexler D., Konstantinov K., Liu H.K., J. Alloys Compd., 426, (2006)
- Huiberts J.N., Rector J.H., Wijngaarden R.J., Jetten S., de Groot D., Dam B., Koeman N.J., Griessen R., Hjörvarsson B., Olafsson S., Cho Y.S., J. Alloy. Compd., 239, (1996)
- Hunderi O., Myers H.P., J. Phys. F: Met. Phys., 4, (1974)
- Ievlev V.M., Inorg. Mater., 40, 2, (2004)
- Ingason A.S., Olafsson S., J. Alloys Compd., 404-406, (2005)
- Inoue A., Yamamoto H., Masumoto T., Mater. Trans., JIM, 31, 12, (1990)
- Inoue A., Mat. Trans. JIM, 36, 7, (1995)
- Ivanov E., Konstanchuk I.G., Stepanov A., Boldyrev V.V., J. Less-Common Met., 131, (1987)
- Iwakura C., Nohara S., Zhang S.G., Inoue H., J. Alloys Compd., 285, (1999)

- Jain I.P., Vijay Y.K., Malhotra L.K., Uppadhyay K.S., Int. J. Hydrogen Energy, 13, 1, (1988)
- John M.E., Andrè V., Guido L., Phys. Rev. B, 23, (1996)
- Jurczyk M., Smardz L., Okonska I., Jankowska E., Nowak M., Smardz K., Int. J.Hydrogen Energy, 33, (2008)
- Kaiser N., Appl. Opt., 41, 16, (2002)
- Kelly S.T., Van-Atta S.L., Vajo J.J., Olson G.L., Clemens B.M., Nanotechnology, 20, (2009)
- Kalisvaart W.P., Niessen R.A.H., Notten P.H.L., J.Alloys Compd., 417, (2006)
- Kaneko K., Kajitani T., Hirabayashi M., Ueno M., Suzuki K., J. Less-Common Met., 89, 1, (1983)
- Kang B., Zhao Z., Poulikakos D., J. Heat Transf., 116, (1994)
- Kauzman W., Chem. Phys., 43, (1948)
- Khelfa A., Benramdanet N., Guesdon J.P., Julienf C., Semicond. Sci. Technol., 9, (1994)
- Kijek M., Ahmadzadeh M., Cantor B., Cahn R.W., Scr. Metall., 14, (1980)
- Kirchheim R., Sommer F., Schluckeiber G., Acta Metall., 30, 6, (1982)
- Klassen T., in Nanostructure Control of Materials, Eds. Hannink R.H.J. and Hill A.J., Woodhead, Cambridge, 2006, pp. 266–302
- Klassen T., Oelerich W., Bormann R., Mater. Sci. Forum, 360-362, (2001)
- Krozer A., Kasemo B., J. Less-Common Met., 160, (1990)
- Krozer A., Kasemo B., J. Phys:Condens. Matter., 1, (1989)
- Krozer A., Kasemo B., J. Vac. Sci. Technol. A, 5, 4, (1987)
- Kumar S., Reddy G.L.N., Raju V.S., J. Alloys Compd., 476, (2009)
- Lee Y.W., Rigsbee J. M., Surf. Sci., 173, 1, (1986)
- Lee D., Lee G., Kim S., Hwang C., Koo J.Y., Lee H., J. Phys.:Condens. Matter., 19, (2007)
- Lee Y.W., Clemens B.M., Gross K.J., J. Alloys Compd., 452, (2008)
- Léon A., Knystautas E.J., Huot J., Schulz R., J. Alloys Compd., 345, (2002)
- Léon A., Knystautas E.J., Huot J., LoRusso S., Koch C.H., Schulz R., J. Alloys Compd., 356, (2003)
- Li Y., J. Miner. Met. Mater. Soc., JOM, 57, 3, (2005)

- Liang G., J. Alloys Compd., 370, (2004)
- Liang G., Huot J., Boily S., Van Neste A., Schulz R., J. Alloys Compd., 292, (1999)
- Lim S.C., Kim K.K., Jeong S.H., An K.H., Lee S.B., Lee Y.H., Int. J. Hydrogen Energy, 32, 15, (2007)
- Liou S.H., Chien C.L., Phys. Rev. B., 35, (1987)
- Liu C.T., Lu Z.P., Intermetallics, 13, 3-4, (2005)
- Lu Z.P. , Liu C.T. , Dong Y.D., J. Non-Cryst. Solids, 341, 1-3, (2004)
- Liu W.H., Wu H.Q., Lei Y.Q., Wang Q.D., Wu J., J. Alloys Compd., 252, 1-2, (1997)
- Lukens W.E., Wagner C.N.J., J. Phys. Sci. A28, 2, (1973)
- Mader S., J. Vac. Sci. Technol., 2, 35, (1965)
- Mader S., J. Vac. Sci. Technol. 8, 1, (1971)
- Mader S., Nowick A.S., Widmer H., Acta Metall., 15, (1967)
- Mader S., Nowick A.S., Acta Metall., 15, 2, (1967)
- Maeland A.J., Tanner L.E., Libowitz G.G., J. Less-Common Met., 74, 2, (1980)
- Milanese C., Girella A., Bruni G., Berbenni V., Cofrancesco P., Marini A., Villa M., Matteazzi P., J. Alloys Compd., 465, (2008)
- Messier R., Giri P.A., Roy R., J. Vac. Sci. Technol. A, 2, 2, (1984)
- Mekhrabov A.O., Akdeniz M.V., Acta Mater., 47, 7, (1999)
- Mintz M.H., Gavra Z., Kimmel G., Hadari Z., J. Less-Common Met., 74, 2, (1980)
- Miyamura H., Kuriyama N., Sakai T., Oguro K., Uehara I., Ishikawa H., J. Alloys Compd., 192, 1-2, (1993)
- Morris S., Dodd S.B., Hall P.J., Mackinnon A.J., Berlouis L.E.A., J. Alloys Compd., 293-295, (1999)
- Mosaner P., Bazzanella N., Bonelli M., Checchetto R., Miotello A., Mat. Sci. Eng. B, 108, 1-2, (2004)
- Movchan B.A., Demchishin A.V., Phys. Metals Metallog., 28, 4, (1969)
- Mulheran P.A., Europhys. Lett., 65, 3, (2004)
- Nakamura K., Scr. Metall., 18, (1984)
- Nayeb-Hashemi A.A., Clark J.B., in The Phase Diagrams of Binary Magnesium Alloys, 1st ed., ASM International, Metals Park, Ohio, 44072, (1988)

- Neugebauer C.A., in *Handbook of Thin Film Technology*, Ed. Maissel L.I. and Glang R., Chap. 8, McGraw-Hill, New York, (1970)
- Nilsson H.T.G., Andersson B., Karlsson S.E., *Thin Solid Films*, 63, 1, (1979)
- Nowick A.S., Mader S., in *Basic Problems in Thin Film Physics*, Ed. Niedermayer R. Mayer H., Vandmhoeek & Ruprecht, Göttingen, (1966), p. 212.
- Nowick A.S., Mader S.R., *IBM J. Res. Develop.*, 9, (1965)
- Oelerich W., Klassen T., Bormann R., *J. Alloys Compd.*, 315, (2001)
- Oguchi H., Heilweil E.J., Josell D., Bendersky L.A., *J. Alloys Compd.*, 477, 1-2, (2009)
- Ohring M., in *Materials Science of Thin Films, Deposition and Structure*, 2nd ed., Academic Press, San Diego, (2002), pp. 9, 358, 374, 502, 542, 546
- Okamoto K., Hara K., Kamiya M., Hashimoto T., Fujiwara H., *Thin Solid Films*, 176, 2, (1989)
- Okamoto H., *J Phase Equilib. Diff.*, 27, 4, (2006)
- Okamoto H., *J. Phase Equilib. Diff.*, 29, 2, (2008)
- Olsson S., *Phase Transitions and Phase Formation of Hydrogen in Quasi-2D Lattices*, (PhD Thesis), Uppsala University, Faculty of Science and Technology, Department of Physics, (2003)
- Orimo S., Ikeda K., Fujii H., Fujikawa Y., Kitano Y., Yamamoto K., *Acta Mater.*, 45, 6, (1997)
- Orimo S.I., Nakamori Y., Eliseo J.R., Züttel A., Jensen C.M., *Chem. Rev.*, 107, (2007)
- Ostenfeld C.W., Johansson M., Chorkendorff I., *Surf. Sci.*, 601, (2007)
- Ovshinsky S.R., Fetchenko M.A., Ovonic Battery, US Patent, 5506069, (1996)
- Ouyang L.Z., Wang H., Zhu M., Zou J., Chung C.Y., *J. Alloys Compd.*, 404–406, (2005)
- Özgit Ç., Isochronal Hydrogenation of Textured Magnesium/Palladium Thin Films, (Master Thesis), Middle East Technical University, Department of Metallurgical and Materials Engineering, (2009)
- Paillier J., Roué L., *J. Electrochem. Soc.*, 152, 1, E1-E8, (2005)
- Pasturel M., Slaman M., Schreuders H., Rector J.H., Borsa D.M., Dam B., Griessen R., *J. Appl. Phys.* 100, (2006)

- Pauleau Y., in Handbook of Thin Film Materials, Nalwa H.S., Academic Press, San Diego, CA, (2002)
- Pehlivanoglu M.K., Production and development of bulk metallic glasses, PhD Thesis, Department of Metallurgical and Materials Engineering, METU, (2003)
- Pezzagna S., Vezian S., Brault J., Massies J., *Appl. Phys. Lett.*, 92, 23, (2008)
- Polk D.E., *Acta Metall.*, 20, (1972)
- Pranevicius L., Milcius D., Pranevicius L.L., Thomas G., *J. Alloys Compd.*, 373, 1-2, (2004)
- Pranevicius L., Wirth E., Milcius D., Lelis M., Pranevicius L.L., Bacianskas A., *Appl. Surf. Sci.*, 255, (2009)
- Predel B., in Landolt-Bornstein - Group IV Physical Chemistry, Ed. by Madelung O., Springer-Verlag, Vol. 5b, (1992), p. 1
- Predel B., in Landolt-Bornstein - Group IV Physical Chemistry, Ed. by Madelung O., Springer-Verlag, Vol. 5c, (1993), p. 1
- Predel B., in Landolt-Bornstein - Group IV Physical Chemistry, Ed. by Madelung O., Springer-Verlag, Vol. 5e, (1995), p. 1
- Predel B., in Landolt-Bornstein - Group IV Physical Chemistry, Ed. by Madelung O., Springer-Verlag, Vol. 5h, (1997), p. 1
- Predel B., in Landolt-Bornstein - Group IV Physical Chemistry, Ed. by Madelung O., Springer-Verlag, Vol. 5I, (1998), p. 1
- Pundt A., *Adv. Eng. Mat.*, 6, 1-2, (2004)
- Pundt A., Kirchheim R., *Annu. Rev. Mater. Res.*, 36, (2006)
- ¹Qu J.L. , Wang Y.T., Xie L., Zheng J., Liu Y., Li X.G., *J. Power Sources*, 186, 2, (2009)
- ²Qu J.L., Wang Y.T., Xie L., Zheng J., Liu Y., Li X.G., *Int. J. Hydrogen Energy*, 34, 4, (2009)
- Quinn J., Jona F., *Surf. Sci.*, 249, 1-3, (1991)
- Ramachandra R.P., *Z. Metallk.*, 71, (1980)
- Recham N., Bhat V.V., Kandavel M., Aymard L., Taracson J.M., Rougier A., *J. Alloys Compd.*, 464, (2008)
- Reda I.M., Hafner J., Pongratz P., Wagendristel A., Bangert H., Bhat P.K., *Phys. Status Solidi A: Applied Research*, 72, 1, (1982)

- Rehm C., Fritzsche H., Maletta H., Klose F., Phys. Rev. B, 59, (1999)
- Rehm C., Klose F., Nagengast G., Malette H., Weidinger A., Physica B., 234, (1997)
- Reilly J.J., Wiswall R.H., Inorg. Chem., 6, 12, (1967)
- Reilly J.J., Wiswall R.H., 7, 11, (1968)
- Richardson T.J., Slack J.L., Armitage R.D., Kostecki R., Farangis B., Rubin M., Appl. Phys. Lett., 78, 20, (2001)
- Richardson T.J., Farangis B., Slack J.L., Nachimuthu P., Perera R., Tamura N., Rubin M., J. Alloys Compd., 356, (2003)
- Richter H., Berckhemer H., Breitling G., Z. Naturforsch., A: Phys. Sci., 9, 2, (1954)
- Roger D.F., Madana G.S., Gemma G., Francesc P., Javier R.V., J. Power Sources, 169, 1, (2007)
- Rush J.J., Rowe J.M., Maeland A.J., J. Phys. F: Met. Phys., 10, 10, (1980)
- Rydén J., Hjörvarsson B., Ericsson T., Karlsson E., Krozer A., Kasemo B., J. Less Common Met., 152, (1989)
- Sadoc J.F., Dixmier J., Guinier A., Acta Crystallogr A., 28, (1972)
- Sakintuna B., Lamari-Darkrim F., Hirscher M., Int. J. Hydrogen Energy, 32, (2007)
- Sakamoto Y., Takao K., Baba K., Mat. Sci. Eng., 97, (1988)
- Samwer K., Johnson W.L., Phys. Rev. B., 28, 6, (1983)
- Sandrock G., Thomas G.M., Appl. Phys. A., 72, 153, (2001)
- Schiller F., Heber M., Servedio V.D.P., Laubschat C., Pyhs. Rev. B, 70, 12, (2004)
- Schwarz R.B., Johnson W.L., Phys. Rev. Lett., 51, 5, (1983)
- Selvam P., Viswanathan B., Swamy C.S., Srinivasan V., Int. J. Hydrogen Energy, 11, 3, (1986)
- Serikawa T., Henmi M., Kondoh K., J. Vac. Sci. Technol. A, 22, 5, (2004)
- Shao H., Asano K., Enoki H., Akiba E., J. Alloys Compd., 477, (2009)
- Shi F., Shim Y., Amar J.G., Phys. Rev. E., 74, 2, (2006)
- Singh S., Eijt S.W.H., Zandbergen M.W., Legerstee W.J., Svetchnikov V.L., J. Alloys Compd., 441, (2007)
- Sigma Instruments, <http://www.inficonthinfilmdeposition.com/en/index.html>, (22/08/2010)

- Slack J.L., Locke C.W.J., Song S.W., Ona J., Richardson T.J., Sol. Energy Mater. Sol. Cells, 90, 485, (2006)
- Slowik C.H., Phys. Rev. B., 10, 2, (1974)
- Smith D.L., in Thin Film Deposition: Principles and Practice, Mc-Graw-Hill, New York, (1995)
- Sommer F., Bucher G., Predel B., J. Phys. Colloque, C-8, 41, (1980)
- Spassov T., Köster U., J. Alloys Compd., 287, (1999)
- Spit F.H.M., Drijver J.W., Radelaar S., Z. Phys. Chem., 116, (1979)
- Spit F.H.M., Drijver J.W., Radelaar S., Scr. Metall., 14, 10, (1980)
- Srolovitz D.J., Mazor A., Bukiet B.G., J. Vac. Sci. Technol., 6, 4, (1988)
- Stoltz S.E., Popovic D., Surf. Sci., 601, (2007)
- Stoltz U., Weller M., Kirchheim R., Scr. Metall., 20, (1986)
- Suryanarayana C., Prog. Mater. Sci., 46, 1-2, (2001)
- Süer S., Mekhrabov A.O., Akdeniz M.V., J. Non-Cryst. Solids, 355, (2009)
- Takayama S., J. Mat. Sci., 11, 1, (1976)
- Takeichi N., Tanaka K., Tanaka H., Tamotsu T., Kamiya U.Y., Tsukahara M., Miyamura H., Kikuchi S., J. Alloys Compd., 446-447, (2007)
- Tan H., Ma D., Feng Y.P., Li Y., Acta Mater., 51, (2003)
- Tan J.J., Qu X.P., Xie Q., Zhou Y., Ru G.P., Thin Solid Films, 504, (2006)
- Tang F., Yuan W., Lu T.M., Wang G.C., J. Appl. Phys., 104, (2008)
- Tang F., Parker T., Li H.F., Wang G.C., Lu T.M., Nanotechnology, 19, 46, (2008)
- Tegenkamp C., Michailov M., Wollschläger J., Pfnür H., Appl. Surf. Sci., 151, 1-2, (1999)
- Thornton J.A., J. Vac. Sci. Technol., 11, 4, (1974)
- Thornton J.A., J. Vac. Sci. Technol., 12, 4, (1975)
- Thornton J.A., Ann. Rev. Mater. Sci., 7, (1977)
- Tkatch V.I., Limanovskii A.I., Denisenko S.N., Rassolov S.G., Mat. Sci. Eng. A, 323, (2002)
- Turnbull D., Contemp. Phys., 10, 5, (1969)
- Turnbull D., Metall. Trans. A., 12, 2, (1981)

- U.S. Department of Energy, DOE, URL; http://www1.eere.energy.gov/hydrogenandfuelcells/pdfs/mhcoe_materials_downselect_report_fy07.pdf, p.17, (15.04.2010)
- U.S. Department of Energy, DOE, Basic Research Needs for Hydrogen Economy, (2003)
- U.S. Department of Energy, DOE, URL; http://www1.eere.energy.gov/hydrogen-andfuelcells/storage/pdfs/targets_onboard_hydro_storage.pdf, (15.04.2010)
- Uhlmann D.R., J. Non-Cryst. Solids, 7, 4, (1971)
- Vajo J.J., Mertens F., Ahn C.C., Bowmann R.C., Fultz B., J. Phys. Chem. B., 108, (2004)
- Vajo J.J., Skeith S.L., Mertens F., J. Phys. Chem. B., 109, (2005)
- Van-der Kolk G.J., J Mater. Sci., 3, 2, (1988)
- Venables J.A., Spiller G.D.T, Hanbücken M., Rep. Prog. Phys., 47, 4, (1984)
- Vermeulen P., Niessen R.A.H., Notten P.H.L., Electrochim. Commun., 8, (2006)
- Vijh A.K., J. Mat. Sci., 10, 6, (1975)
- ¹Vook R.W, Witt F., J. Vac. Sci. Technol., 2, 49, (1965)
- ²Vook R.W, Witt F., J. Vac. Sci. Technol., 2, 243, (1965)
- Wagner R.S., Voorhoeve R.J.H., J. Appl. Phys., 42, 10, (1971)
- Wang H., Ouyang L.Z., Peng C.H., Zeng M.Q., Chung C.Y., Zhu M., J. Alloys Compd., 370, 1-2, (2004)
- Wang L.M., Li Z., Chen Z., Zhao Y., Liu R., Tian Y., J. Phys. Chem. B., 114, (2010)
- Wang X.L., Tu J.P., Wang C.H., Zhang X.B., Chen C.P., Zhao X.B., J. Power Sources, 159, 163–166, (2006)
- Wenzl H., Klatt K.H., Meuffels P., Papathanassopoulos K., J. Less-Common Met., 89, (1983)
- Westerwaal R.J., Slaman M., Broedersz C.P., Borsa D.M., Dam B., Griessen R., Borgschulte A., Lohstroh W., Kooi B., Ten Brink G., Tschersich K.G., Fleischhauer H.P., J. Appl. Phys., 100, (2006)
- Wu W.F., Li Y., Appl. Phys. Lett., 95, (2009)
- ¹Xia L., Fang S.S., Wang Q., Dong Y.D., Liu C.T., J. Appl. Phys. Lett., 88, (2006)
- ²Xia L., Li W.H., Fang S.S., Wei B.C., Dong Y.D., J. Appl. Phys., 99, (2006)

- Xilian S., Jianda S., Appl. Surf. Sci., 253, (2006)
- Xu X., Song C., Appl. Catal. A., 300, (2006)
- Yamamoto K., Higuchi K., Kajioka H., Sumida H., Orimo S., Fujii H., J. Alloys Compd., 330-332, (2002)
- Yang B., Du Y., Liu Y., Trans. Nonferrous Met. Soc. China, 19, (2009)
- Yasuda K., Hirano Y., Kamino T., Hirokawa K., Anal. Sci., 10, (1994)
- Yoshimura K., Yamada Y., Okada M., Surf. Sci., 566/568, 751, (2004)
- Yoshimura K., Bao S.H., Yamada Y., Okada M., Vacuum, 80, 7, (2006)
- Yuan G., Amiya K., Inoue A., J. Non-Cryst. Solids, 351, 8-9, (2005)
- Zabel H., Weidinger A., Comments Cond. Mat. Phys., 17, (1995)
- Zaluski L., Zaluska A., Ström-Olsen J.O., J. Alloys Compd., 288, (1999)
- Zhou L., Renewable and Sustainable Energy Reviews, 9, (2005)
- Züttel A., Naturwissenschaften, 91, (2004)
- Züttel A., JRC Workshop on Hydrogen Storage Technologies, Presentations Handout Book, Petten, Netherlands, (2005), pp. 61-62

CURRICULUM VITAE

PERSONAL INFORMATION

Surname, Name: Akyıldız, Hasan
Nationality: Turkish (TC)
Date and Place of Birth: 03 March 1977, Akşehir
Marital Status: Single
Phone: +90 312 210 5919
Fax: +90 312 210 2518
e-mail: akhasan@metu.edu.tr

EDUCATION

Degree	Institution	Year of Graduation
BS	Anadolu University, Ceramic Engineering	2000
High School	Kocaeli Anatolian High School	1995

WORK EXPERIENCE

Year	Place	Enrollment
2010 -present	METU, Department of Metallurgical and Materials Engineering	Research Assistant
2009-2010 (12 months)	NCSU, Department of Materials Science and Engineering	Visiting Scholar
2002-2009	METU, Department of Metallurgical and Materials Engineering	Research Assistant
2000-2001	Çelebi Vitrifiye	Process Engineer
1999 (July)	Torprak Vitrifiye	Intern Engineering Student
1998 (July)	Toprak Karo	Intern Engineering Student

FOREIGN LANGUAGE

Advanced English

PUBLICATIONS

- 1- H. Akyıldız, M. Özenbaş, T. Öztürk, Hydrogen absorption in magnesium based crystalline thin films, *Int. J. Hydrogen Energy*, 31(10), 1379-1383, 2006
- 2- H. Akyıldız, G. Çakmak, S. Tan, T. Öztürk, A screening method for hydrogen storage alloys, *Turk. J. Eng. Env. Sci.*, 31, 289-295, 2007
- 3- H. Akyıldız, T. Öztürk, Hydrogen sorption in crystalline and amorphous Mg-Cu thin films, *J. Alloys Compd.*, 492(1-2), 745-750, 2010
- 4- Ç. Özgit, H. Akyıldız, T. Öztürk, Isochronal hydrogenation of textured Mg/Pd thin films, *Thin Solid Films*, 518(17), 4762-4767, 2010